



DIPLOMARBEIT

„Synthesis, Ultrafast Spectroscopy and Theoretical Modeling of Lutetium Bisphthalocyanine“

Verfasser

Oliver Bixner

angestrebter akademischer Grad

Magister der Naturwissenschaften (Mag. rer. nat.)

Wien, August 2011

Studienkennzahl lt. Studienblatt: A 419

Studienrichtung lt. Studienblatt: Chemie

Betreuerin / Betreuer: Prof. Dr. Werner Jakubetz

Acknowledgement

In the beginning I would like to appreciate my family, especially my parents and my brother for their steady familiar and financial support as well as for their continuous encouragement during my studies.

My advisor Prof. Dr. Werner Jakubetz is honored for his friendly and helpful aid, the possibility to investigate various problems with different methods just as for supply of his technical skills at any time of the work.

Special acknowledgement is dedicated to the Ultrafast Dynamics group of Prof. Dr. Harald F. Kauffmann at the Faculty of Physics, Department Electronic Properties of Materials for the all-time supervision. My gratitude is directed to Prof. Kauffmann for providing the opportunity of implementation, the situated topic, continuous promotion of interest into this work and his financial support. A note of special thanks is addressed to Dr. Niklas Christensson for his ongoing care, collegial support and extensive advices in all concerns throughout the whole preparation period of this thesis. I also like to award Dr. Franz Milota and Dr. Jürgen Hauer for valuable mediation of backgrounds, technical consulting and the excellent working climate. This is certainly not self-evident !

A large portion of recognition and approval is directed to the Bioorganic Chemistry working group, Department of Organic Chemistry at the University of Vienna especially to Mag. Michael Fischer, Mag. Christoph Schmölzer und Prof. Dr. Walther Schmid who enabled the synthesis and characterization parts. I would like to thank them for providing guidance, labware and competent care during work.

I am also greatly thankful to Prof. Dr. Eberhard Riedle, Dr. Igor Pugliesi und Mag. Max Bradler of the Biomolecular Optics Group, Institute of Physics at Ludwig-Maximilians-University Munich for additional investigations at their labs and their help in the realm of broadband pump-probe spectroscopy.

Furtheron I owe appreciation to Dr. Vladimir Lukes, Department of Quantum Chemistry, Technical University of Bratislava for putting up the computing power of the DFT simulations, a fruitful cooperation and collegial instructions.

Finally I want to thank my good friends Hannes Faßhuber, Thomas Werzer, Daniel Greuter and Thomas Wehsner for their continuous help and encouraging words.

Zusammenfassung

In dieser Arbeit wurde der Doppeldecker Komplex Lutetium Bisphthalocyanin synthetisiert um elektronische Wechselwirkungen der beiden makrozyklischen Liganden auf ultraschnellen Zeitskalen im Hinblick auf Energietransfer und Ladungstrennung zu studieren.

Der Sandwichkomplex wurde basenkatalysiert mittels zyklischer Tetramerisierung unter Verwendung eines Metalltemplateffekts synthetisiert, anschließend chromatographisch abgetrennt und aufgereinigt.

Die Charakterisierung beinhaltet ein und zwei dimensionale NMR Techniken, elektronische und Schwingungsspektroskopie sowie eine massenspektrometrische Analyse. Dabei stellte sich heraus, dass der dimere Komplex kaum eindeutige Signale liefert, die Rückschlüsse auf dessen Struktur erlauben. Dennoch ist es möglich den elektronischen Zustand anhand redoxsensitiver Banden zu identifizieren.

Kohärente zwei-dimensionale elektronische Spektroskopie stellt ein wertvolles Mittel zur Untersuchung von molekulardynamischen Prozessen wie Wellenpaketen, elektronischem Energietransfer oder Ladungstrennung dar. In weiterem Verlauf wird ein multifunktionaler Aufbau beschrieben, der es ermöglicht diese Prozesse in Echtzeit zu verfolgen. Das Dimer sollte ursprünglich als biomimetrisches Modellsystem zur Untersuchung des Beitrags von elektronischen Kohärenzen zur Effizienz von Lichtsammelsystemen dienen. Es stellte sich heraus, dass jegliche Beiträge durch eine extrem schnelle Populationsdynamik ausgelöscht werden, diese aber ein neues Detail in der elektronischen Struktur des Bisphthalocyanins freigibt.

Mögliche Modelle die dessen Ursprung aufklären könnten, werden im theoretischen Teil unter Zuhilfenahme quantenchemischer Rechenmethoden diskutiert. Die Dimension des behandelten Systems erfordert eine Berechnung mittels Dichtefunktionaltheorie. Das Vorhandensein verschiedenartiger elektronischer Zustände kompliziert die Simulation und schränkt die Genauigkeit der Ergebnisse stark ein. BHLYP erwies sich als geeignetstes all-round Funktional, speziell für die Berechnung von charge-transfer Anregungsenergien. Die Einbeziehung des Gegenions, lieferte eine Aufspaltung der elektronischen Zustände, die die experimentellen Beobachtungen reproduziert und deutet auf eine Asymmetrie des Dimers hin, die wahrscheinlich zu einer partiellen Ladungstrennung führt.

Abstract

In this thesis a lutetium bisphthalocyanine double-decker complex is synthesized to study the interaction of the macrocyclic ligands on ultrashort timescales with special concern on the elementary processes of energy transfer and charge separation.

The molecular dimer is prepared by a metal template assisted cyclic tetramerization reaction under basic condition in the bulk phase at elevated temperature following chromatographic separation and purification by recrystallization.

The spectroscopic characterization includes one and two dimensional NMR, vibrational and electronic spectroscopy as well as mass spectrometry. It is found that the symmetry of the molecular structure leads to few signals in all of the aforementioned spectroscopic techniques. Despite these difficulties, it is possible to assign the electronic state by inspection of some redox sensitive marker bands.

Coherent two-dimensional electronic spectroscopy (2D-ES) provides a versatile tool for investigating molecular dynamics in real time. The observable processes include nuclear wavepackets, electronic energy transfer and dissipation just as charge transfer dynamics. A multifunctional non-linear spectroscopy set-up capable of following these processes in the visible spectral range is described and applied to the synthesized phthalocyanine dimer. The work intended to focus on recently discussed importance of electronic coherences to energy transfer in biological systems by using this relatively simple model system. However, it turned out that the induced dynamics are dominated by an ultrafast initial population decay that extinguishes all possible electronic coherences but exposes a previously unseen feature in the electronic structure through asymmetric recovery of the missing low energy cross-peak. Possible scenarios to account for its emergence are tackled by quantum chemical calculations.

Computation of the electronic structure is vital and an elementary step in the discussion of excited state processes. The sheer size of the considered system and different state characters make theoretical modeling cumbersome and restrict it to DFT methods. A test of various functionals marks B3LYP as most suitable for calculating charge transfer excitation energies. Association of the anionic dimer complex with the TBA counterion leads to structural asymmetry of the rings that lifts the degeneracy of states thus doubling the number of transitions and altering their character.

Table of Contents

Introduction	-1-
(a) Phthalocyanines	-1-
(b) Lutetium Bisphthalocyanines	-2-
(c) Two-Dimensional Electronic Spectroscopy	-3-
Lutetium(III)bisphthalocyaninato-tetrabutylammonium: [LuPc ₂] ⁻ TBA ⁺	-4-
1. Synthesis	-4-
(a) General Aspects	-4-
(b) Reaction Mechanism MPcs	-5-
(c) Reaction Apparatus	-7-
(d) Synthetic Procedure	-7-
(e) Variation of Reaction Conditions	-11-
2. Characterization	-12-
(a) Elementary Analysis	-12-
(b) NMR	-13-
a. ¹ H	-13-
b. ¹³ C	-16-
c. COSY	-18-
d. HSQC	-19-
e. HMBC	-20-
(c) Electronic Spectroscopy	-21-
a. UV-VIS	-21-
b. Fluorescence	-23-
(d) Vibrational Spectroscopy	-24-
a. IR	-24-
b. Raman	-27-
(e) Mass Spectrometry	-28-
a. ESI	-28-

Theory	-29-
3. DFT Calculations	-29-
(a) Calculation of the ground state.....	-30-
(b) Calculation of normal modes.....	-35-
(c) Calculation of the excited states	-36-
(d) Computational details	-42-
(e) Results	-43-
4. Non-Linear Spectroscopy Theory	-59-
(a) Introduction	-59-
(b) System-Bath Interactions	-61-
(c) System-Field Interactions.....	-66-
(d) Third-Order Spectroscopy: Four-Level System	-70-
Ultrafast Spectroscopy	-74-
5. Experimental Ultrafast Spectroscopy	-74-
(a) Lasersystem	-74-
(b) Non-Linear Optical Parametric Amplifier (NOPA).....	-75-
(c) Pulse Compression	-76-
(d) Pulse Characterization.....	-77-
(e) Calibration	-78-
(f) Set-Up	-79-
(g) Implementation of Non-Linear Spectroscopies	-81-
(h) Data processing	-87-
6. Results Ultrafast Spectroscopy	-89-
(a) PP.....	-89-
(b) 2D-ES	-96-
Literature	-105-

Introduction

The introduction aims to give an overview of phthalocyanines, to highlight the importance of the dimeric lutetium double-decker complex as an electronically coupled toy system and to establish 2D-ES as a valuable tool for disentangling molecular interactions in real time.

(a) Phthalocyanines

Their exceptional electronic and optical properties, excellent stability and chemical pliability recently raised increasing interest in phthalocyanines (Pcs) as functional organic materials. Various potential applications at the interface of chemistry, physics and material science make them attractive research targets for technological devices [1-53].

Pcs and their metal derivatives comprise two-dimensional, planar ring system with alternating carbon-nitrogen bonds throughout the inner macrocycle. The aromatic 18 π -electron system of the shortest cyclic conjugated path marks them as synthetic analogues of porphyrins [4, 7, 54]. High symmetry, strong linkages of the four isoindole units via aza-bridges and an extension of the conjugated system by benzene groups fused to the pyrrole C_{α} carbons account for their outstanding chemical, thermal, optical and environmental stability [4, 6, 7, 19, 54].

The unique electronic and optical traits of Pcs and MPcs are a consequence of the delocalization of their charge density over the macrocycle and the resulting high degree of charge carrier mobility [4, 7]. Modifications of the electronic structure by substitutions and simultaneous control over their assemblies allow for fine-tuning of the required characteristics and tailoring to the type of use [6, 55]. Chemical flexibility, relatively straight forward implementation and a rich supermolecular chemistry [34] steadily improve their scope, while profound thermal stability guarantees general processability. Electronic properties based on the substantial redox activity of the macrocycle and formation of various stable redox states favor applicability in the areas of molecular electronics [21, 22, 28, 29, 39-41, 46] and catalysis [42, 43, 48-50]. Striking optical and photophysical attributes in the visible and NIR due to intense absorption and easy tuning of spectral features via peripheral and skeletal substitutions, change of central metals, coordination environments and / or oxidation state account for their popularity in optoelectronics [8, 12, 34], photovoltaics [10, 14, 17, 18, 23, 27, 30] and medicine [2, 9, 24, 26, 31, 37]. Control over the morphology of their mesoscopic architectures in condensed phases through interplay of different interactions like ionic assembly, metal-ligand coordination, π - π and van der Waals interactions awards Pcs for incorporation as building blocks for nanotechnological devices [1, 4, 7, 13, 20, 25, 28, 32, 33, 36-38, 44, 45, 52, 53].

Their central four-dentate ring cavity provides hosting abilities for 70 cations [56] which implies operations in ionoelectronics.

Current research involves improvement of established scopes in virtually all afore mentioned areas including

- electronics: semiconductors [29, 46], OFET [39], electrochromic devices [21, 22]
- optoelectronics: OLED [12], optical switching and limiting devices [57, 58], second and third order non-linear optical materials [8, 34, 59]
- spintronics: single molecule magnets [34, 40, 41, 60]
- photovoltaics: low bandgap [18, 30] and dye-sensitized solar cells [10, 14, 17, 23, 27]
- information technology: data storage [11, 16] and quantum computing [51]
- nanotechnology: thin films [28, 36], building blocks and templates in form of polymers [20, 53], dendrimers [44, 52], discotic liquid crystals [13, 25] just as supermolecular motifs [1, 4, 7, 32, 33, 36-38, 45] and molecular machines [61, 62]
- medicine: sensitizers for photodynamic therapy [2, 9, 24, 26], labeling and imaging agents [31, 47]
- catalysis: oxidations of secondary alcohols [48] and aromatic compounds [50], epoxidation of olefins [49], allylic amination [42] or electrocatalytic reactions [43]
- environmental science: sensing [35, 39], photocatalytic degradation of pollutants

(b) Lutetium Bisphthalocyanine

Among the large family of phthalocyanines, double-decker phthalocyanines, and especially the lutetium derivatives, have been subject of extensive investigations due to their intrinsic semiconductivity [35, 46, 63, 64] and electrochromic behavior [21, 22, 64-70]. Bisphthalocyanines comprise two macrocyclic moieties held together at a fixed distance determined by a rare earth cation or an organic spacer [54, 71-73]. In its ground state LuPc₂ is a mixed-valence compound, that is, a stable radical delocalized over both rings with an intermediate oxidation state of -1.5 on each ring [74]. The close proximity of the two Pc rings offers the chance to study fine variations in excitonic interactions and their impacts upon charge carrier generation [75, 76]. An interplay of excitonic (EX) and charge-transfer (CT) states [77-80] in redox active macrocycles enjoys considerable attention in the fields of photovoltaics and photosynthesis research with regard to the accompanying changes in physical properties. Due to its structural and electronic similarities [77, 81] it can be seen as a biomimetic model system for studies of the special pair [74, 82], a magnesium porphyrin dimer, of central importance for photoinduced charge separation in bacterial photosynthetic reaction centers. A direct observation of such processes is usually complicated by rather small optical cross sections of excited CT states. In its reduced form, lutetium bisphthalocyanine [LuPc₂]⁻, exhibits energetically lowered CT states that intermix with

nearby EX states and thereby gain transition intensity [77-80]. Such an electronically coupled dimer resembles a simple aggregate with few excitonic (delocalized, collective) states that is well suited for exploring excitation energy and charge transfer dynamics along its system sites and accompanying losses due to the interaction with its environment.

(c) Two-Dimensional Electronic Spectroscopy

Two-dimensional electronic spectroscopy (2D-ES) provides the unique possibility to monitor and characterize transient changes of the electronic molecular structure and to disentangle intermolecular interactions on femtosecond timescales [83-86]. Tracking the evolution of electronic excitations, directly reports on the very heart of chemistry since changes of transition dipoles are sensitive to relative distances and orientations of the involved molecular structures. The femtosecond resolution allows to probe these changes in real time. 2D-ES yields increased information as compared to time-resolved linear absorption spectroscopy by spreading out and correlating the averaged recorded data on an additional dimension [87-89]. 2D spectra display interrelations of species as characteristic cross-peaks. This fact emphasizes its application as a versatile tool for sensing molecular linkages and enables one to determine their underlying microscopic mechanisms. Evolving couplings [83, 90] and 2D-lineshapes [91-93] provide information on intersystem and system-bath interactions that determine excitation energy and charge transfer dynamics [84, 94-96]. A change in the couplings signals intra- and / or intermolecular interactions while lineshapes yield knowledge about the environment and its perturbations on the system potential energy surface. Modulations of cross-peaks might arise either from changes in the couplings caused by intramolecular vibrations or from mutual intermolecular influences. Diagonal widths of lineshapes reflect prevalent distributions of static system oscillators due to the instantaneous configuration of the surrounding bath while anti-diagonal widths give intrinsic system energetics and their changes due to redistributions [97].

Although recent investigations of various large scale molecular systems [98-104] already revealed exquisite details of energy transfer and trapping mechanisms, moderately complicated, handsome toy systems can provide easy and profound access to the relevant modeled interactions. Naturally a detailed survey of small systems composed of a comprehensible number of components yields detailed understanding of their functions and mutual interactions that can be extended to larger entities.

1. Synthesis of Lutetium Bisphthalocyanine

The synthesis of the lutetium(III)bisphthalocyaninato-tetrabutylammonium salt $[\text{Lu}^{\text{III}}(\text{Pc}^{2-})_2]^- [\text{N}(\text{n-Bu})_4]^+$ is carried out via a base catalyzed cyclotetramerization reaction of phthalonitrile with lutetiumacetate in the bulk-phase at elevated temperature.

The synthesized compound is characterized by means of elementary analysis, nuclear magnetic resonance (NMR), electronic ultraviolet-visible (UV/VIS) and fluorescence as well as vibrational infrared (IR) and Raman spectroscopies just as mass spectrometry.

Metal-ligand bonding

In its most stable oxidation state lutetium exists as an electropositive trivalent ion in the electronic configuration $[\text{Xe}] 4f^{14}$. In this state the neutral atom has lost its $5d^1$ and $6s^2$ valence electrons and retains a closed $4f$ shell that is located inside the ion (underneath the $5s^2$ and $5p^6$ orbitals) due to the lanthanoid contraction. The small overlap with the macrocyclic ligand orbitals contributes very little to chemical bonding so the interactions holding the complex together are mainly electrostatic in nature ^[105]. Rare earth cations are usually considered as an inert spacer between the dianionic phthalocyanine ligands and the resulting organometallic chemistry is dictated by their relatively large sized ions, their high Lewis-acidity and the tendency to be present at high coordination numbers ^[105].

(a) General aspects of the synthesis

The synthesis is implemented referring to known procedures from literature, especially those from Koike ^[106] and Konami ^[107].

These synthetic compositions rely on the most simple approach where a mixture of the corresponding metal salt and phthalonitrile is stepwise heated in the bulk phase (without use of a solvent) to 280 °C until solidification of the melt signals completion of the reaction (after one to four hours) following chromatographic purification of the resulting reaction products ^[108].

This phthalonitrile method owes the benefits that the crude reaction products contain less contaminations than comparable reactions starting from other precursors since each phthalonitrile corresponds to one eighth of the formed complex and hence only side reactions associated with different polymerization states occur ^[19].

In absence of a base the reaction proceeds to the radical sandwich dimer referred to as the green form or the neutral species as the main reaction product since the trivalent oxidation state of the rare earth cation requires balancing of charges by three electrons. Addition of alkaline reagents (bases or lyes) leads to partial formation of the respective reduced form (blue form) of the complex [54, 73].

The excess, unreacted phthalonitrile and thermally labile by-products can be removed from the melt by sublimation (reducing pressure to less than 1 Torr at 280 °C) after the reaction has ceased. This is due to the unusually high thermal stability of phthalocyanine sandwich compounds.

This cleaning firm is advantageous in that it considerably eases the following chromatographic purification step with regard to preparative scales since phthalocyanines (Pc) generally exhibit strong tendencies to aggregate in solution [54].

The chromatographic separation is progressed by flushing the dissolved crude reaction mixture over solid aluminium oxide in a polar mobile phase under basic conditions to stabilize the anionic species and protect it against protolysis.

The anionic fractions are precipitated through addition of the non-nucleophilic (sterically hindered) cation tetrabutylammoniumbromide (TBA^+Br^-) and crystallized.

(b) Reaction mechanism

Cyclotetramerization reactions are strongly exothermic and usually take place under drastic conditions that complicate the elucidation of their formation mechanisms [54].

The afterimage [109] depicts the proposed scheme of the base catalyzed cyclic tetramerization reaction of metal phthalocyanines under influence of a kinetic metal template effect [110].

Therein the metal cation serves as an activating agent polarizing the nitrile group and furtheron functions as an anchorage point for guiding the assembly of reactive units [110].

The base acts as a catalyst initiating the dinitrile cyclization through its electrophilic attack on the activated carbon [110]. The latter then starts to react intramolecularly with the second nitrile function in a nucleophilic addition reaction yielding isoindolinimine as an intermediate [54].

The tetramerization proceeds onward via oligomers created from sequential additions of phthalonitrile monomers complexed nearby to the central metal cation.

The last step in the ring formation is believed to be the closure of a metal-coordinated non-planar open-chain tetramer where the dissociation of the base yields the desired phthalocyanine [54].

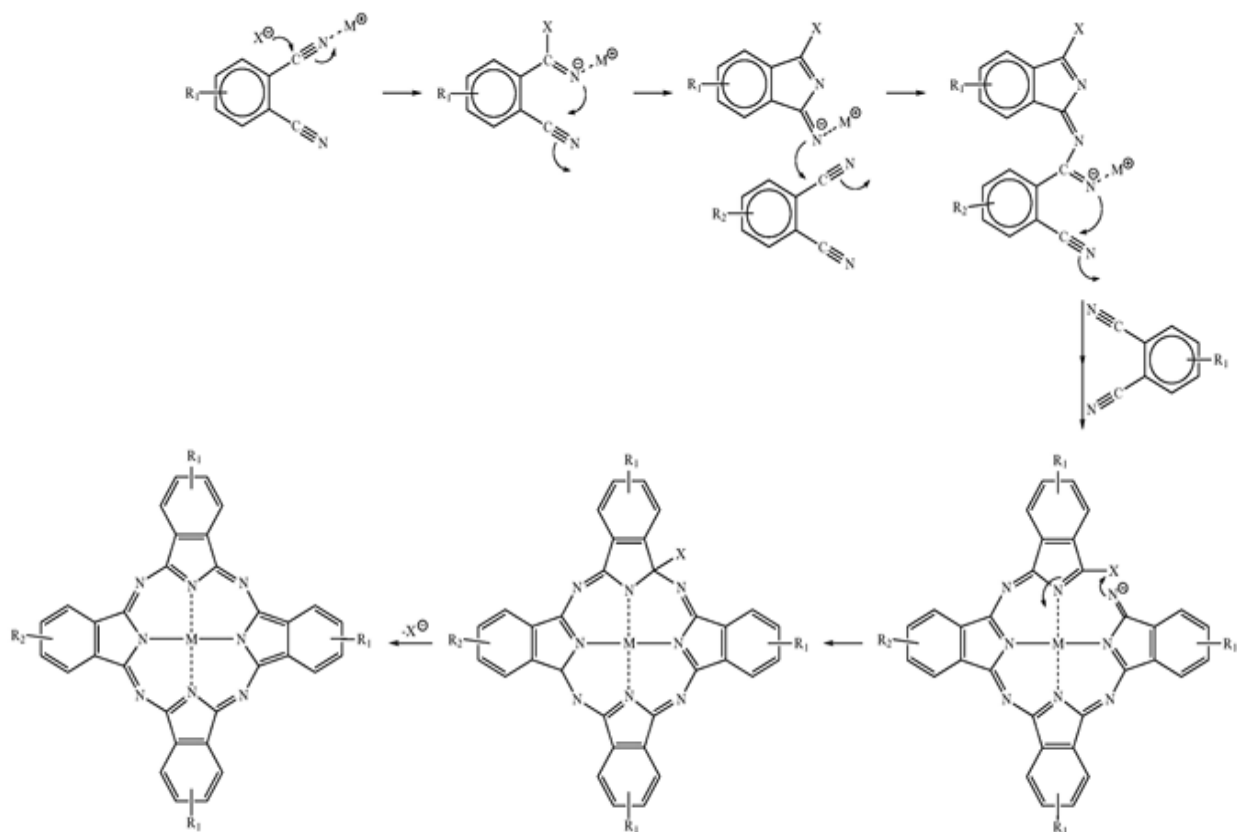


Figure 1: Steps in MPc formation [109].

The preferred formation of a sandwich structure is attributed to the size and coordination requirements (coordination numbers eight, nine or ten) of the lanthanoid ion [105]. Since a rare earth metal is too large to completely fit into the central cavity [19] of one phthalocyanine moiety alone the spatial arrangement of intermediates in its coordination shell favors to lock up another macrocycle when additional coordinating ligands are mostly absent or loosely bound due to the harsh reaction conditions.

Typically the observed product distribution of base catalysed reactions involves mixtures of diphthalocyanines in different redox states. Their appearance is rationalized by one-electron reductions of the reactive phthalonitrile units or reduction of the open-chain tetramer intermediates during ring formation. In investigated MPc formations, either the central metal in a less oxidized state or the base itself act as reducing agents [54, 111].

However in the applied synthetic approach the catalyzing base cannot be the reducing agent since it already appears in the most oxidized state. The rare earth acetate indeed undergoes thermal decomposition near the reaction temperature to the rare earth metal oxide, CO₂ and acetone [112] but neither of them is oxidizable. Coordinated crystal water is thought not to participate in the reduction process since similar products are obtained when using highly dried precursors. Accordingly it has been argued that dissolving the crude reaction product might reduce the complex [113].

(c) Reaction apparatus: Kugelrohr (ball tube)

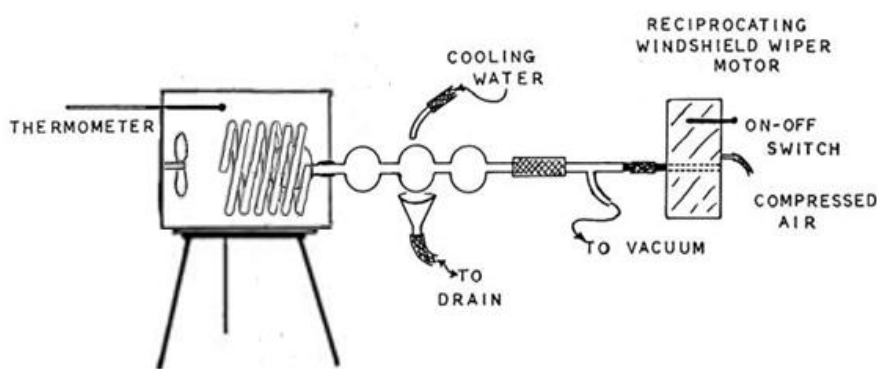


Figure 2: Scheme of the ball tube apparatus used to carry out the reaction [114].

The apparatus consists of a sealable chamber equipped with a fan that provides uniform air circulation, a digital thermostat to control ambient temperature and a central bulb containing the reaction mixture. The chamber is heated via a coil surrounding the reaction bulb which is obliged to a transformer and the thermostat. Outside the reaction chamber three additional interconnected, water-cooled round flasks are used to collect distillates sequentially by condensing the passing vapors. A glass joint downstream the cooling stage connects the apparatus to a vacuum pump. A motor drive is used to rotate the string of bulbs to increase intermixing of the melted reagents.

(d) Synthetic procedure:

Reagents

All reagents were purchased from Sigma Aldrich and used as received without further purification. Solvents are applied in their absolute forms.

Reaction equation

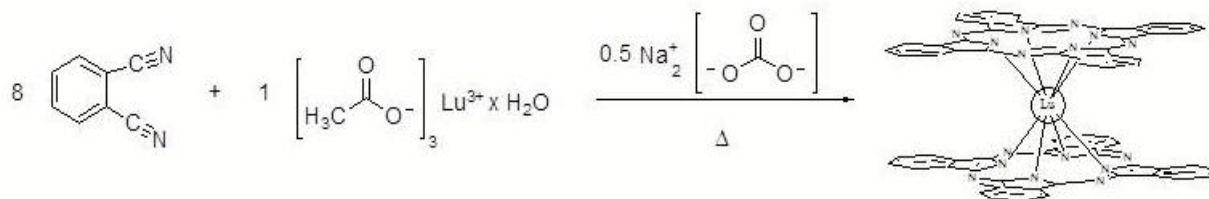


Figure 3: Reaction equation for the double-decker formation.

The synthesis yields several by-products [19, 74, 115] among others the unreacted metal salt $\text{Lu}(\text{OAc})_3$, metalphthalocyanine MPc, free base phthalocyanine H_2Pc , triple-decker phthalocyanine M_2Pc_3 and bicyclic phthalocyaninate (MPcc).

Stoichiometric amounts

The reaction run-up comprised 4.1 mmol o-dicyanobenzene or phthalonitrile, $\text{Ph}(\text{CN})_2$, (0,1 mmol excess), 0.5 mmol lutetium acetate hydrate, $\text{Lu}(\text{OAc})_3 \times \text{H}_2\text{O}$, as limiting agent and 0.25 mmol sodium carbonate, Na_2CO_3 , as catalyst. This mixture corresponds to a ratio of phthalonitrile : Lu : base of 8 : 1 : 0.5 and is equivalent to the perception that four aza-bringed benzopyrrole units constitute one macrocyclic ring so that each lutetium ion will be sandwiched in between two of these phthalocyanine ligands (eight phthalonitrile monomers in total). The reaction is catalyzed by 0.5 equivalents of base. The residual excess of 0.2 equivalents to the concentration of phthalonitrile assures a complete reaction.

Implementation

In order to avoid disrupting interferences all used glass wares were carefully dried and the whole apparatus was purged with Argon to exclude possible oxidation of the Pc moieties [116, 117].

The reaction has been implemented as follows:

- Outweighing stoichiometric amounts & proper mixing
- Kugelrohrdestillation under Ar atmosphere and constant mixing
 - 150 °C: 20' heating / 30' keep at specified temperature
 - 280 °C: 15' heating / 20' keep at specified temperature
 - 280 °C + vacuum (< 1 Torr) for 1 hour

- Cool to room temperature and crush crude reaction product
- dissolve in CH₃CN (abs.) on ultrasonic bath
- filtrate with suction filter and constrict
- column chromatography to separate products

· AlOx 90, neutral, activity grade I

· MeOH / MeONa (0,2 %)

- check quality in UV/VIS and collect fractions
- rotary evaporation and addition of (n-Bu)₄N⁺Br⁻
- crystallization at -30 °C for 2 days
- purification by washing with DMF
- dry on vacuum line for 2-3 days

During the heating periods the temperature is raised slowly to allow for proper mixing of the melted solids and to create a homogeneous blend.

A summary of the most evident observations during preparation period comprises:

- liquefaction at T > 145 °C to a brown granular and viscous mass
- mixture turns to brownish liquid during constant interval at T = 150 °C
- discoloration from brown to light brown plus crumbly solid residue at T > 160 °C
- appearance of a light greenish glimmer accompanied by a color change to dark green during heating period to T=280 °C
- change-over to dark blue in the course of constant heating at T=280 °C
- sublimation at T=280 °C under reduced pressure < 1 Torr causes white vapor fumes to rise that condense as white needles in the downstream water cooled flask
- dark blue to black solid with violet gloss left over
- dissolving crude reaction mixture in CH₃CN yields a dark blue solution and a black unsoluble residue (probably elementary carbon)

After comprehensive filtering of the received solution the mixture is separated in a preparative chromatographic column filled with an amount of stationary phase (AlOx 90, neutral, activity grade I) that equals the 80-fold quantity of the theoretical reaction turn-over (~ 50 g).

Basic methanol containing 0.2 v/v % sodium methanolate (MeONa), prepared by dissolving 1.6 g Na in 1l of MeOH (abs), is used as mobile phase.

The fractions appeared in a satisfying time-ordering

- starting with some yellow volume (with an unstructured UV/VIS spectrum),
- followed by a smooth passage to pure radical dimer (green),
- then the main green band,
- a mixed fraction of green and blue eluate,
- pure blue reduced species
- and some undesirable blue quantity.

The collected eluate made up approximately 20 fractions à 5 ml with a ratio of dark green to dark blue of around 1:4.

The fractions were checked for compliance with published UV/VIS spectra on the fly and the appropriate ones were collected, crystallized and purified. The used instrument was a Shimadzu UV mini 1240 UV/VIS spektrometer (λ -range: 200 nm - 800 nm, scan speed: medium, No. of scans: 1) where each measurement was referenced to pure solvent (0,2 v/v % MeONa / MeOH).

After rotary evaporation an amount of 81 mg TBA⁺Br⁻ corresponding to an expected yield of 50 % of the full theoretical conversion was added and after crystallizing the excess salt was partially removed by washing the obtained crystals with ice-cooled DMF (abs.).

The practical yield after three days of drying on the vacuum line amounts to 36.6 mg of product (M ([LuPc₂]⁻ [N(n-Bu)₄]⁺) = 1442,52 g/mol) which equals 5 % of the theoretical turn-over.

(e) Variation of reaction conditions

The described procedure employing a tenfold stöchiometric amount resulted in little change of the product count. Such an indifference suggests a dominant role of the metal template effect since ring formation reactions usually proceed via statistical reunion of their ends and are thereby sensitive to concentration effects.

A test to improve the amount of reduced product included adding the reducing agent hydrochinon under basic reaction conditions.

In this attempt a ratio of phthalonitrile : Lu : base : reducing agent of 8 : 1 : 1.5 : 0.5 was used since one electron (or 0.5 eq.) is necessary for the reduction of each sandwich complex. Accordingly 1 equivalent of base is needed to neutralize the released two protons from the oxidized hydrochinon. Again on top of this an excess of 0.5 eq. of base acts as catalyst.

Although there was a net increase in the reduced form this approach unfortunately led to troubles in the described chromatographic procedure (incomplete separation) and resulted in partial alterations of the spectra in the UV region (probably due to the addition of benzochinone into the ring system).

Additional remarks

During the synthetic work it turned out that the reduced double-decker complex is rather sensitive to protolysis so special care has to be taken during the preparation with regard to the used solvents (absolute aprotic ones only) and storage conditions (e.g. unfreezing, avoidance of moist air). Low levels of humidity in surrounding air are unproblematic but long exposure should possibly be avoided.

Under proton addition the reduced species (blue) reacts to the radical form (green) so the sensitivity to proto- and hydrolysis can be correlated with the proposed redox equilibrium [66, 118-120].

Both the radical and the reduced species are stable with respect to oxygen [118].

2. Characterization of lutetium bisphthalocyanine

The synthesized compound is investigated spectroscopically as a quality check of the applied methodology. Device specifications are given in appendix A.

(a) Elementary analysis

Elementary analysis combusts the sample in an element specific way and measures the amount of produced gases. The obtained mass percentages are then used to back-calculate the sum formula. The sample was tested microanalytically with respect to the elements carbon, hydrogen and nitrogen. The following mass percentages $\%w_x = \frac{m_x}{m_{dimer}}$ of these elements were obtained.

Measured quantities (%w/w):

Lu: not determined, C: 30.95, H: 3.75, N: 6.34

The amount of a component is evaluated according to $X = \%w_x \cdot \frac{m_{dimer}^{exact}}{m_x \cdot 100}$ which results in a reconstructed sum formula of $C_{37}H_{54}N_7$. This clearly contradicts the theoretical predicted values of Lu: 12.13, C: 66.61, H: 4.75, N: 16.51 (%w/w) for $LuC_{80}H_{68}N_{17}$.

The deviations might be rooted in an incomplete combustion processes or trace back to insufficient drying of the complex.

One possible explanation could lie in the mineralization process of metal-containing compounds. It often yields diverse problems associated with the formation of either thermally indecomposable components like oxides and carbonates or metastable compounds which are only slowly degrading.

Besides it's likely that the thermally extremely stable tetrapyrrole complex itself prevents complete burning and leads to acquisition of pyrolysis intermediates and/or incombustible reaction products. This would especially account for the large inconsistencies in the nitrogen and carbon values.

Other reasons affecting the accuracy could be persistent attachment of crystal-water or solvent molecules to the complex. The applied synthetic reagents could not be obtained completely waterfree and solvent molecules might have not evaporated under the used drying conditions. The large extent of deviations makes it impractical to seek for water or solvent contributions in the recorded data.

(b) Nuclear magnetic resonance (NMR)

All recorded NMR spectra indicate highly symmetric structure consistent with the point groups D_{4d} , D_{4h} or a time-averaged configuration (spinning of the rings) [107].

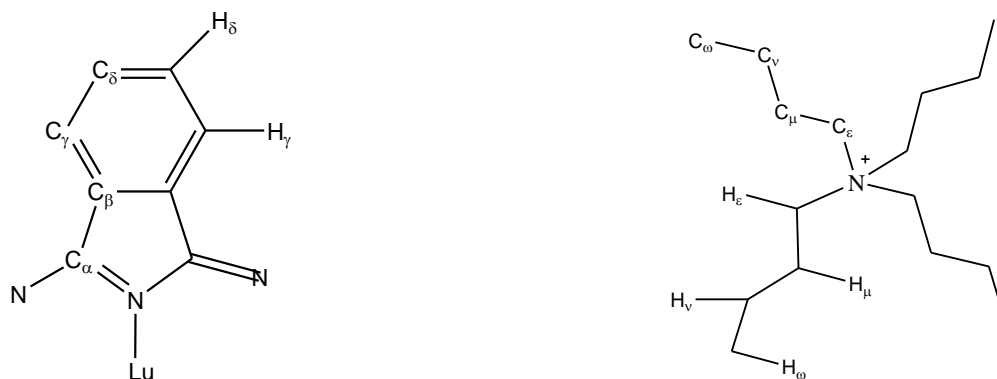


Figure 4: Applied nomenclature to the observed NMR signals of the dimer complex (left) and the TBA counterion (right).

Symmetry

A listing of the symmetry elements [121] constituting the molecular point group is essential to the interpretation of all spectroscopic disciplines and is therefore mentioned.

$$D_{4d} (4\sigma_d \parallel C_4) \rightarrow \text{symmetry elements: } E, C_4, 4C_2, 4\sigma_d, S_8$$

The point group D_{4d} forbids a dipole moment due to the presence of the C_4 axis and the four C_2 axes since the dipole vector can not simultaneously point in several directions [122].

a. $^1\text{H-NMR}$

The $^1\text{H-NMR}$ spectrum in DMSO is conspicuously simple in that it only displays two signals that can be associated with the phthalocyanine macrocycles.

The absence of additional proton peaks can be explained by symmetry considerations since molecular parts that exhibit the same transformation behavior are chemically equivalent and will thus lead to the same chemical shift. The main rotation axis (C_4) transforms all four isoindolinimin units constituting a ring into each other so only the protons of one benzene unit per phthalocyanine remain to be spectroscopically distinguishable. Protons situated on opposite sides of each benzene ring are mapped onto each other by dihedral mirror planes (σ_d) that are vertically intersecting the benzopyrrole units. The dihedral two-fold axes (C_2) identify hydrogens in the foreground on the upper benzene unit with the ones in the background on the

lower ring. Together these symmetries allow only for two evaluable proton species denoted H_γ and H_δ .

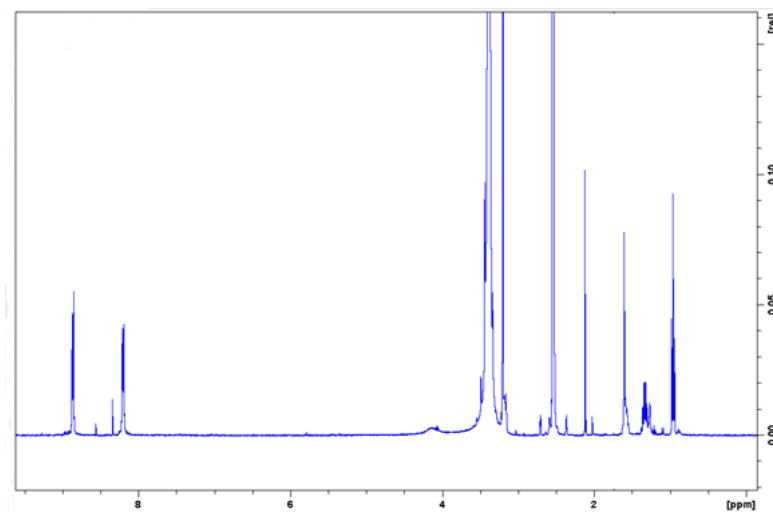


Figure 5: ^1H -NMR spectrum of $[\text{LuPc}_2]^- \text{TBA}^+$ in DMSO.

Both of them correspond to aromatic protons of the benzene groups and exhibit markedly high chemical shifts even though the reduced dimer complex is diamagnetic.

The low field shift (large δ -values) of peripheral protons is mainly caused by a deshielding effect ascribed to the ring current characteristic to cyclic, conjugated systems ^[123]. The induced field of the circulating π -electrons enhances the applied magnetic field H_0 on the outside of the macrocycle and thereby deshields these nuclei while the resulting field counteracts H_0 in the inner regions and shifts those protons to higher field (low chemical shifts).

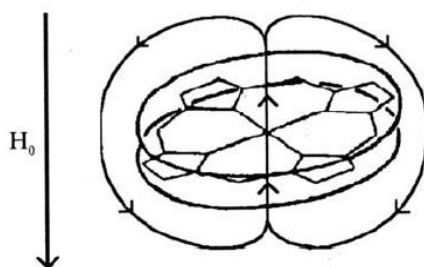


Figure 6: Depiction of the aromatic ring current counteracting the applied magnetic field in the inner regions of the macrocycle and enhancing it on the periphery ^[124].

Considering the ring current effect on the locations of the ring protons it is deduced that the low field multiplet at 8.20 ppm corresponds to H_γ and the high field multiplet at 8.86 ppm is then assigned to the H_δ species.

Another factor that strikingly influences the chemical shift is the change in charge density upon transition from neutral system to anionic complex [123]. In this case the increased shielding moves the signal downward on the ppm scale.

A change in chemical shifts due to steric effects, that is the deformation of electronic charge distributions by force of van der Waals interactions between adjacent groups (deshielding effect) will be rather small because of concave distortions of the ring periphery and is probably covered by the other effects.

The observed diamagnetic ring current anisotropy (outer protons deshielded, inner ones more shielded) is regarded as a qualitative criterium of aromaticity and the $4n+2$ π -electronic character of the system [123].

The multiplett structure (quadruplet) of each proton signal arises from a higher order effect between mutual 3J and 4J couplings of H_γ / H_δ within one benzene unit.

The H_δ signal is a bit broader and of higher intensity than H_γ . Since intensities in 1H -NMR spectra are proportional to the number of H-nuclei the integrated peak areas can be used to determine compositional percentages of hydrogen atoms in the molecule to cross-check the result of elementary analysis. The intensity of H_γ was normalized to 16 and compared to the other recorded values. The intensities of the ring protons are slightly lower (10%) than the TBA signals. This is probably caused by insufficient purification of excess TBA but is otherwise in accordance with the expected values. It is therefore concluded that elementary analysis gave incorrect results for the mentioned reasons.

Except the two aromatic proton signals no other strongly shifted peaks could be identified in the recorded region that lead back to coordinating water or protonation of the isoindole nitrogens. Any present crystal water would exhibit a larger chemical shift as compared to free water molecules originating from its proximity to the ring system since it was found to be H-bonded on the periphery of the complex [125]. Protons on the inner isoindole nitrogens will be shifted to lower δ -values and are expected around -10 ppm. The latter region was not covered by the recording routine and its presence can therefore not be excluded.

A similar spectral simplicity is observed in the shift region of the dissolved TBA protons so that likewise a highly symmetrical structure is assumed [107].

TBA signals are assigned by considering the inductive influence of the ammonium nitrogen onto the charge distributions of its surrounding protons which yields H_ϵ at 3.17 ppm, H_μ at 1.57 ppm, H_ν at 1.31 ppm and H_ω at 0.96 ppm.

A broadening of the $[\text{LuPc}_2]^-$ signals as compared to those of TBA may result from an altered relaxation through presence of the rare earth ion or existence of some radical dipthalocyanine. Aggregation phenomena are assumed to be absent due to the association with the bulky TBA cations.

Table 1. $^1\text{H-NMR}$ shifts, multiplicities and intensities of $[\text{LuPc}_2]^- \text{TBA}^+$ in DMSO. Multiplicities are abbreviated s for singlets, t for triplets, q for quadruplets and m for unresolved multiplets. The intensities have been normalized to the expected value of 16.

H_n	δ [ppm]	multiplicity	Intensity
H_γ	8.86	q	16
H_δ	8.20	q	16
H_ϵ	3.17	s	
H_μ	1.57	m	17
H_ν	1.31	m	17
H_ω	0.96	t	17
H_{HOD}	3.30	s	1875
H_{DMSO}	2.50	m	262

b. $^{13}\text{C-NMR}$

By reason of the same symmetry elements only four observable carbons can be identified.

In contrary to ^1H spectra, the ring current effect in $^{13}\text{C-NMR}$ does not contribute as much to the shift of ring carbons resulting in a similar absorption range of aromatic and olefinic carbons [123]. The ^{13}C -shift positions are strongly influenced by the hybridization of the considered carbons owing to large paramagnetic shieldings by the p-electrons. Therefore sp^2 -hybridized carbon atoms of the macrocycle absorb at lower field (higher δ) than sp^3 ones of the TBA cation.

As the absorption range in ^{13}C excesses a larger region the influences of any change in the chemical environment has more profound effects on chemical shifts. This means that the spectrum displays the presence of distant inductive groups and distinguishes those carbons that are closer to electronegative nitrogens by a high chemical shift.

In the same way, different alkylation patterns give the chemical shift series: $\delta C_{\text{prim}} < \delta C_{\text{sec}} < \delta C_{\text{tert}} < \delta C_{\text{quart}}$.

Further on the assignment of the carbon atoms are cross-checked by comparison of ^1H -coupled and decoupled ^{13}C -spectra.

In the ^1H broadband decoupled spectra C_q and CH_2 signals are facing upward while CH_3 and CH are pointing downwards.

The phthalocyanine carbons are assigned as C_α at 154 ppm, C_β at 138 ppm, C_γ at 128 ppm and C_δ at 122 ppm.

The TBA carbons associated with the following shifts: C_ϵ at 57.89 ppm, C_μ at 23.41 ppm, C_ν at 19.57 ppm and C_ω at 13.84 ppm.

^{13}C - ^{14}N couplings are usually not revealed because the nuclear quadrupole moment of ^{14}N leads to fast relaxation so that the coupling is hidden in the line width. However, in the case of TBA it is seen since its electric field gradient is rather weak.

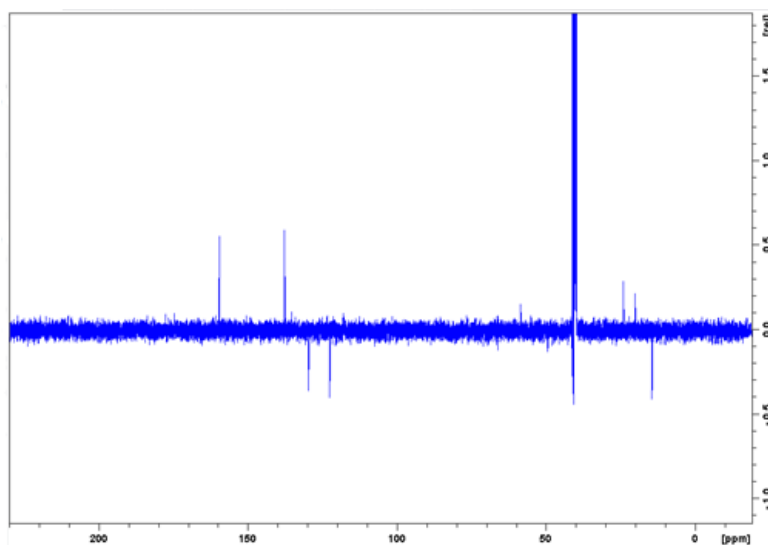


Figure 7: ^{13}C -NMR spectrum of $[\text{LuPc}_2]^- \text{TBA}^+$ in DMSO.

In the routine ^{13}C -NMR spectra no quantitative statements about the intensities of the individual peaks can be made as their population differences are affected by different relaxation and NOE patterns [123].

Table 2. ^{13}C -NMR shifts, amplitudes and assignments of $[\text{LuPc}_2]^- \text{TBA}^+$ in DMSO.

C_n	δ [ppm]	amplitude	assignment
C_α	158.96	pos.	Q
C_β	137.15	pos.	Q
C_γ	129.00	neg.	CH
C_δ	121.91	neg.	CH
C_ϵ	57.89	pos.	CH_2
C_μ	23.41	pos.	CH_2
C_ν	19.57	pos.	CH_2
C_ω	13.84	neg.	CH_3
C_{DMSO}	39.5		

c. COSY

Correlation spectroscopy (COSY) shows proton connectivities by revealing spin-spin-couplings up to three bonds between vicinal hydrogens. A 2D plot of ^1H chemical shifts on both axes visualizes existing correlations between them. Diagonal peaks ($\delta_i\delta_i$ and $\delta_j\delta_j$) in the H-H COSY resemble the linear ^1H -NMR spectrum. Interaction partners can be easily identified by cross-peaks ($\delta_i\delta_j$ and $\delta_j\delta_i$) that indicate close proximity.

Through space (dipolar) couplings between upper and lower ring protons and those between the phthalocyanine and the TBA counterion average out in solution so no statement about their interactions can be made by COSY.

The benzene protons of the macrocycle are connected as seen by the characteristic square pattern of diagonal and off-diagonal peaks in the high chemical shift region.

TBA hydrogens also interact with each other as indicated by three rectangles in the upper right of figure 8.

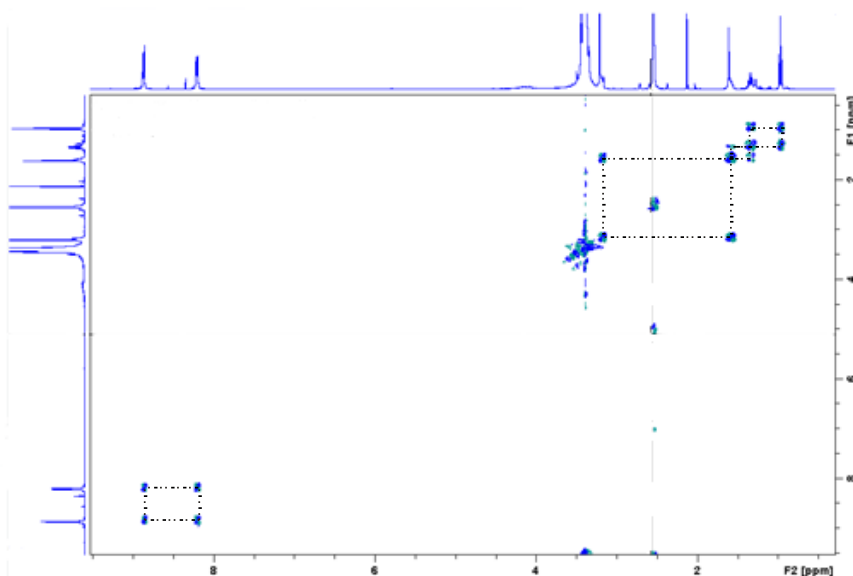


Figure 8: COSY (^1H - ^1H correlation) spectrum of $[\text{LuPc}_2]^- \text{TBA}^+$ in DMSO.

d. HSQC

Heteronuclear single quantum coherence (HSQC) spectra indicate peaks that correspond to directly bound (^1J coupled), hetero-nuclear correlated (^{13}C - ^1H) signals. Because a connection between different nuclei is probed, no diagonal peaks are observable. The recorded 2D plots consist of ^1H broadband decoupled ^{13}C versus the corresponding ^1H spectra. Accordingly, each hydrogen can unambiguously be assigned to the appropriate carbon.

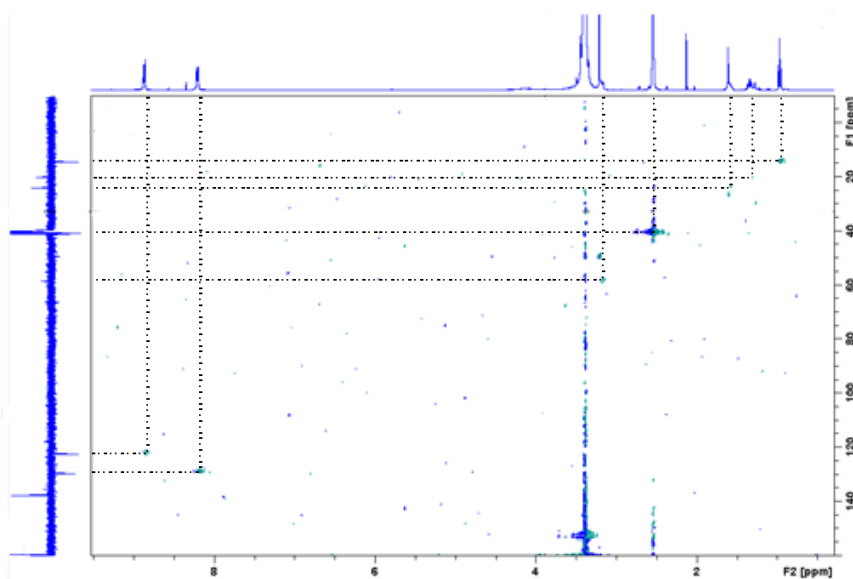


Figure 9: HSQC (single bond ^{13}C - ^1H correlation) spectrum of $[\text{LuPc}_2]^- \text{TBA}^+$ in DMSO.

Table 3. ^{13}C - ^1H correlation table from HSQC measurement of $[\text{LuPc}_2]^- \text{TBA}^+$ in DMSO.

C_n	$\delta^{13}\text{C}$ [ppm]	associated H_n	$\delta^1\text{H}$ [ppm]
C_α	158.96	-	-
C_β	137.15	-	-
C_γ	129.00	H_γ	8.20
C_δ	121.91	H_δ	8.86
C_ϵ	57.89	H_ϵ	3.17
C_μ	23.41	H_μ	1.57
C_ν	19.57	H_ν	1.31
C_ω	13.84	H_ω	0.96
C_{DMSO}	39.5	H_{DMSO}	2.5

e. HMBC

A heteronuclear multi bond correlation (HMBC) spectrum visualizes the same ^{13}C - ^1H shifts as in HSQC but correlates them over three (sometimes also four) bonds.

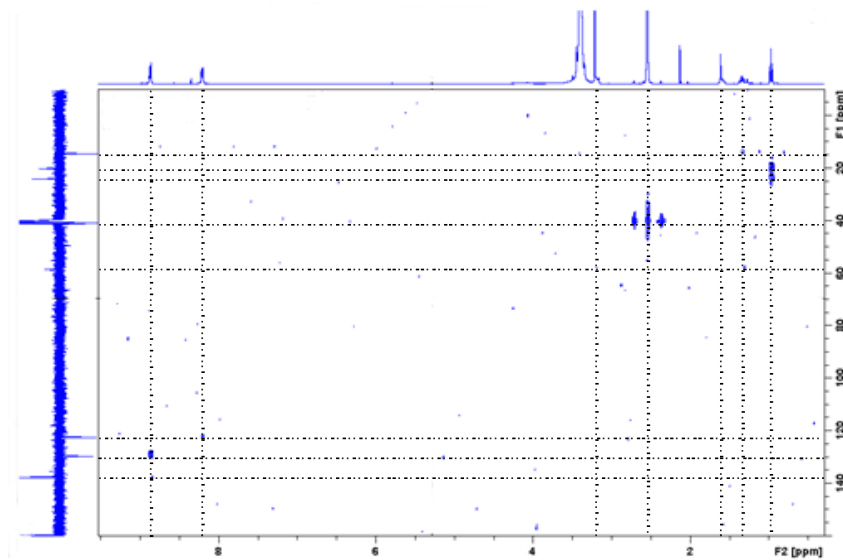


Figure 10: HMBC (multi bond ^{13}C - ^1H correlation) spectrum of $[\text{LuPc}_2]^- \text{TBA}^+$ in DMSO.

The most intensive signals are related to ^1J and ^3J couplings, the less intensive ones correspond to ^2J or ^4J correlations. The trend of highlighted odd numbered couplings was well behaved in the aromatic but for the TBA cation ^2J rather than ^1J couplings are more pronounced.

(c) Electronic spectroscopy

Electronic spectroscopy is a versatile tool in identifying electronic properties resulting from the energetic and steric interplay of the macrocyclic ligands.

a. UV-VIS spectroscopy

UV/VIS spectroscopy is probably the most useful spectroscopy for a quick identification of sandwich dimers. Information about the structure, the substituents, the redox state of the macrocycle and the central metal cation can be obtained from the positions of the UV-VIS bands.

The Q-band position in the VIS generally varies depending on the size of the lanthanoid cation due to modulation of excitonic interactions with an altered distance between the two rings. Substituents in β -peripheral positions (e.g. benzoannulation) modify the FMO energies and thereby change the locations of the individual bands [73].

The considered anionic lutetium phthalocyanine dimer exhibits two peaks in the visible region (Q-bands) where the energetically higher one corresponds to a mostly localized excitation (π - π^* transition between an a_{1u} HOMO and an e_g type LUMO) on one ring referred to as exciton (EX) state while the lower energy optical absorption peak stems from a charge transfer (CT) state between the two rings [78-80]. The shoulder on the high energy side of the exciton band is attributed to a vibronic progression denoted as Q_{vib} .

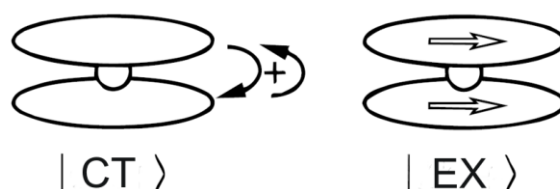


Figure 11: Depiction of dominant excited state configurations that correspond to the main Q-bands. CT denotes the low energy charge transfer Q-band and EX indicates the high energy exciton Q-band [126]. Hollow arrows represent transition dipoles and full arrows correspond to transitions between different rings.

When comparing the VIS spectra of the monomer and dimer, the charge transfer contribution becomes obvious by noting the accompanying spectral changes. The monomer Q-band becomes split up asymmetrically, the widths are unequal and the resulting intensities differ. Such effects cannot be obtained from a simple excitonic interaction alone. Theoretically this is not surprising since exciton theory is only applicable to properly separated dipoles [127, 128]. This condition is not fulfilled in the dimer complex as the separation of the macrocycles is less than their van der Waals radii [106, 129]. The electronic structure of the $[\text{LuPc}_2]^-$ is therefore dominated by orbital overlap and configuration interaction contributions [130]. The inapplicability of exciton theory also prevents predictions of the molecular point group on basis of the relative orientation of transition dipole moments.

Absorption bands in the UV range (Soret or B-bands) are probably also caused by $\pi\text{-}\pi^*$ and CT transitions of the Pc^{2-} benzene components [131], although a clear cut assignment of individual bands in the Soret region is complicated by a relatively high density of possible electronic excitations [132].

The UV-bands following the B-region show resemblance to benzene α - and p-absorption bands.

Experimentally obtained values in benzonitrile (BN) are $Q^{\text{EX}} = 618 \text{ nm}$, $Q^{\text{CT}} = 702 \text{ nm}$, $Q^{\text{vib}} = 565 \text{ nm}$, $B^{\text{EX}} = 333 \text{ nm}$, $B^{\text{CT}} = 411 \text{ nm}$. The different state characters manifest themselves in individual solvent dependences. The CT Q-band is more strongly affected by a change of the solvent than the EX band by virtue of a higher dipole moment. There are no UV/VIS bands that can be directly correlated to the 4f-electron configuration [73].

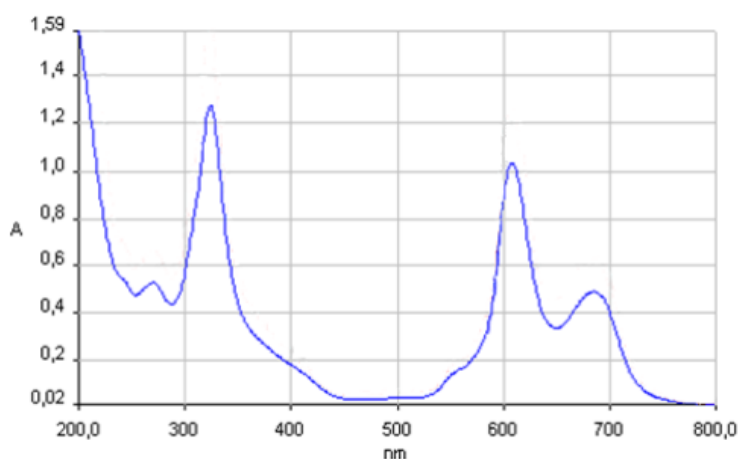


Figure 12: Measured UV-VIS spectrum of $[\text{LuPc}_2]^- \text{TBA}^+$ in CH_3CN .

A recorded UV/VIS/NIR spectrum of the reduced complex up to 3000 nm could not identify previously reported extra bands [132] at 520 nm or around 950 nm and 1060 nm within the instruments sensitivity.

b. Fluorescence spectroscopy

While monomeric phthalocyanines show intensive fluorescence from the Q-band, none could be detected in the corresponding dimeric complexes.

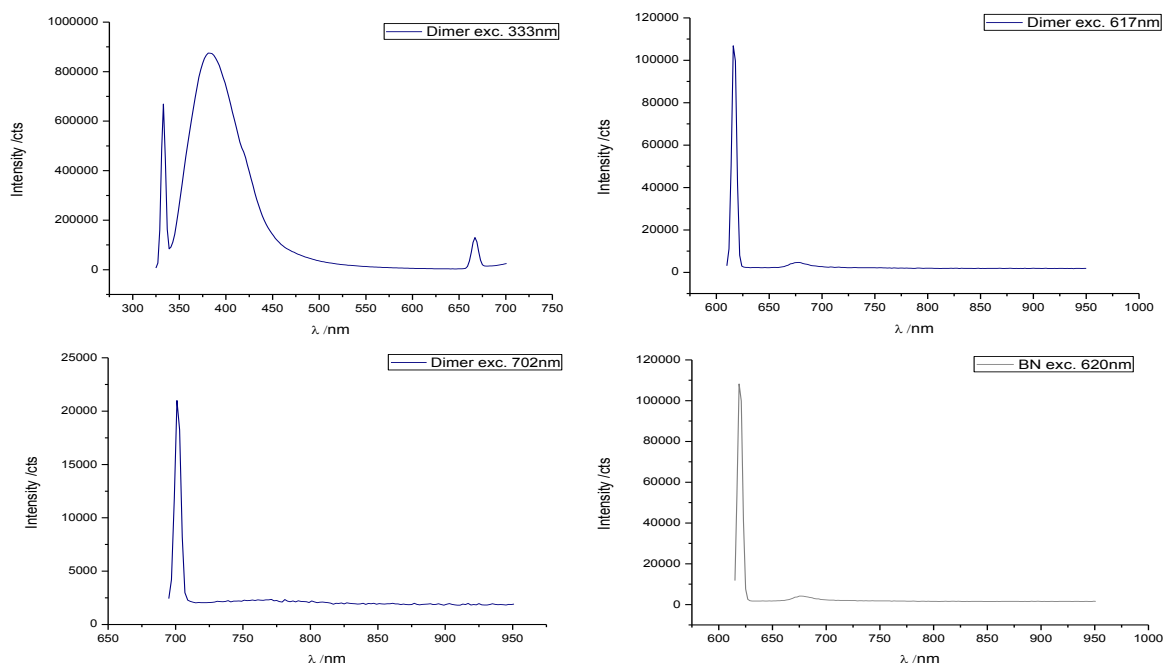


Figure 13: Recorded fluorescence spectra of $[\text{LuPc}_2]^- \text{TBA}^+$ in BN (blue) at different excitation wavelengths of 333 nm (top left), 617 nm (top right) and 702 nm (bottom left). A reference spectrum of pure BN excited at 620 nm is shown in grey (bottom right).

In the first graph the B^{EX} band is excited at 333 nm and the emitted fluorescence is detected corresponding to the second peak around 400 nm. The third peak at 660 nm is associated with the second diffraction order of the excitation beam. The fluorescence curve seems to be broader than the excited Soret absorption band in this diagram but equals it if the appropriate normalization factor ($1/\omega^5$) is taken into account in the wavenumber representation. Fluorescence from a higher excited state is unusual in that it violates Kasha's rule but has been reported for some molecules such as benzene [133]. This finding fits to the similarity of the UV absorption bands to those of benzene.

The second and third figures display the happenings after exciting the Q^{EX} and Q^{CT} states respectively. Both states behave in the same manner and reflect no detectable emission within the experimental sensitivity of 10^{-4} . The recorded spectra display a sharp peak corresponding to the wavelength and width of exciting light flash. The small bump at 660 nm in the Q^{EX} region is related to a solvent Raman mode as can be seen from the solvent response.

The different recorded intensity are related to the excitation energy densities at these wavelengths.

The three most common mechanisms of fluorescence quenching ^[134] are intersystem crossing (heavy-atom effect), electron exchange (Dexter mechanism) and photoinduced electron transfer.

These mechanisms can be excluded based on observations reported in literature and the experimental results obtained by ultrafast spectroscopy. In [LuPc₂]⁻, intersystem crossing is insignificant ^[135] and would lead to phosphorescence which was not detected. Electron exchange is not feasible due to lack of an appropriate acceptor and photoinduced charge transfer to an external acceptor would be easily identified by significant spectral changes. However, none of them are observed on ultrafast timescales.

Broadband pump-probe measurements presented in the last section rather suggest that the excitation relaxes within 150-200 fs to a dark state that moves the population out of the observation window.

(d) Vibrational spectroscopy

The sensitivity of vibrational spectra to symmetry can be used to distinguish between D_{4d} and D_{4h} point groups since in centrosymmetric molecules the mutual exclusion rule dictates that no common absorption bands are allowed in IR and Raman spectra ^[136]. In the case of lutetium bisphthalocyanine weak IR signals or strong Raman ones are of A₁ symmetry while in the opposite instance the vibrations are of E type ^[137]. The D_{4d} symmetry of the complex was confirmed by *Lu et al.* through appearance of several common bands ^[136].

a. Infrared spectroscopy

Due to the high symmetry and the lack of a dipole moment there are only little observable bands in the infrared spectra. The active bands comprise a few fundamental modes associated with the macrocycle. These include ^[132, 136, 138]

- C-H wagging at 730 cm⁻¹
- isoindol breathing coupled to C-H bending at 1110-1115 cm⁻¹
- pyrrole stretching at 1310-1330 cm⁻¹
- isoindol stretching at 1440-1455 cm⁻¹

Marker bands used to differentiate redox states of the phthalocyanine moieties are located at 1310-1330 cm⁻¹. An appearance at 1310-1320 cm⁻¹ is associated with a radical ligand (Pc⁻)

whereas a band at 1330 cm^{-1} denounces the dianionic ring (Pc^{2-}) because a shift to higher wavenumbers is characteristic to an increase in π -electronic density [132, 136, 138].

A solution of the dimer in BN at the same concentration as in the UV/VIS/NIR measurement was recorded in a transmission cell using ZnSe windows and a $200\text{ }\mu\text{m}$ spacer. The following spectra in the range of 700 cm^{-1} to 8000 cm^{-1} were obtained.

The characteristic bands of the dimer complex appear to be of very low intensity and are therefore rather noisy. Especially in the region below 1000 cm^{-1} , large contributions from lamp fluctuations and the non-linear behavior of the detector lead to artefacts during the background subtraction. Despite the bad quality bands are identified at 1112 cm^{-1} , 1330 cm^{-1} and 1381 cm^{-1} . The first two correspond to the double-decker complex and the latter is probably associated with alkyl deformation modes of the TBA cation. The isoindole stretching mode around $1440\text{--}1455\text{ cm}^{-1}$ could not be resolved since the noisy background is dominating this area. The region from $700\text{--}1000\text{ cm}^{-1}$ was not trustworthy enough to be interpreted owing to an oblique baseline and strong noise.

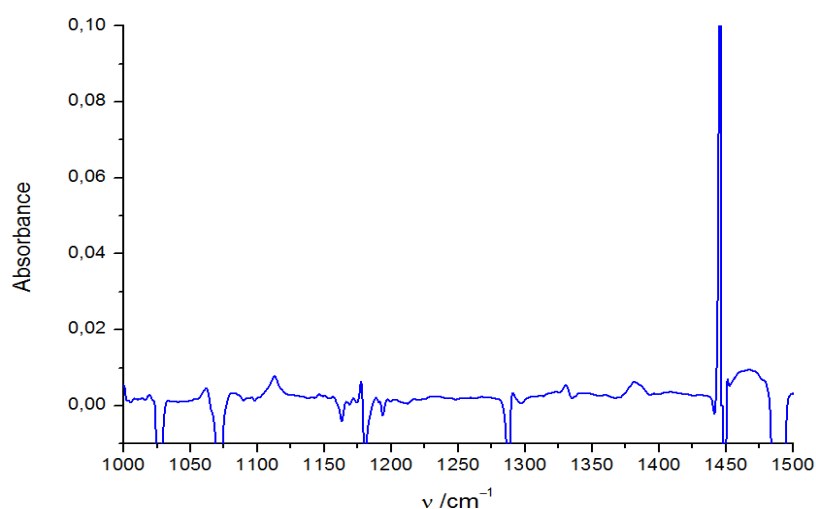


Figure 14: MIR sector from 1000 to 1500 cm^{-1} showing identifiable bands at 1112 cm^{-1} , 1330 cm^{-1} and 1381 cm^{-1} that are associated with the dianionic Pc ligands.

In the region of $3400\text{--}3600\text{ cm}^{-1}$ a single, broad and medium intense band would be expected for N-H stretching modes. However, none such band could be identified.

To investigate whether the complex is protonated at the isoindole nitrogens, a series was tested where defined amounts of water were added. Fig. 13 shows amounts of free water that were added to the sample, yielding characteristic peaks around $3550\text{--}3700\text{ cm}^{-1}$.

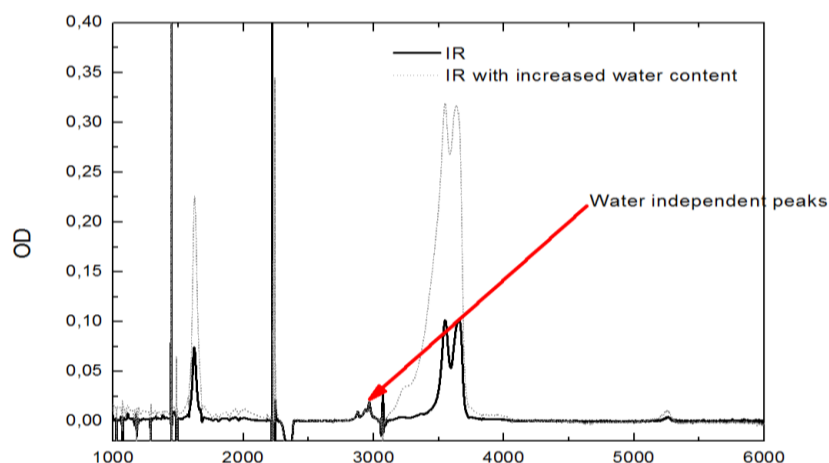


Figure 15: MIR- NIR spectrum of $[\text{LuPc}_2]^- \text{TBA}^+$ in BN (black line) and with increased water content (grey line).

Further increase in water content was not possible because it led to full covering of the considered range by vibrations of water associated H-bonding networks.

Identifiable signals in the region of 2850 cm^{-1} to 3000 cm^{-1} were found to be water independent and are assigned to CH-stretching vibrations of the TBA cation because of their characteristic grouping, the sharp band pattern and relatively weak absorption.



Figure 16: MIR spectrum of water independent bands assigned to the TBA cation.

Differences in intensities between the complex and TBA signals are justified by some excess TBA concentration and a higher dipole moment on account of its alkyl chains being more mobile than the phthalocyanine units.

b. Raman spectroscopy

Bands specific to diphthaloanines are missing [132], therefore only vibrations associated with the macrocycle can be used as indicators [137, 139]:

- isoindole and macrocyclic radial ring vibrations at 400-1000 cm^{-1}
- aromatic C-H vibrations 1000-1300 cm^{-1} in RR
- pyrrol- and aza-stretching vibrations around 1500-1515 cm^{-1}

Off-resonant excitation at 1064 nm yielded strong solvent (BN) bands [140]. Vibrations that are assigned to the phthalocyanine dimer only appeared at high concentrations along with an increased background.

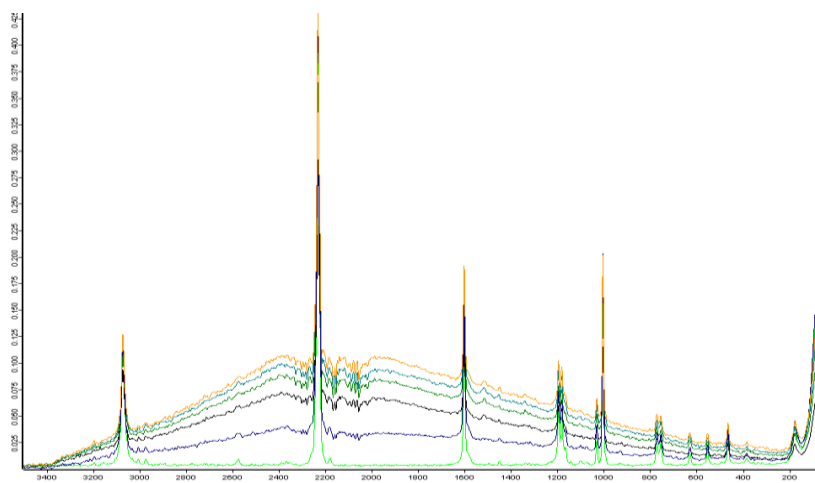


Figure 17: Raman spectra of [LuPc₂]⁻TBA⁺ in BN recorded with increased concentrations to the top and pure BN (light green) as reference.

The most intense band appears at 1500 cm^{-1} . The main component of this vibration stems from C=C pyrrol- and C=N aza-stretchings. The band around 3000 cm^{-1} probably corresponds to its overtone. They are in accordance with those of the dianionic bisphthalocyanine. The region of 1595 -1600 cm^{-1} did not show any evaluable signals that are indicative of the radical species.

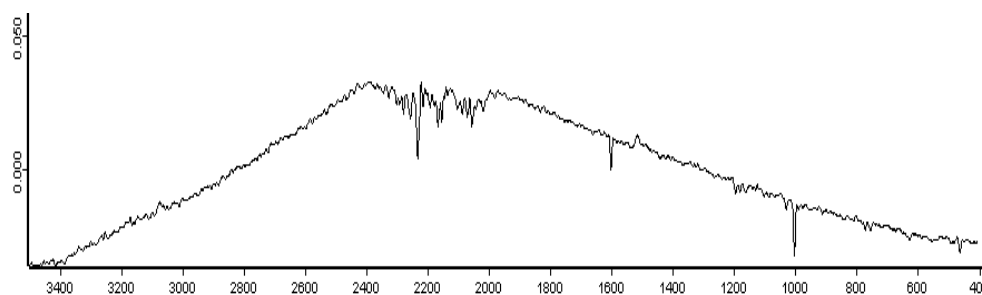


Figure 18: Raman spectra of [LuPc₂]⁻TBA⁺ at high concentrations.

(e) Mass spectrometry

Electrospray ionization mass spectrometry (ESI-MS) provides a sensitive and accurate method for high molecular mass determination to confirm the composition of the synthesized complex.

a. ESI

The high resolution mass spectrum was obtained by ESI in acetonitrile (CH₃CN) / methanol (CH₃OH) at an applied voltage of 4 kV.

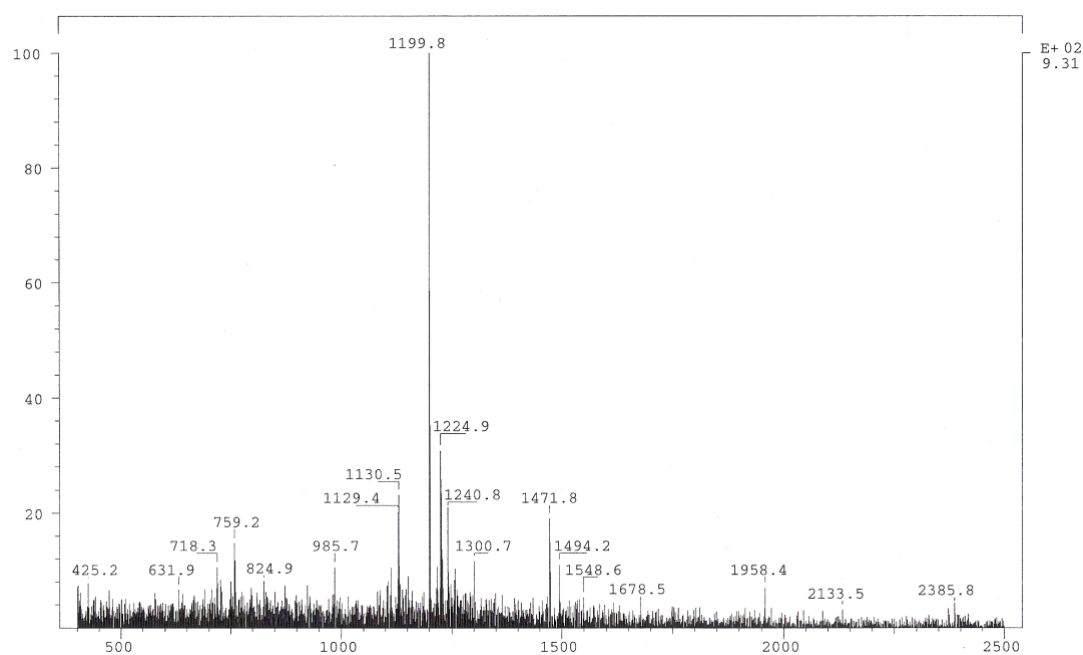


Figure 19: ESI-MS spectrum of [LuPc₂]⁻ TBA⁺ in CH₃CN / CH₃OH.

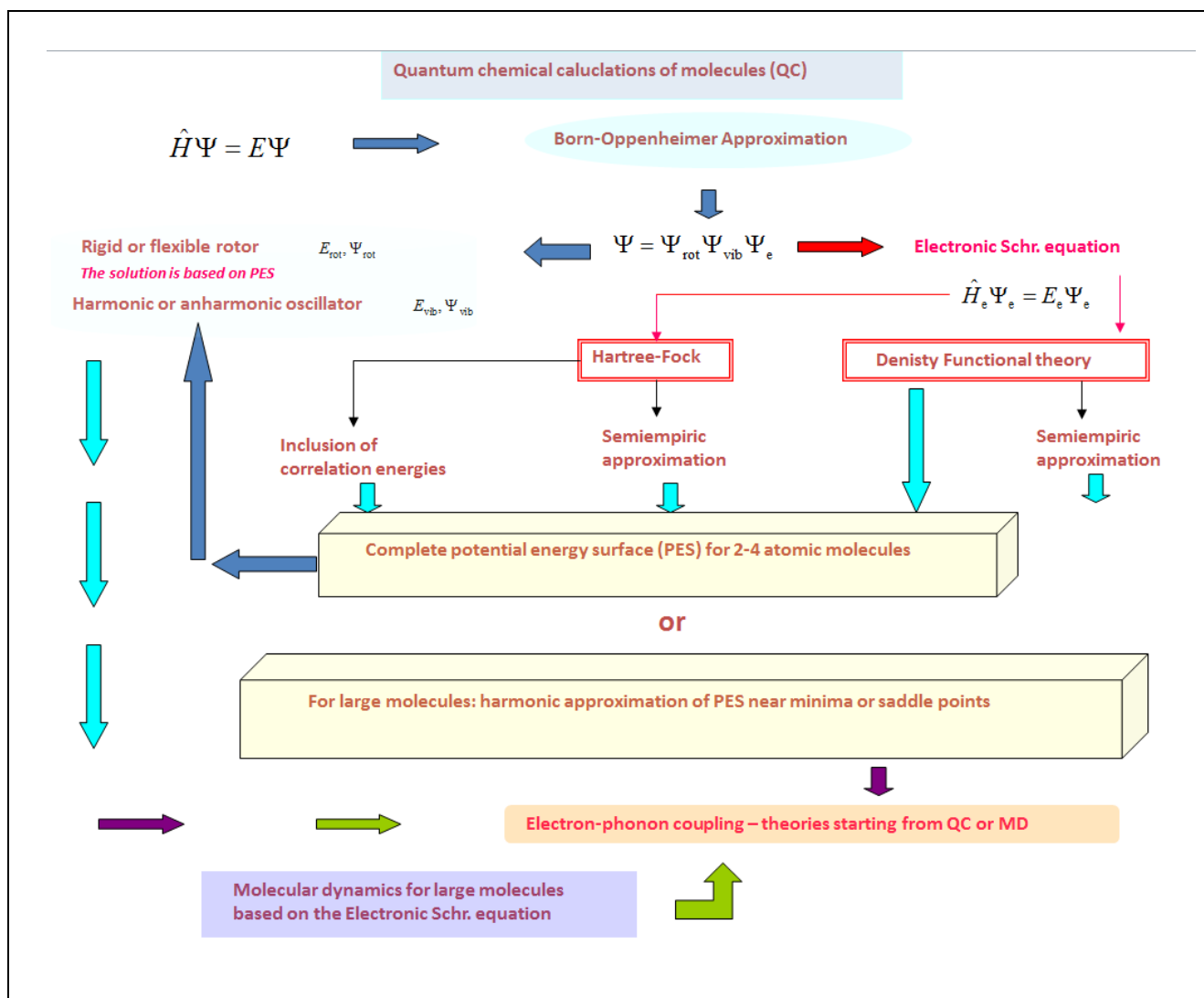
The molecular ion peak of the singly charged complex can be clearly seen as the strongest peak in the decoded ESI spectrum. The measured m/z ratio of 1199.8 is in good agreement with the exact mass of 1199.2 [72].

3. Quantum chemical calculations

The purpose here was to pretest whether it is possible to compute excited states and their vibrational modes to reasonable accuracy to compare it to protruding experimental features. The calculations are employed to confirm a likely participation of conical intersections in the observed ultrafast dynamics, hint to the nature of the involved vibrations and to refine the energy level scheme.

Introduction

The following flow chart depicts the applied general strategy for quantum chemical simulations of molecular properties of the investigated lutetium bisphthalocyanine dimer.



(a) Calculation of the ground state

A first step in calculating the molecular energies and wavefunctions of the ground state involves applying the Born-Oppenheimer approximation to the time-independent Schrödinger equation. It implies to separate energetically different contributions via a product ansatz by setting back the cross-terms between nuclear and electronic parts of the wavefunction and thereby treating them independently [141].

$$\Psi_{total} = \Psi_{electronic} \times \Psi_{nuclear}$$

Initially neglecting the nuclear kinetic energy in the total molecular Hamilton operator leads to an electronic Hamiltonian that depends on fixed nuclear positions through the Coulomb potential. Solving this Schrödinger equation for one particular nuclear configuration (a set of fixed nuclear coordinates) results in the corresponding energy eigenvalue.

$$\hat{H}_e(\vec{r}, \vec{R}) \chi(\vec{r}, \vec{R}) = E_e \chi(\vec{r}, \vec{R})$$

Calculating the electronic energies for infinitesimally changed nuclear geometries then gives the potential energy surface (PES) of the molecule. Reintroduction of the nuclear kinetic energy operator in the PES expression yields components associated with nuclear motions.

$$\left(\hat{T}_N + E_e(\vec{R}) \right) \phi(\vec{R}) = E \phi(\vec{R})$$

A separation of nuclear degrees of freedom into internal (vibrational) and external (rotational and translational) coordinates is achieved by decoupling them using Eckart conditions [142]. These give an orthogonal direct sum decomposition of the 3N dimensional space of nuclear position vectors into a subspace that is invariant under rotation and translation representing internal elements and a remaining external subspace.

$$\vec{R}^{(3N)} = \vec{R}_{internal}^{(3N-6)} \oplus \vec{R}_{external}^{(6)}$$

$$V(\vec{R}_1, \vec{R}_2, \dots, \vec{R}_N) = V(\vec{R}'_1, \vec{R}'_2, \dots, \vec{R}'_N) \equiv V^{internal}$$

$$\text{for } \vec{R}'_i = \vec{R}_i + t \text{ (translation) and } \vec{R}'_i = \vec{R}_i + \frac{\Delta\varphi}{|s|} (s \times \vec{R}_i) \text{ (rotation)}$$

Computing the energy eigenvalue for fixed nuclear configurations is performed by means of density functional theory (DFT) due the large number of atoms constituting the dimer. DFT facilitates the calculation since the electronic density depends only on 3 spatial (plus 1 spin) rather than $3N$ (plus 1 spin) coordinates and because all other molecular properties can be deduced from the density itself [143, 144]. This is since the external potential V_{ext} (nuclear positions) determines the Hamiltonian H , therefore the wavefunction Ψ and the density ρ [145].

$$V_{ext}(\vec{r}) = V_{ext}[\rho(\vec{r})]$$

$$\rho_0 \Rightarrow \{N, Z_A, R_A\} \Rightarrow \hat{H} \Rightarrow \Psi_0 \Rightarrow E_0 \text{ (and other properties)}$$

A DFT approach to calculate molecular energies relies on the Kohn-Sham (KS) equations, an eigenvalue equation formulated in terms of the electronic density [146].

$$\hat{h}^{KS} \varphi_i^{KS} = \varepsilon_i \varphi_i^{KS}$$

The KS energy partitioning operator h^{KS} is made up from similar contributions as the Hartree-Fock (HF) Hamiltonian in that they contain the usual operators [141, 143, 144]:

$$E[\rho] = T_k[\rho] + E_{ext}[\rho] + E_{ee}[\rho]$$

or

$$E[\rho] = T_k[\rho] + E_{ext}[\rho] + E_{Coul}[\rho] + E_{xc}[\rho]$$

which take on the following form:

$$T_k = -\frac{1}{2} \sum \int \varphi_i^{KS*}(\vec{r}) \nabla^2 \varphi_i^{KS}(\vec{r}) d\vec{r} \quad \text{with} \quad \rho(\vec{r}) = \sum |\varphi_i^{KS}(\vec{r})|^2$$

$$E_{ext}[\rho] = -\sum_{m=1}^M Z_m \int \frac{\rho(\vec{r})}{|\vec{r} - \vec{R}_m|} d\vec{r}$$

$$E_{Coul}[\rho] = \frac{1}{2} \iint \frac{\rho(\vec{r}_1)\rho(\vec{r}_2)}{r_{12}} d\vec{r}_1 d\vec{r}_2$$

$$E_{xc}[\rho] = E_x[\rho] + E_c[\rho]$$

T_k – kinetic energy functional, ϕ – independent particle wavefunction

E_{ext} – energy functional of the external potential (electron-nuclear attraction)

E_{ee} – energy functional of electron-electron interactions

E_{Coul} – Coulomb integral (electron-electron repulsion)

E_{XC} – exchange-correlation energy functional

The energy evaluation in this approach is based on a variational minimization of the energy functional with respect to the density according to the second Hohenberg-Kohn theorem [145].

$$V = \frac{\delta E[\rho]}{\delta \rho(r)} \rightarrow \min \quad \text{where} \quad E[\bar{\rho}] \geq E[\rho_0]$$

$$\left(-\frac{1}{2} \bar{\nabla}^2 + V_{Coul}(\rho, \bar{r}) + V_{ext}(\rho, \bar{r}) + V_{XC}(\rho, \bar{r}) \right) \phi_i^{KS}(\bar{r}) = \varepsilon_i \phi_i^{KS}(\bar{r})$$

Because DFT, in contrast to HF, deals with electronic densities rather than point charges it is not clear how the functionals of the kinetic energy and the exchange correlation look like. Therefore it has been most convenient to use the kinetic energy of a set of non-interacting electrons in terms of KS orbitals ϕ^{KS} and put all corrections arising from interaction terms into the E_{xc} functional. Exchange effects (energy lowering caused by a positional interchange of electrons originating from the Pauli principle) are substantially larger than correlation effects (energy lowering due to a decreased Coulomb repulsion caused by the mutual avoidance of two electrons).

The functionals normally used in DFT are integrals of some function of the density and possibly the density gradient [141, 144]:

$$E_{XC}[\rho] = \int f(\rho(\bar{r}), \nabla \rho(\bar{r})) d^3r$$

where methods differ in which function f is used for E_X and which (if any) is used for E_C .

In addition to pure DFT functionals most programs support hybrid methods wherein the exchange functional is a linear combination of the Hartree-Fock exchange and a common DFT exchange-correlation functional. This is possible within the Kohn-Sham formulation because HF theory is regarded as a special case that contains full exchange but no correlation energy. Interpolation between pure HF and pure DFT by the adiabatic theorem allows for creation of a hybrid functional by mixing desired amounts of exchange and correlation from each of the

functionals. Such functionals are usually the most efficient and offer improvement over pure DFT functionals

The size and complexity of the considered molecule requires to simplify matters using a split valence polarized basis set SV(P). Atomic orbitals (AOs) are represented by one-particle Slater type orbitals (STO) which are constructed from a superposition of Gaussian type orbital (GTO) functions ^[141]. A split valence basis set then constructs molecular orbitals (MOs) by assigning one STO to each AO and a larger basis set to the outer AOs. For that only valence orbitals are calculated in a double zeta basis (twofold amount of basis functions) and inner shell orbitals which are not as crucial to the calculation are given by a single STO.

To account for charge distribution distortions by an anisotropic environment (e.g. by the lanthanoid or electronegative atoms like nitrogen) extra basis functions, ones with higher angular momentum quantum numbers, called polarizing functions have been added that mix with and thereby distort the valence orbitals.

The KS equations with specified basis set and exchange-correlation functional are then solved in a self-consistent loop using appropriate numerics for fast iterative solution like steepest and conjugated gradients.

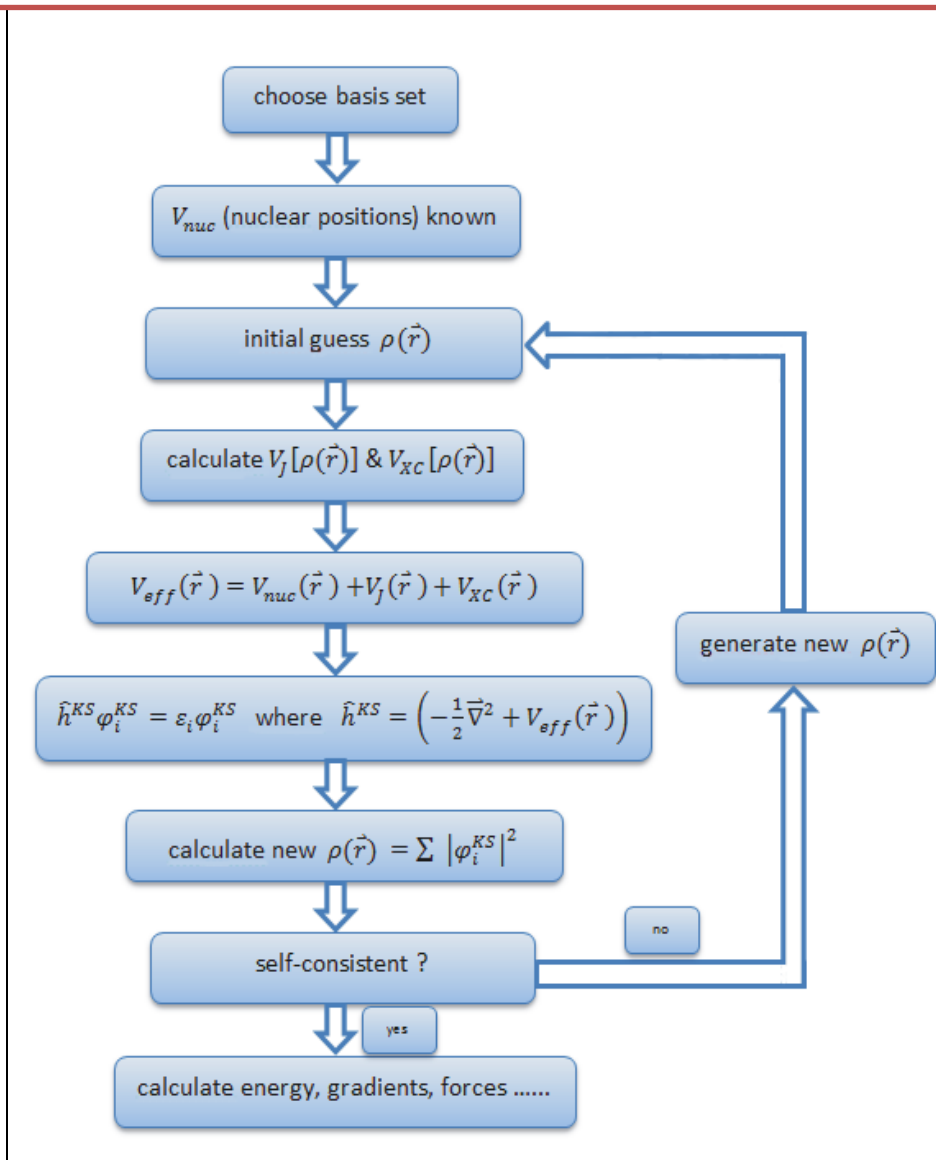
Each converged loop yields one energy eigenvalue to a defined fixed nuclear geometry. Once the electronic Schrödinger equation has been solved for a sufficient number of configurations the energy eigenvalues are interpolated by an analytic function.

The resulting ground state PES is then analysed with respect to its stationary points to define the surface topology ^[147]. Stationary points indicate

1. Minima that correspond to stable or quasi-stable species.
2. Transition states that are equal to saddle points owe minima in all dimensions but one where they possess a maximum.
3. Higher-order saddle points: a minimum in all dimensions but n , where $n > 1$ and a maximum in the other n dimensions.

This analysis is done by calculating the gradients of the energy with respect to all internal coordinates which will be zero at the stationary points.

Self-consistent iterative loop for solving the Kohn-Sham equations



Additionally a torsional potential of the ground state is calculated by restraining geometries to certain values and calculating them using a faster AM-1 / sparkle method parametrized for lutetium complexes [148]. This semiempirical approach is based on the introduction of two spherical Gaussians with variable coefficients for width, intensity and position to the AM-1 technique to more accurately approximate internuclear repulsions.

(b) Normal mode analysis

A normal mode analysis is carried out at stationary points of the ground state PES to characterize nuclear motions (vibrations). For this purpose the harmonic approximation is invoked, meaning that the nuclear Schrödinger equation is solved in the internal molecular frame where only the vibrations enter the equation, so that the PES is approximated as a quadratic function of atomic displacements [149]. Applying the harmonic approximation, the Hamiltonian can be converted into a sum of uncoupled one-dimensional harmonic oscillators. Such an approximation yields enormous simplification because analytical solutions to the quantum mechanical harmonic oscillator are known.

Vibrational frequencies are computed by determining the second derivatives of the energy with respect to the Cartesian nuclear coordinates called Hessian matrix, then transforming the Hessian and the displacements to mass-weighted coordinates and orthogonalizing them by an affine transformation. Diagonalization of the mass-weighted Hessian yields eigenvalues f_i , corresponding to the force constants which are connected to the vibrational frequencies and transformation of the displacements to an orthogonal space yields normal coordinates [149].

$$\hat{\mathbf{H}}_{nuc} = \sum_{i,j} \frac{-\hbar^2}{2m_i} \frac{\partial^2}{\partial x_i^2} + \frac{1}{2} k_{i,j} x_i x_j \quad k_{i,j} = \frac{\partial^2 E(R)}{\partial x_i \partial x_j}$$

$$\hat{\mathbf{H}}_{nuc} = \sum_{i,j} \frac{-\hbar^2}{2} \frac{\partial^2}{\partial \xi_i^2} + \frac{1}{2} \tilde{k}_{i,j} \xi_i \xi_j \quad \xi_i = \sqrt{m_i} x_i \quad \tilde{k}_{i,j} = \frac{k_{i,j}}{\sqrt{m_i m_j}}$$

k_{ij} – harmonic force constants in Cartesian coordinates (second derivatives of the potential energy surface)

ξ – mass weighted Cartesian coordinates

$$\hat{\mathbf{H}}_{nuc} = \sum_{i,j} \frac{-\hbar^2}{2} \frac{\partial^2}{\partial q_i^2} + \frac{1}{2} f q_i^2$$

$$f = \mathbf{T}^t \tilde{\mathbf{k}} \mathbf{T} = \mathbf{T}^t \mathbf{M} \mathbf{k} \mathbf{M} \mathbf{T} \quad \nu_i = \frac{\sqrt{f_i}}{2\pi}$$

$$\mathbf{q} = \mathbf{T}^t \xi = \mathbf{T}^t \mathbf{M} \mathbf{x} \quad M_{i,j} = \delta_{i,j} / \sqrt{m_i}$$

f_i – eigenvalues of the orthogonalized mass weighted Cartesian force constant matrix

q_i – normal modes of vibration

\mathbf{M} – mass coordinate matrix

\mathbf{T} – transformation matrix

Typically the calculated harmonic frequencies are 10% higher than the experimentally observed vibrational frequencies. This discrepancy is rooted in the harmonic approximation.

(c) Calculations of electronically excited states

While the main scope of DFT is a description of the ground state properties of a system at equilibrium an extension in time domain grants access to excited states and non-equilibrium properties [150, 151].

Computation of excited states involves the use of the time-dependent formalism of DFT (TDDFT) that is based on response theory which states that an applied time-dependent potential (radiation field) has the effect of perturbing the electronic ground state density. The change between initial and final configuration is mediated by the response function.

A simulation of optical absorption spectra requires computation of the molecules first excited state that is directly accessed in TDDFT via the linear response term of the perturbed system.

The conceptual and computational foundations for solving the time-dependent Kohn-Sham equations are similar to the stationary case in that one has to determine the effective potential of a fictitious non-interacting system that is the same as that of the interacting one of interest and find the correct density by variation. In TDDFT an exchange-correlation kernel f_{xc} is responsible for corrections to the non-interacting KS linear response [150, 151].

In the time-dependent case calculating the density comprises variation of the action (time integrated expectation value) rather than the energy functional of DFT.

Linear response TDDFT

$$\begin{aligned}
 \text{DFT :} & \quad V(\vec{r}) \Leftrightarrow \rho(\vec{r}) \\
 \text{TDDFT :} & \quad V(\vec{r}, t) \Leftrightarrow \rho(\vec{r}, t) \\
 & \quad V(\vec{r}, t) = V(\vec{r}) + \delta V(\vec{r}, t) \\
 & \quad \delta V(\vec{r}, t) \Leftrightarrow \delta \rho(\vec{r}, t) \text{ in case of } \delta V(\vec{r}, t) \ll V(\vec{r}) \\
 & \quad V(\vec{r}) + \delta V(\vec{r}, t) \Leftrightarrow \rho(\vec{r}) + \delta \rho(\vec{r}, t) \\
 & \quad \downarrow \\
 & \quad \text{TDDFT} = \text{DFT} + \text{linear response}
 \end{aligned}$$

Because excited state wavefunctions are not available from response theory, all excited state properties need to be computed as derivatives of excited state energies [141].

Excited state properties as derivatives of the energy

<i>Response to external</i>	<i>geometrical perturbations</i>	<i>electric fields</i>
$\rho_i^{(1)} = \frac{\partial E_i^{(0+1)}}{\partial V_{ext}}$	$g_{i\alpha} = \frac{\partial E_i^{(0+1)}}{\partial R_\alpha}$	$\mu_i = \frac{\partial E_i^{(0+1)}}{\partial \vec{E}}$
	$H_{ii,\alpha\beta} = \frac{\partial^2 E_i^{(0+1)}}{\partial R_\alpha \partial R_\beta}$	$\alpha_i = \frac{\partial \mu_i}{\partial \vec{E}} = \frac{\partial^2 E_i^{(0+1)}}{\partial \vec{E}^2}$

ρ – perturbed density

g – gradient (force)

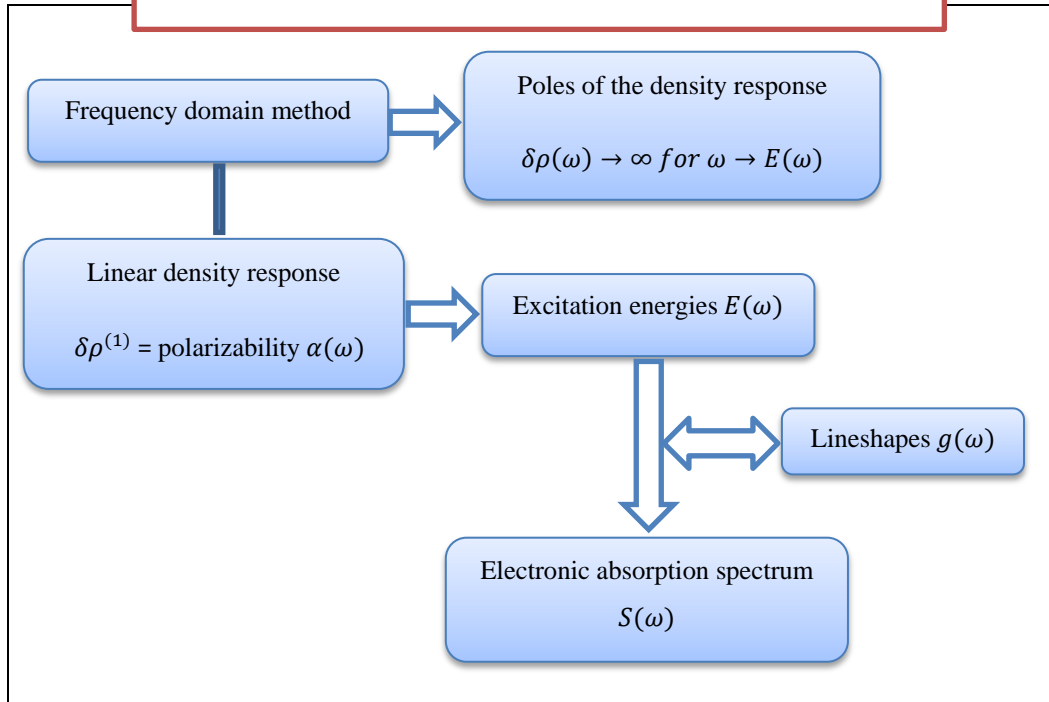
μ – induced dipole moment

\mathbf{H} – Hessian (force constants)

α – induced polarizability

The optical absorption spectrum is calculated in the frequency domain which uses the response function χ to map an external perturbation onto the density and thereby altering it.

Frequency domain technique for optical absorption



The central quantity is the generalized response function in frequency space (Lehmann representation) which is expressed in terms of the KS susceptibility χ^{KS} (independent particle response) and the exchange-correlation kernel f_{xc} (that corrects for the interaction) in a Dyson-like equation. The problem of solving this equation is equivalent to calculating the poles of the generalized response function can be rewritten in form of a Hermitian eigenvalue problem (Casida equation) for frequency independent kernels [150, 151].

The eigenvalues provide excitation energies of the system and the eigenvectors are used to obtain oscillator strengths and to assign the symmetry of each transition.

Frequency domain technique for optical absorption

- step 1: consider external perturbation

$$V_{ext}(\vec{r}, t) = \begin{cases} V_{ext}(\vec{r}) & t < t_0 \\ V_{ext}(\vec{r}) + \delta V_{ext}(\vec{r}) & t > t_0 \end{cases}$$

- step 2: effecting the ground state density

$$\rho(\vec{r}, t) = \rho(\vec{r}) + \delta\rho(\vec{r}, t) + \delta^2\rho(\vec{r}, t) + \dots$$

linear density response

$$\delta\rho(\vec{r}, t) = \iint \chi(\vec{r}, t, \vec{r}', t') \delta V_{ext}(\vec{r}', t') d\vec{r}' dt'$$

response function

$$\chi(\vec{r}, t, \vec{r}', t') = \frac{\delta\rho(\vec{r}, t)}{\delta V_{ext}(\vec{r}', t')}$$

- step 3: evaluate generalized response function in frequency space :

$$\chi(\vec{r}, \vec{r}', \omega) = \chi^{KS}(\vec{r}, \vec{r}', \omega) + \iint \chi^{KS}(\vec{r}, \vec{r}_1, \omega) \left(\frac{1}{r_1 - r_2} + f_{xc}(\vec{r}_1, \vec{r}_2, \omega) \right) \chi(\vec{r}_2, \vec{r}', \omega) dr_1 dr_2$$

↑ yields true excitation energy
↑ calculated from KS eigenstates & values
↑ xc-kernel (generally frequency dependent)

- step 4: for frequency independent kernels finding the poles of χ is equivalent to solving Casida's equation :

$$\sum_q R_{qq'} F_q = \Omega_q^2 F_q$$

↑ matrix operator
↑ ∝ f_i oscillator strength
↑ ∝ E²(ω) excitation energy²

$$R_{qq'} = (\epsilon_{a\sigma} \epsilon_{i\sigma'}) \delta_{qq'} + 2\sqrt{\epsilon_{a\sigma} \epsilon_{i\sigma'}} K_{qq'} \sqrt{\epsilon_{a'\sigma} \epsilon_{i'\sigma'}} = \omega_q^4 \delta_{qq'} + 4\sqrt{\omega_q \omega_{q'}} K_{qq'}$$

↑
interaction (particle-hole matrix element of induced interaction)

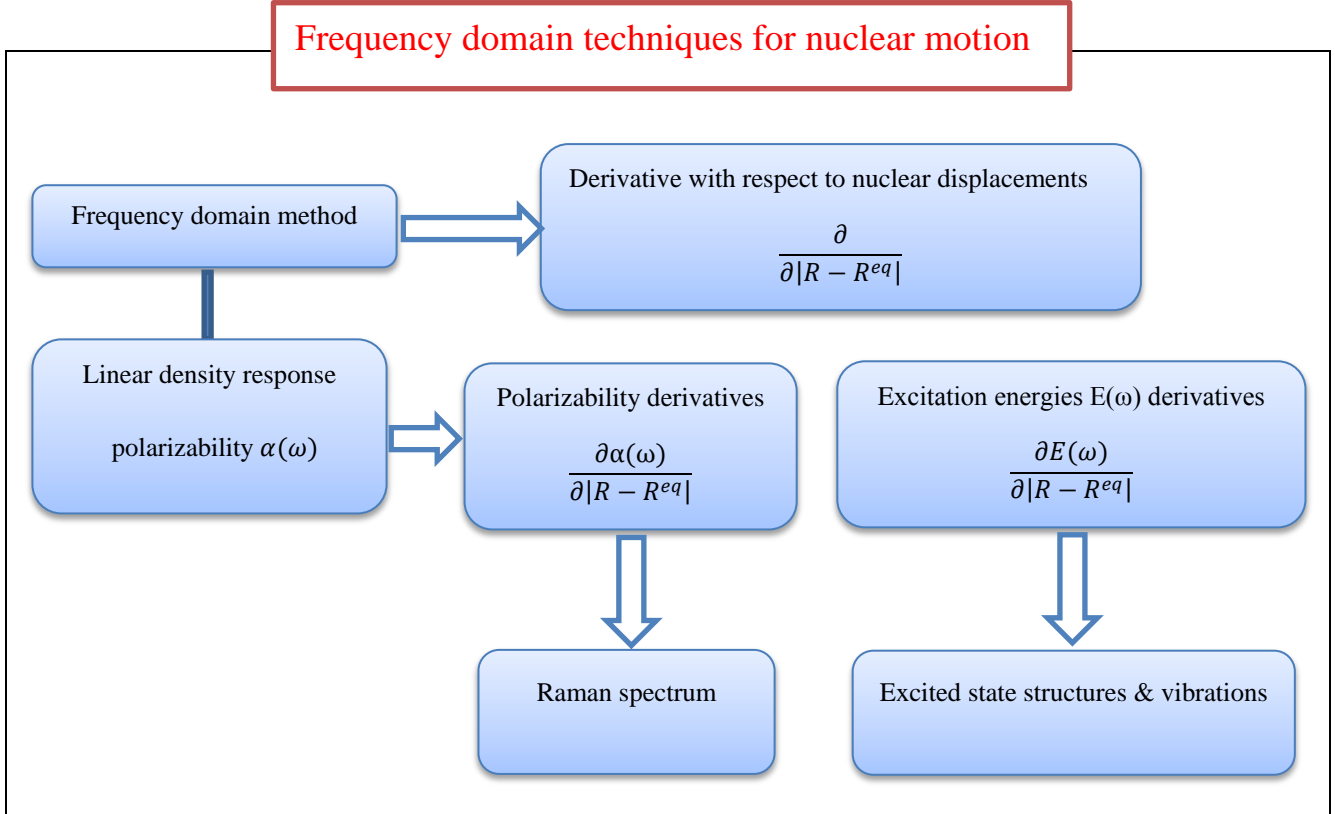
$$K_{qq'} = \iint \phi_{a\sigma}^*(\vec{r}) \phi_{i\sigma}(\vec{r}) \left(\frac{1}{|\vec{r} - \vec{r}'|} + f_{xc\infty}(\vec{r}, \vec{r}', \omega) \right) \phi_{a'\sigma'}(\vec{r}') \phi_{i'\sigma'}^*(\vec{r}') d\vec{r} d\vec{r}'$$

$q = (a, i, \sigma) \dots$ compound index that labels unocc. (a, σ) and occ. (i, σ) orbitals

- step 5: use single pole approximation

$$\Delta E = \epsilon^{KS} + K$$

The frequency technique can also be applied to calculate frequency dependent linear polarizabilities and related properties of nuclear motions within time dependent density functional theory as indicated by the flow chart.



Raman spectra are simulated by numerically differentiating computed polarizabilities with respect to nuclear coordinates.

Spectra are simulated by taking into account symmetry selection rules and computing contributing Franck-Condon-integrals i.e. overlap integrals between vibrational wavefunctions of different electronic states that determining the probability of the transition [141]:

$$\begin{aligned}
 P &= \langle \Psi_i | \hat{\mu}^{total} | \Psi_j \rangle \xrightarrow{\text{Condon approx}} \langle \psi_i^e \psi_i^v \psi_i^s | (\hat{\mu}_e + \hat{\mu}_N) | \psi_j^e \psi_j^v \psi_j^s \rangle \\
 &= \underbrace{\int \psi_i^e \hat{\mu}_e \psi_j^{e*} d\tau_e}_{\text{orbital selection rules}} \cdot \underbrace{\int \psi_i^v \psi_j^{v*} d\tau_N}_{\text{Franck-Condon factors}} \cdot \underbrace{\int \psi_i^s \psi_j^{s*} d\tau_s}_{\text{spin selection rules}} + \underbrace{\int \psi_i^e \psi_j^{e*} d\tau_e}_{\delta_{ij}} \cdot \int \psi_i^v \hat{\mu}_N \psi_j^{v*} d\tau_N \cdot \int \psi_i^s \psi_j^{s*} d\tau_s
 \end{aligned}$$

$$I \propto \langle \psi_i^v | \psi_j^v \rangle^2 = \left| \int \psi_i^v \psi_j^{v*} d\tau_N \right|^2$$

The overlap is optimized iteratively in the Franck-Condon region by expanding the ground state as a linear combination of the excited state and maximizing the coefficients.

Another important quantity that can be computed by TDDFT is the Huang-Rhys factor S_i which relates electronic excitation to structural changes by a linear coupling term [152, 153].

It is the key parameter characterizing the difference in electron-phonon coupling strengths of two states by being a measure of the displacement of the harmonic nuclear potential minimum upon electronic excitation along a vibrational coordinate.

Therefore it naturally occurs that the Huang-Rhys parameter is related to the Franck-Condon factors and is crucial to understand electron-phonon coupling in that it reflects the systems sensitivity to conformational and thermal disorder.

The extent of the shift of the excited state potential curve compared to the ground state parabola governs the relative intensities of the vibronic transitions and gives an idea of the amount of relaxation in the upper state [154].

Values of $S < 0.1$ are interpreted as weak exciton-vibrational coupling.

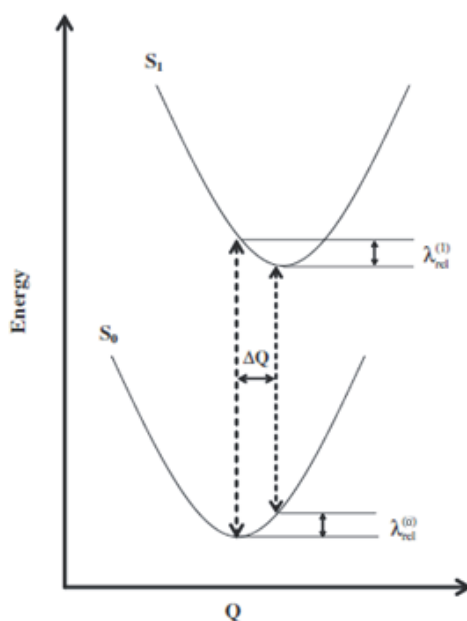


Figure 20: Displaced harmonic potential curves depicting common parameters describing their relation [155]. The shift of the minima along the vibrational coordinate is indicated as ΔQ and the respective reorganisation energy following the excitation is given by λ_i .

The Huang-Rhys factor is indirectly calculated as the resulting shift of the potential curves when computing the Franck-Condon-integrals.

Calculating the difference in the projection of the excited state vibrations onto the ground state normal modes leads to an expression which corresponds to the energy λ_i associated with the displacement ΔQ along that mode. The effect of the considered vibration is described by S_i as reorganizing contribution per total mode energy. The parameters k_i and ω_i denote respective force constants and vibrational frequencies.

$$\lambda_{rel} = \sum_i \lambda_i = \hbar \omega_i S_i$$

$$\lambda_i = \frac{k_i}{2} \Delta Q_i^2 \quad \text{and} \quad S_i = \frac{\lambda_i}{\hbar \omega_i}$$

(d) Calculation details

All calculations have been performed with the programs TURBOMOLE [156] and MOPAC [157].

The following functionals have been used in calculating properties of the lutetium bisphthalocyanine dimer:

PBE: Perdew-Becke-Ernzerhof [158]. This GGA-functional is given by [159]

$$E_x^{\text{PBE}} = \frac{bx^2}{1+ax^2}$$

$$a = 0.00449; \quad b = 0.00336; \quad x = \frac{|\nabla\rho|}{\rho^{4/3}}$$

It was designed to reproduce exchange features only and is usually combined with the Perdew-Wang (PW) correlation functional.

B3LYP: Becke "Three Parameter" Lee-Yang-Parr [160]. This functional has the form

$$E_{xc}^{\text{B3LYP}} = a_0 E_x^{\text{HF}} + (1-a_0) E_x^{\text{LDA}} + a_x E_x^{\text{B88}} + (1-a_c) E_c^{\text{VWN80}} + a_c E_c^{\text{LYP88}}$$

$$a_0 = 0.2; \quad a_x = 0.72; \quad a_c = 0.81$$

The lower case x refers to determination of electron exchange while the lower case c refers to the determination of electron correlation. Approximations that are part of this functional are

Hartree-Fock (HF) – pure nonlocal exchange, Local density approximation (LDA) - pure local DFT exchange, Becke-1988 (B88) – gradient corrected local exchange, Vosko-Wilks-Nusair 1980 (VWN80) – local correlation and Lee-Yang-Parr 1988 (LYP88) – non-local correlation.

BHLYP: Becke “ Half and Half ” Lee-Yang-Parr [161]. This functional reads

$$E_{xc}^{\text{BHLYP}} = a_0 E_x^{\text{HF}} + (1 - a_0) E_x^{\text{LDA}} + a_x E_x^{\text{B88}} + a_c E_c^{\text{LYP88}}$$

$$a_0 = 0.5; a_x = 0.5; a_c = 1$$

It is used to reduce the problems associated with the wrong asymptotic behavior of the KS potentials since it includes 50% of exact exchange.

All calculations have been performed with a split valence polarized basis set, SV(P).

The applied valence basis functions of the individual atoms comprise 2s for hydrogen, 3s 2p 1d for carbon, 3s 2p 1d for nitrogen and 10s 8p 5d 4f 1g for lutetium on top of the corresponding cores [162].

(e) Results

Among the three functionals tested within the same basis set the overall best results were obtained when using BHLYP. This is attributed to the varying extent of non-local exchange contributions in the different functionals as discussed at the end of the results section.

For this reason only results perceived within BHLYP are presented.

The reduced lanthanoid bisphthalocyanine is modeled as a double-decker consisting of a central trivalent lanthanoid ion sandwiched in between two parallel π -conjugated macrocycles.

The filled 4-f orbitals and a formal charge of 2– on each ligand set off a closed shell configuration of the overall complex. Figure 21 shows the corresponding electronic ground state equilibrium structure of the lutetium bisphthalocyanine dimer.

The strong electrostatic attraction of the coordinating isoindole nitrogens with the rare earth cation leads to concave distortions of the peripheral benzene groups giving rise to an off-planarity angle of 6.6°. The attraction is balanced by counteracting orbital repulsions at the equilibrium interring distance of 3.144 Å and leads to 45° staggering of the macrocycles with a quadratic antiprism in D_{4d} ligand field as coordination polyhedron.

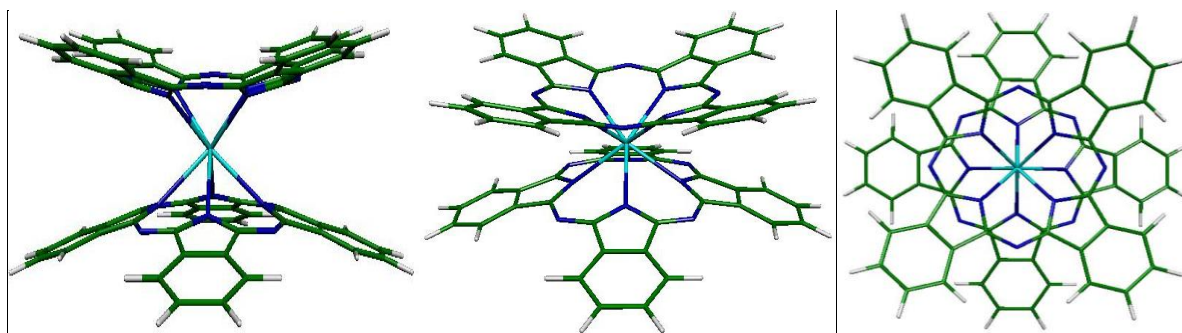


Figure 21: Optimal BHLYP/SV(P) geometry for electronic ground state.

The computation reproduces the main features of the crystal structure properly as depicted by the resulting geometrical parameters of the ground state in table 4.

Table 4. BHLYP / SV(P). structural parameters for ground state equilibrium geometry of [LuPc₂]⁻

<i>atoms</i>	<i>distance</i> [Å]	<i>atoms</i>	<i>angle</i> [°]	<i>atoms</i>	<i>dihedral angle</i> [°]
N _{iso} -N' _{iso}	3.144	N _{iso} -Lu-N' _{iso}	80.9	N _{iso} - Lu- N' _{iso} -C' _α	114..7
N _{iso} -N'' _{iso}	3.144	N _{iso} -Lu-N'' _{iso}	80.9	N _{iso} - Lu- N'' _{iso} -C' _α	-114.7
N _{iso} -N _{iso'''}	3.985	C _α -N _{iso} -Lu	124.2	Lu- N _{iso} -C _α -N _{aza}	-29.7
Lu- N _{iso}	2.421	C _α -N _{iso} -C _{α'}	108.4	Lu-N _{iso} -C _α -C _β	155.4
N _{iso} -C _α	1.354	C _α -N _{aza} -C _α	124.4	N _{iso} -C _α -C _β -C _γ	179.3
C _α -N _{aza}	1.315	N _{iso} -C _α -C _β	109.7	N _{iso} -C _α -C _β -C _{β'}	3.0
C _α -C _β	1.458	C _α -C _β -C _{β'}	106.0	C _α -N _{iso} -C _{α'} -N _{aza}	170.0
C _β -C _{β'}	1.394	C _γ -C _β -C _{β'}	121.2	C _α -C _β -C _γ -C _δ	-178.2
C _β -C _γ	1.389	C _β -C _γ -C _δ	117.7	C _β -C _γ -C _δ -C _{δ'}	0.8
C _γ -C _δ	1.386	C _γ -C _δ -C _{δ'}	121.1	H _γ -C _γ -C _δ -H _δ	0.4
C _δ -C _{δ'}	1.403	C _γ -C _δ -C _{δ'}	121.1	H _δ -C _δ -C _{δ'} -H _{δ'}	0.0
C _γ -H _γ	1.085	H _γ -C _γ - C _δ	121.8	C _α -N _{aza} -C _α -N _{iso}	6.6
C _δ -H _δ	1.086	H _δ -C _δ -C _{δ'}	119.2	C _α -N _{aza} -C _α -C _β	167.8

An illustrating graph of the listed ground state equilibrium parameters is given in figure 22 to facilitate comparisons.

The calculated ground state interplanar distance deviates by 2% from the crystal structure. The metal to isoindole nitrogen and C_α-aza-nitrogen bonds exhibit the largest deviations on the order

Table 5. Selected structural parameters for first excited state equilibrium geometry calculated with TD-BHLYP / SV(P).

<i>atoms</i>	<i>distance</i> [Å]	<i>atoms</i>	<i>angle</i> [°]	<i>atoms</i>	<i>dihedral angle</i> [°]
N _{iso} -N' _{iso}	3.077	N _{iso} -Lu-N' _{iso}	79.9	N _{iso} -Lu-N' _{iso} -C' _α	113.3
N _{iso} -N'' _{iso}	3.084	N _{iso} -Lu-N'' _{iso}	80.1	N _{iso} -Lu-N'' _{iso} -C' _α	-113.6
N _{iso} -N _{iso} '''	3.974	C _α -N _{iso} -Lu	123.4	Lu-N _{iso} -C _α -N _{aza}	31.4
Lu-N _{iso}	2.396	C _α -N _{iso} -C _α '	108.9	Lu-N _{iso} -C _α -C _β	153.2
N _{iso} -C _α	1.355	C _α -N _{aza} -C _α	124.1	N _{iso} -C _α -C _β -C _γ	179.3
C _α -N _{aza}	1.318	N _{iso} -C _α -C _β	109.4	N _{iso} -C _α -C _β -C _β '	3.0
C _α -C _β	1.461	C _α -C _β -C _β '	106.1	C _α -N _{iso} -C _α '-N _{aza}	171.6
C _β -C _β	1.396	C _γ -C _β -C _β '	121.2	C _α -C _β -C _γ -C _δ	178.8

The second excited state (S_2) corresponds to the state whose transition energy is closest to that of the CT Q-band. Its equilibrium geometry is less strongly shifted along the metal-isoindole bond than the ground and third excited states.

Table 6. Selected structural parameters for relaxed second excited state equilibrium geometry calculated with TD-BHLYP / SV(P).

<i>atoms</i>	<i>distance</i> [Å]	<i>atoms</i>	<i>angle</i> [°]	<i>atoms</i>	<i>dihedral angle</i> [°]
N _{iso} -N' _{iso}	3.115	N _{iso} -Lu-N' _{iso}	80.8	N _{iso} -Lu-N' _{iso} -C' _α	114.7
N _{iso} -N'' _{iso}	3.126	N _{iso} -Lu-N'' _{iso}	80.4	N _{iso} -Lu-N'' _{iso} -C' _α	-115.2
N _{iso} -N _{iso} '''	3.982	C _α -N _{iso} -Lu	124.2	Lu-N _{iso} -C _α -N _{aza}	29.4
Lu-N _{iso}	2.412	C _α -N _{iso} -C _α '	108.4	Lu-N _{iso} -C _α -C _β	155.7
N _{iso} -C _α	1.356	C _α -N _{aza} -C _α	124.1	N _{iso} -C _α -C _β -C _γ	179.8
C _α -N _{aza}	1.317	N _{iso} -C _α -C _β	109.7	N _{iso} -C _α -C _β -C _β '	2.8
C _α -C _β	1.459	C _α -C _β -C _β '	106.0	C _α -N _{iso} -C _α '-N _{aza}	170.2
C _β -C _β	1.395	C _γ -C _β -C _β '	121.2	C _α -C _β -C _γ -C _δ	177.9

The third excited state (S_3) is associated with the transition energy closest to the EX Q-band. Its equilibrium geometry along the metal-isoindole bond is further shifted than S_1 and S_2 but on the same order as the ground state.

Table 7. Selected structural parameters for relaxed third excited state equilibrium geometry calculated with TD-BHLYP / SV(P).

<i>atoms</i>	<i>distance</i> [Å]	<i>atoms</i>	<i>angle</i> [°]	<i>atoms</i>	<i>dihedral angle</i> [°]
$N_{iso}-N'_{iso}$	3.147	$N_{iso}-Lu-N'_{iso}$	81.0	$N_{iso}-Lu-N'_{iso}-C'_{\alpha}$	114.5
$N_{iso}-N''_{iso}$	3.158	$N_{iso}-Lu-N''_{iso}$	81.3	$N_{iso}-Lu-N''_{iso}-C'_{\alpha}$	-114.9
$N_{iso}-N_{iso}'''$	3.984	$C_{\alpha}-N_{iso}-Lu$	124.2	$Lu-N_{iso}-C_{\alpha}-N_{aza}$	29.4
$Lu-N_{iso}$	2.423	$C_{\alpha}-N_{iso}-C_{\alpha}'$	108.3	$Lu-N_{iso}-C_{\alpha}-C_{\beta}$	155.2
$N_{iso}-C_{\alpha}$	1.356	$C_{\alpha}-N_{aza}-C_{\alpha}$	124.1	$N_{iso}-C_{\alpha}-C_{\beta}-C_{\gamma}$	179.0
$C_{\alpha}-N_{aza}$	1.317	$N_{iso}-C_{\alpha}-C_{\beta}$	109.7	$N_{iso}-C_{\alpha}-C_{\beta}-C_{\beta}'$	3.2
$C_{\alpha}-C_{\beta}$	1.457	$C_{\alpha}-C_{\beta}-C_{\beta}'$	106.0	$C_{\alpha}-N_{iso}-C_{\alpha}'-N_{aza}$	170.2
$C_{\beta}-C_{\beta}$	1.396	$C_{\gamma}-C_{\beta}-C_{\beta}'$	121.2	$C_{\alpha}-C_{\beta}-C_{\gamma}-C_{\delta}$	178.4

Interestingly this implies that S_2 and S_1 , S_3 are oppositely shifted around the ground state equilibrium with respect to the same nuclear coordinate which is in agreement with experimental findings [82]. S_1 and S_3 are shifted in the same direction but with different magnitude.

The torsional potential curve of the ground state exhibits only one global minimum at 45° and a corresponding rotation barrier of 75.6 kJ/mol when calculated with semi-empirical AM-1 / sparkle method for restrained geometries. Similar energetic results for the torsional extrema were obtained with BHLYP / SV(P) validating the AM-1 / sparkle accuracy. Such a high barrier forbids any free rotation of the ligands at room temperature and the structure is therefore assumed to be non-fluctuational.

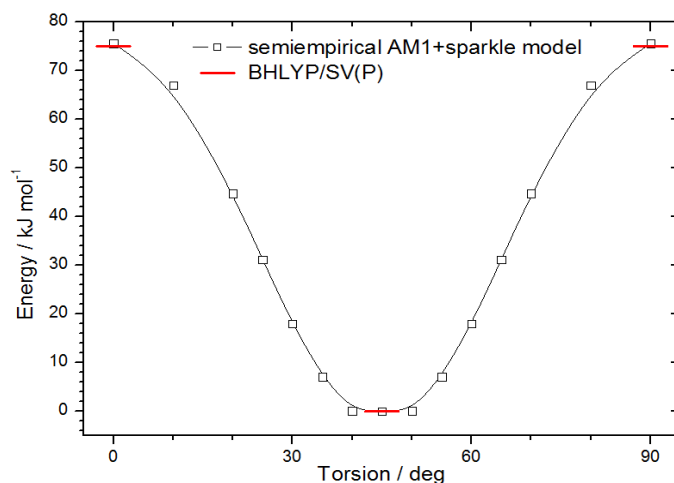


Figure 23: Interpolated torsional potential curve of the electronic ground state at constrained geometries using AM-1 /sparkle (squares) and superimposed BHLYP values (red lines).

Results of the ground state normal mode analysis are presented in figures 24 and 25. Lutetium bisphthalocyanine's ground state vibrations are summarized in spectral form.

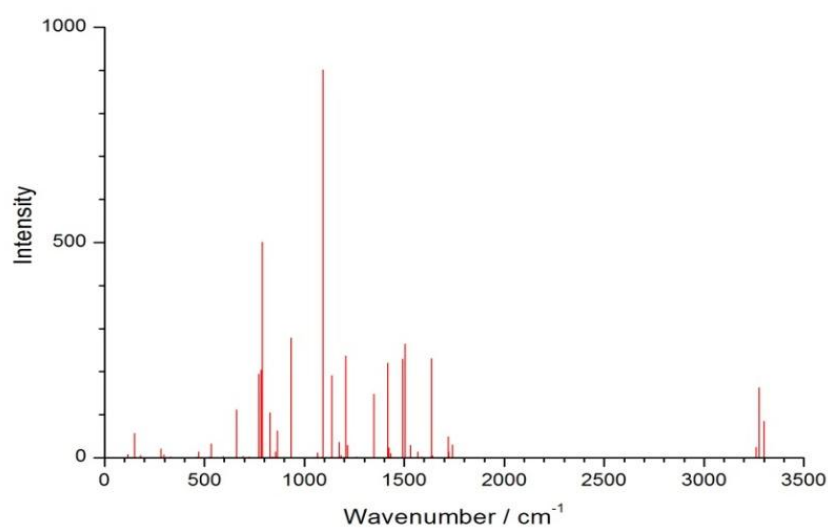


Figure 24: Calculated BHLYP/SV(P) ground state normal mode stick spectrum.

Pronounced Raman normal modes of the electronic ground state are used in assigning vibronic transitions and refining energy level diagrams and hence are given in more detail by table 8 and successive visualizations in the next figure.

Table 8. TD-BHLYP/SV(P) calculated vibrational electronic ground-state frequencies (cm^{-1}) and Huang-Rhys factors S_i with respect to corresponding excited state i (only vibrational modes with S_i larger than 0.01 are shown).

ν (cm^{-1})	S_1	S_2	S_3	<i>Raman activity</i>
6.13	0.0059	0.0460	0.0503	Yes
47.58	45.607	0.0471	0.0018	Yes
140.31	2.2266	0.5604	0.0186	Yes
217.05	0.0057	0.0142	0.1830	Yes
294.98	2.1926	0.0096	0.0022	Yes
473.99	4.0482	0.0061	0.0003	Yes
605.86	0.1052	0.0018	0.0114	Yes
725.8	0.6904	0.0697	0.0490	Yes
791.2	40.859	0.0020	0.0028	Yes
845.27	24.893	0.0032	0.0234	Yes
854.21	0.0000	0.0134	0.0014	Yes
872.37	3.0517	0.0059	0.0583	Yes
943.37	0.0048	0.0197	0.0039	Yes
1028.58	0.0254	0.0169	0.0142	Yes
1066.15	0.1125	0.0106	0.0000	Yes
1147.70	0.0145	0.0279	0.0322	Yes
1234.59	0.0067	0.0162	0.0186	Yes
1279.29	0.0207	0.0339	0.0357	Yes
1371.69	0.0948	0.1727	0.1943	Yes
1425.02	0.0325	0.0285	0.0130	Yes
1573.30	0.1749	0.3099	0.3465	Yes
1742.61	0.0234	0.0026	0.0034	Yes
3260.39	0.0092	0.0175	0.0197	Yes
3299.41	0.1361	0.3452	0.4049	Yes
3302.36	0.1470	0.0251	0.0100	Yes

The strongly exaggerated Huang-Rhys factors with respect to S_1 are presumably caused by an incorrect calculation. The error might arise from a large shift of the equilibrium geometry of that state.

A depiction of the strongest listed Raman modes to the excited states S_1 - S_3 is shown below.

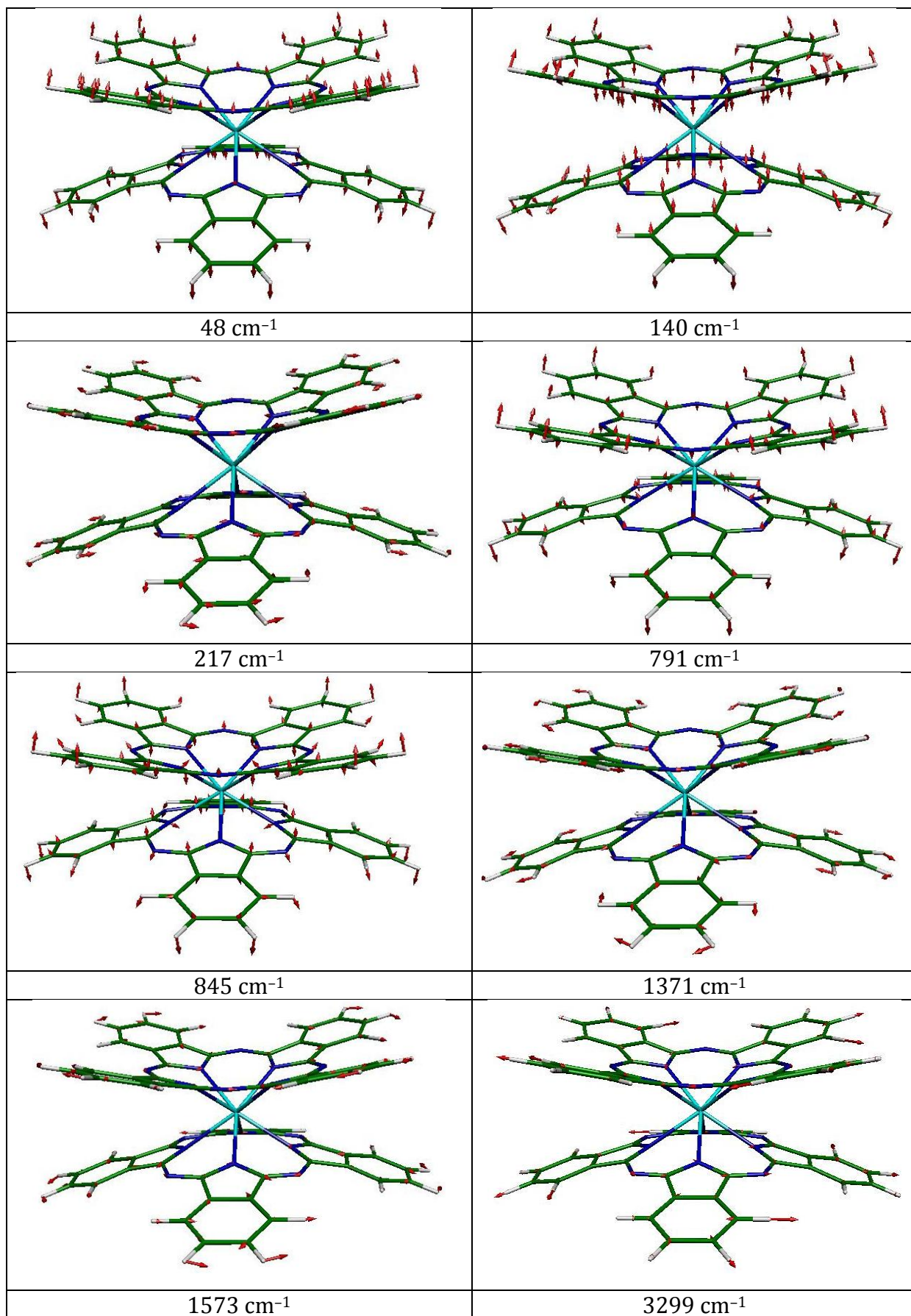


Figure 25: A visualisation of the BHLYP/SV(P) modes dominating the vibronic structure of the optical absorption spectrum.

The 47 cm⁻¹ mode exhibits characteristics of a symmetric out-of-plane ring bending vibration. 140 cm⁻¹ resembles a symmetric interring stretching. 217 cm⁻¹ is an in-plane rocking of the isoindole units. 791 cm⁻¹ corresponds to a symmetric benzene and C_α-pyrrole wagging. 845 cm⁻¹ shows an out-of-phase motion of the benzene and C_α-pyrrole wagging contributions. 1371 cm⁻¹ displays an asymmetric C_α-pyrrole stretch and a benzene rocking. The 1573 cm⁻¹ vibration indicates an in-plane benzene deformation of the ring periphery and 3299 cm⁻¹ demonstrates large asymmetric H_γ- and smaller H_δ stretches.

The most dominant vertical excitations between ground and electronically excited states are summarized in the next table.

Table 9: Vertical excitation and vertical de-excitation energies with respect the ground state (in nm) obtained from TD-B3LYP/SV(P) and TD-BHLYP/SV(P) calculations from their respective optimal B3LYP and BHLYP/SV(P) geometries. The values in parentheses represent the corresponding oscillator strengths.

PBE: S₀ (f)	B3LYP: S₀ (f)	BHLYP: S₀ (f)
1016 (0.0000)	895 (0.0000)	856 (0.0000)
858 (0.0320)	733 (0.0818)	631 (0.4529)
607 (0.7360)	565 (1.0291)	536 (1.0400)
580 (0.0068)	407 (0.0000)	480 (0.0000)
520 (0.00010)	395 (0.14322)	319 (0.2710)

Unfortunately poor agreement with experimentally recorded absorption spectra is achieved therein concerning energetic locations and transition strengths of spectral bands.

When using B3LYP the exciton state was obtained in good accordance with experiment (606 nm) while the CT band was failed significantly by nearly 200 nm. Moreover there is a predicted transition in the visible region rather than a Soret band in the UV.

In BHLYP the CT Q-band is more closely approximated just as the Soret B-band but the calculation deviates in the exciton region.

Another striking problem emerging in all TDDFT calculations is a way to low intensity of CT bands since configuration interaction effects are neglected. Once again BHLYP yields a more realistic picture of the actual intensity ratios than B3LYP but still differs by a factor of 5.

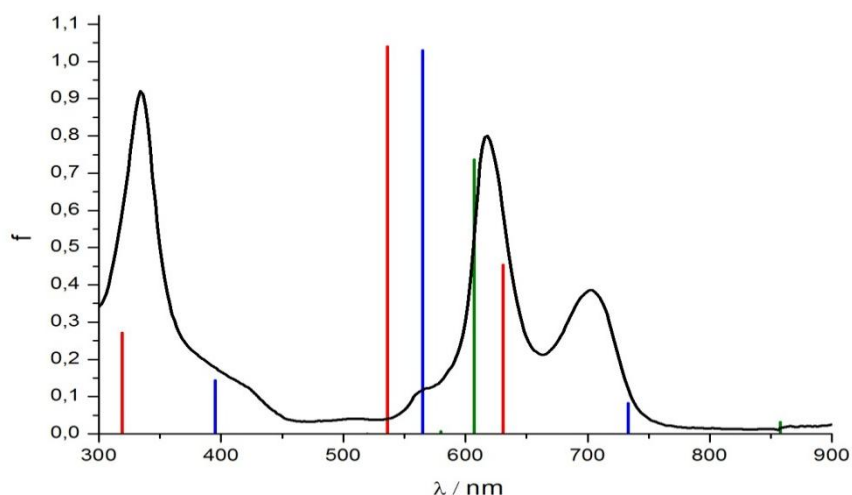


Figure 26: Experimental absorption spectrum in BN (black line) and simulated gas phase TD-PBE/SV(P), TD-B3LYP/SV(P) and TD-BHLYP/SV(P) stick spectra. PBE results are given in green, B3LYP in blue and BHLYP in red.

Considering linear response nature of TDDFT (validity within small deviations from equilibrium) and that the accuracy of the obtained results is not within a 10 % threshold needed to safely compare theoretical predictions and experiment no further higher excited states shall be discussed.

Calculated KS orbitals of the dimer in its electronic ground state that give rise to the calculated optical transitions and their respective energies are shown below.

Although KS orbitals should not be interpreted as conventional MOs there is striking similarity to those calculated by Ishikawa and Rousseau.

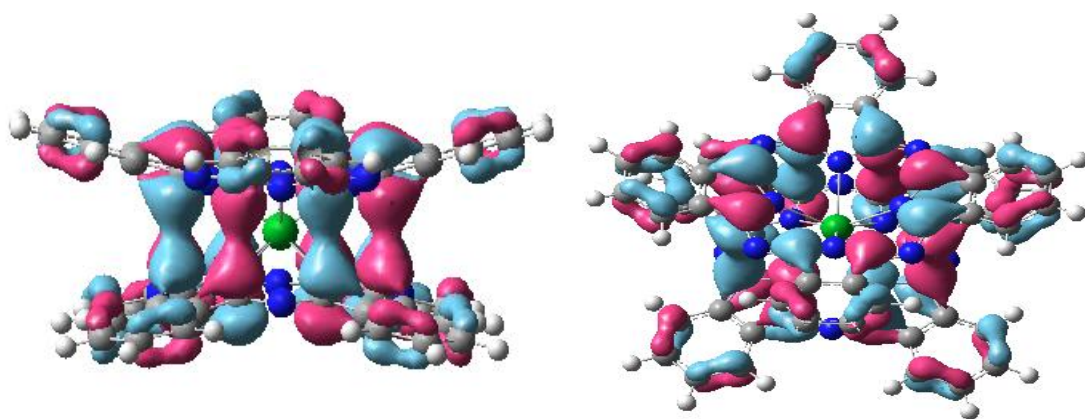
HOMO-1 is a bonding π -orbital with its density mostly located between carbons closest to their individual ring centres (C_α).

The HOMO is an anti-bonding π -orbital predominantly centred on C_α -carbons of the macrocycles.

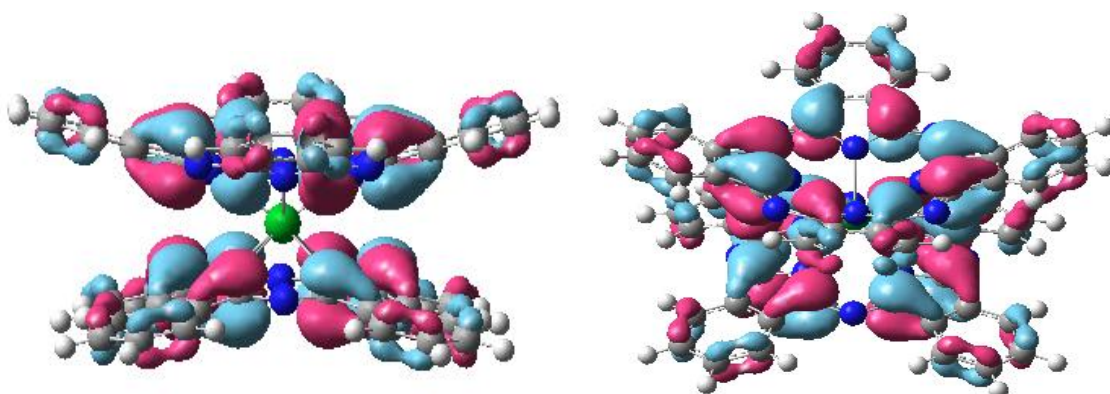
In the LUMO of the molecule the probability density is essentially aligned along two opposite benzopyrrole units of the same macrocycle with large contributions between C_α/C_β -carbons on different rings as well as from bridging aza- and isoindole nitrogens.

LUMO+1 corresponds to a rotated version of LUMO with antisymmetric contributions from bridging aza- and isoindole nitrogens on different rings.

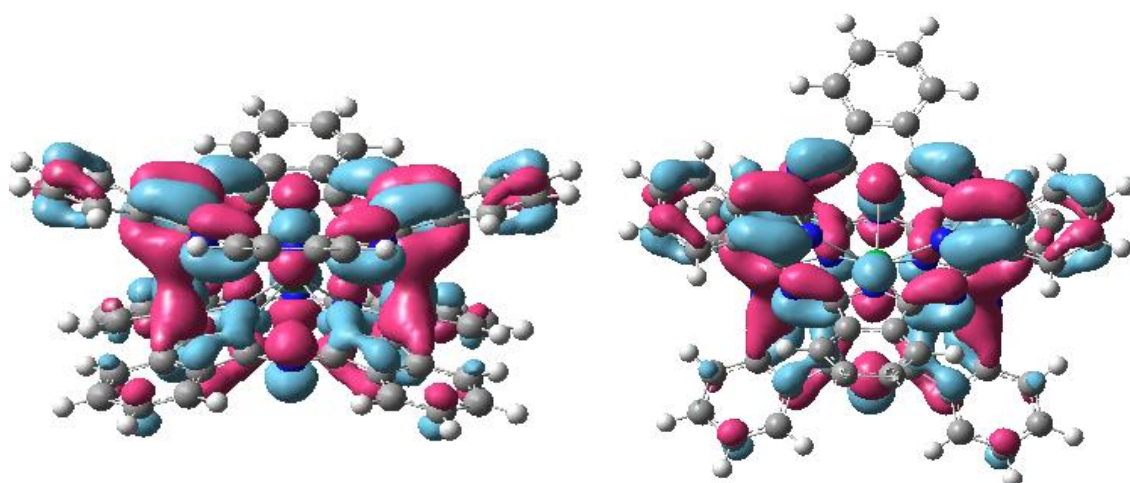
Frontier KS orbitals are predominantly associated with phthalocyanine orbitals in that they show no contributions from the metal ion.



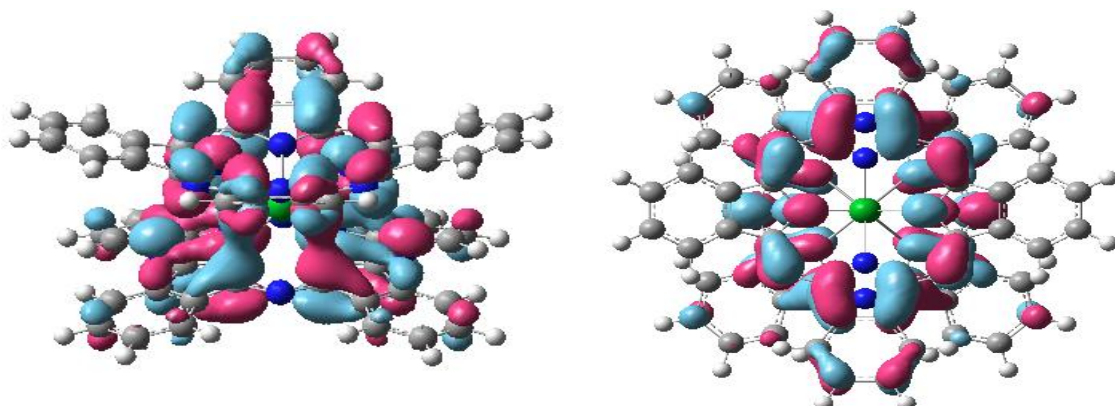
HOMO⁻¹ (-3.22 eV)



HOMO (-2.47 eV)



LUMO (0.35 eV)



LUMO+1 (0.72 eV)

Figure 27: Kohn-Sham frontier orbitals of the electronic ground state calculated with BHLYP/SV(P). The first column shows a side view while the second one gives the corresponding top view. Red and blue indicate phases of the KS orbitals.

Transitions in the simulated optical absorption spectrum are originating between the corresponding orbitals given in table 10.

Table 10: TD-BHLYP/SV(P) KS orbital contributions to optical transitions.

λ / nm	Optical excitations	Involved orbitals
856	$S_0 \rightarrow S_1$	HOMO \rightarrow LUMO
631	$S_0 \rightarrow S_2$	HOMO \rightarrow LUMO + 1
536	$S_0 \rightarrow S_3$	HOMO - 1 \rightarrow LUMO

The effect of the TBA counterion on the dimer complex was simulated by using the crystal structure geometry reported by Moussavi [129] and Koike [106]. Although this is presumably not the exact captured arrangement in solution, a similar picture where the counterion is situated in close proximity on top of one of the Pc macrocycles is emphasized by NMR experiments [107, 125].

The crystal structure geometry obtained with BHLYP/SV(P) yields an asymmetric dimer with respect to the two Pc macrocycles. This asymmetry is caused by an oblique positioning of the TBA cation above one of the rings and the DMF solvent molecules below the other. Moreover this interplay results in a partial planarization of the rings characterized by an off-planarity angle of 5.8°.

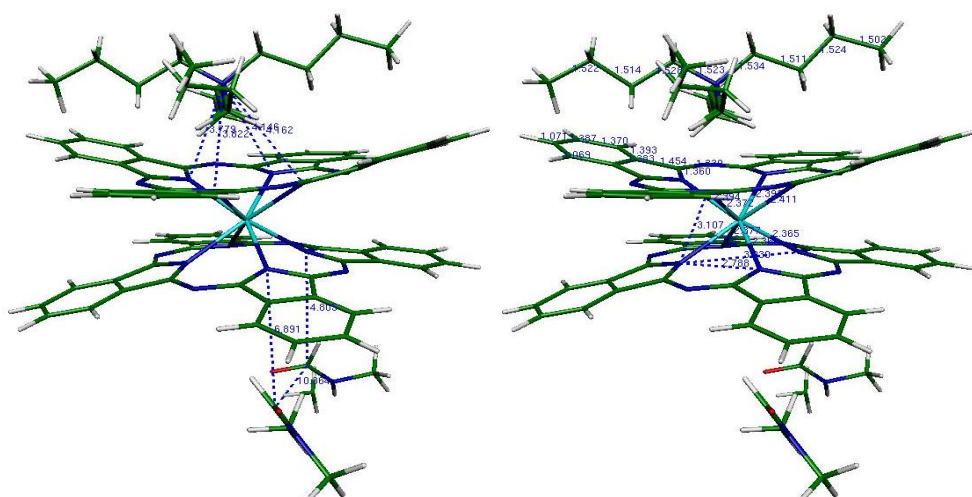


Figure 28: A visualisation of the BLYP/SV(P) crystal structure geometry of $[\text{LuPc2}]^- \text{TBA}^+$ with two DMF solvent molecules.

The complex-counterion separation ($N_{\text{TBA}}-N_{\text{iso}}$) is on average 3.97 Å in which TBA is closer to the opposite page of the solvated part of the lower ring. The average complex-solvent separation amounts to 5.8 Å.

All $\text{Lu}-N_{\text{iso}}$ and $C_{\alpha}-N_{\text{aza}}$ bonds of the dimer-counterion-solvent complex exhibit different lengths. In general $\text{Lu}-N_{\text{iso}}$ distances are smaller than in the unperturbed dimer by 1% and $C_{\alpha}-N_{\text{aza}}$ bonds increased by the same amount.

The metal-isoindole nitrogen bond lengths are unevenly distributed in that they are 0.25 % shorter on the Pc ring that is in the vicinity of the solvent molecules and by the same amount longer on the macrocycle next to the TBA counterion even though the DMF solvent molecules are farther separated from the bisphthalocyanine than the TBA counterion. The calculated $\text{Lu}-N_{\text{iso}}$ bonding lengths range from 2.363 to 2.392 Å on the lower ring to 2.372 to 2.415 Å on the upper Pc moiety. The interplanar distance is also shortened by 1% to 3.107 Å.

The $C_{\alpha}-N_{\text{aza}}$ bond distances showed a slightly stronger increase on the TBA than on the solvated Pc ring giving rise to average bond lengths of 1.334 on the former and 1.325 Å on the latter macrocycle.

Thus the net geometrical effect of the counter ion is to desymmetrize the interplanar distances, widen and partially planarize one macrocycle.

The calculation of excitation energies yielded a twofold amount of allowed transitions. This doubling is attributed to the asymmetric ring geometries which cause a lifting of degenerate transitions. The resulting splitting is rather symmetric in the Q-region giving rise to two transitions of equal intensity for each degenerate band. However the magnitude of the splitting is not uniform throughout the Q-region. The CT states are more strongly affected than the EX levels. In contrast there is only a single intense band besides a second weak one in the Soret region. These different splittings are associated with the individual environments exerted by the TBA cation and the DMF solvent molecules. Furtheron it is interesting to note that the partial planarization of the Pcs results in a redshift of the absorption bands and that the bathochromic shift is more pronounced in the Soret region.

Table 11: Vertical excitation and vertical de-excitation energies (in nm) of $[\text{LuPc}_2]^- \text{TBA}^+$ obtained from TD-BHLYP/SV(P) calculations of the crystal structure geometry. The values in parentheses represent the corresponding oscillator strengths.

BHLYP: S_0 (f)
1301 (0.00355)
1225 (0.00334)
691 (0.13109)
654 (0.14109)
574 (0.47547)
556 (0.47226)
444 (0.01713)
431 (0.83780)

Putting together electronic excitations of the dimer and the crystal structure lead to the spectra shown in fig. x.

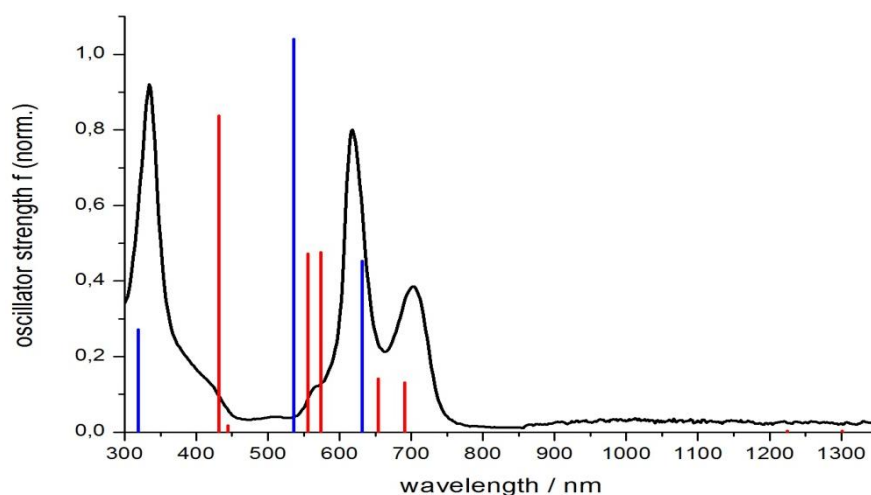


Figure 29: Experimental absorption spectrum in BN (black line) and simulated gas phase TD-BHLYP/SV(P) stick spectra. Results of the unperturbed dimer $[\text{LuPc}_2]^-$ are given in blue and those of the $[\text{LuPc}_2]^- \text{TBA}^+$ crystal structure are indicated in red.

Dicussion and trouble shooting

The rating of diverse standard functionals in the overall description of lutetium bisphthalocyanine is ascribed to the extent of exact exchange included in the corresponding

functional. BHLYP performs best since it includes 50% of non-local interaction as compared to 20 % in B3LYP and in PBE. This portion manifests itself most drastically in calculated electronic excitation energies of CT states.

The failure of TDDFT in computing charge separated states arises from the approximate nature of the exchange-correlation expression already used to compute the ground-state. It is attributed to the underlying assumption of an exponential (short-range) dependence of the electron density and vice versa the exchange potential or more specifically the exchange-kernel in TDDFT on position. In standard hybrid functionals a deviation from full exchange is introduced by applying the adiabatic approximation for mixing local exchange of DFT with non-local HF one [163, 164].

Vanishing overlap of orbitals resulting from the displacement of charge density then leads to an incorrect long-range asymptotic behavior of the exchange term since it is approximated as predominantly local but should correctly appear in the form of an attractive electron-hole Coulomb interaction (scaling as $1/R$) [165-168].

In a CT process the correct excitation energy is given as [169]

$$\omega_{CT}^{exact}(R_{DA}) \approx IP_D - EA_A - \frac{1}{R_{DA}}$$

while in TDDFT the asymptotic behavior for local functionals yields [170]

$$\omega_{CT}^{local}(R_{DA}) = (\varepsilon_j - \varepsilon_i) + 2\langle ij | f_{XC} | ij \rangle \approx \varepsilon_A^{LUMO} - \varepsilon_D^{HOMO}$$

$$\varepsilon^{LUMO} \approx -EA - \frac{\Delta_{XC}}{2} \quad \varepsilon^{HOMO} \approx -IP + \frac{\Delta_{XC}}{2}$$

Thus the lack of exact exchange-correlation underestimates the orbital energies that enter the calculation of the transition frequency by falling off too quickly (mostly exponential instead of inverse) and becomes inaccurate at large distances.

$$\omega^{local} - \omega^{exact} \approx -\frac{1}{2}(\Delta_{XC}^A + \Delta_{XC}^D)$$

This can be interpreted as a self-interaction error since the exchange-correlation potential remains unadapted owing to mainly local properties when some charge density is dislocated far off.

Correspondingly states with either excessive charge separation like Rydberg (high principal quantum number) or charge transfer just as states formed by non-local (long-range) correlation

interactions as van der Waals clusters and widely conjugated systems represent troublesome targets [163].

Computation of such molecular problem cases would require the use of particularly adapted non-standard long-range corrected functionals that are not yet implemented in commercially available software.

Possible solutions in emerging long range corrected functionals contain [171]:

- adding some exact exchange [172, 173]
- derivative discontinuity [170]
- long range corrected exchange-correlation kernel [174]
- CIS hybrid approach [166]
- hybrid meta functional [168]
- frequency dependent kernel [175]

The drawback of too low intensities in the simulated spectrum is ascribed to the neglect of configuration interaction contributions. This intensity borrowing between exciton and CT bands necessary to give correct results will arise when using computationally more expensive MRCI techniques that allow to calculate state interactions and thereby redistributions of oscillator strengths.

Summary

In summarizing the results obtained, a DFT approach works well for determination of ground state properties but gives incorrect excited state features. Differences in achieved agreement are attributed to the portion of exact exchange covered by the tested hybrid functionals. TDDFT results from convey improper excited state potential surfaces and do not support comparable evidence to ultrafast spectroscopies with regard to conical intersections between CT and EX states until new long-range corrected functionals are available.

However the performed calculations on the crystal structure show a rather significant influence of the counterion on the electronic properties of the complex. A similar break in equality of the two rings in solution would lead to a heterodimeric character favoring charge separation on one of the macrocycles. This model would suggest an electronic state as source of the 700 cm^{-1} feature that was observed with 2D-ES during excited state relaxation and indicates a charge-separated nature of the dark state.

4. Theory of Non-linear Spectroscopy

A description of time dependent condensed phase quantum systems by non-linear spectroscopy requires an extension of the usual quantum mechanical formalism to obtain a complete description of the system and its interactions with the environment and the radiation field [94-96, 176].

(a) Introduction

The wavefunction $\Psi(t)$ used to describe a pure quantum state in Hilbert space \mathcal{H} can be rewritten in terms of the more general statistical density operator that serves as a probabilistic measure in characterizing the degrees of freedom in a quantum mechanical ensemble.

The density operator representation $\hat{\rho}(t)$ not only recovers pure states $\Psi(t)$, but also enables one to deal with statistical mixtures of states and coherences necessary to account for random distributions and interactions in condensed phases [95, 177].

A pure state thereby corresponds to an ensemble that happens to be populated in only a single state or wavefunction determined by the Schrödinger equation.

$$\hat{\rho}(t) = |\Psi_i(t)\rangle \langle \Psi_i(t)|$$

A mixed state is equivalent to a system distributed over various pure states with equal probabilities p_{ij} .

$$\hat{\rho}(t) = \sum_{i,j} p_{ij}(t) |\Psi_i(t)\rangle \langle \Psi_j(t)|$$

State populations are represented by diagonal density matrix elements while off-diagonal entries, called coherences, correspond to admixtures from two different states.

An interacting system can then be seen as a collection of coupled sub-ensembles by combining fractions f_i of the individual ensemble members.

$$\hat{\rho}_{total}(t) = \sum_i f_i(t) \hat{\rho}_i \quad \sum_i f_i(t) = 1$$

In statistical mechanics a system state is represented by a point in phase space which is given in terms of a vector pointing towards its actual position. The point's coordinates at any time are determined by the system's dynamical variables and its time evolution is described as a change in current vector position. For a quantum ensemble, the same framework leads to the concept of Liouville space representations within which, the density operator (that takes on the form of a

matrix in Hilbert space) is transformed into a higher dimensional vector by action of a superoperator (an operator transforming another operator) usually referred to as the Liouvillian \hat{L} .

$$\hat{L}\hat{\rho} = \hat{\rho}' = [\hat{H}, \hat{\rho}] \quad |i\rangle\langle j| \xrightarrow{\hat{L}} |i\rangle\langle j| \equiv |ij\rangle$$

This approach offers several advantages over the conventional Hilbert space representation. Most notably it enables to describe correlated dynamics in a transparent fashion and therefore gains clear insights into the information content of different spectroscopies.

The main points for changing to Liouville space are that ^[94]:

- it's possible to simultaneously keep track of the bra and ket time-evolutions (interactions with the radiation field) because the time variables are ordered,
- the Liouvillian operator is linear with respect to the response of the density operator in Liouville space whereas it's non-linear in Hilbert space,
- reduced descriptions of the density operator are easily accessible by tracing over the bath and therefore concentrating only on a few relevant degrees of freedom,
- no thermal averages need to be calculated explicitly because the whole phase space density that represents the thermal system is propagated,
- a phenomenological description of the relaxation process that includes dephasing (decoherence) is possible by an additional relaxation operator.

The time-evolution of the density matrix is governed by the Liouville–von Neumann equation

$$\frac{d\hat{\rho}(t)}{dt} = -\frac{i}{\hbar} [\hat{H}(t), \hat{\rho}(t)] = -\frac{i}{\hbar} \hat{L}(t)\hat{\rho}(t)$$

in which the Liouville superoperator appears as the commutator of the density matrix with the Hamiltonian ^[94-96, 176]. The full Hamilton operator is given as

$$\hat{H}(t) = \hat{H}_S(t) + \hat{H}_B(t) + \hat{V}_{SB}(t) + \hat{V}_{SR}(t)$$

Here H_S denotes the Hamilton of the unperturbed system, V_{SB} the interaction of the system with its environment (the bath) and V_{SR} the system-radiation interaction of the system with the electromagnetic field.

The system-bath part describes how the system properties are affected by the presence of an environment. In the realm of non-linear spectroscopy the bath dynamics influence relaxation and energy transfer within the molecule and dissipation to the environment.

The system-radiation part induces transitions between suitable levels depending on the field applied and serves as a probe to disentangle various molecular processes and interactions. The obtained information includes static system parameters like energetic separations and symmetries as well as dynamics if the time resolution is faster than the investigated system processes.

System Hamiltonian

The system Hamiltonian describes the system's electronic structure in contact with diverse influences such as the environment and radiation fields. The material system is usually encountered as a level scheme extracted by quantum chemical calculations from the time-independent Schrödinger equation. The level structure is then taken as a starting point to describe various perturbations acting onto it. A more detailed inquiry of lutetium bisphthalocyanine is given in the quantum chemistry part and / or cited literature.

Especially interesting to non-linear spectroscopy are systems with coupled or interrelated states in the sense that both mutually depend on each other. Perturbing one of these states also reports on the change of its coupled counterpart and thus provides information that would often not be accessible otherwise. In the case of the synthesized dimer complex such a coupling exists between the exciton and charge transfer states. The CT band gains its brightness through intensity borrowing from configuration interaction with the allowed transition to the exciton state and thereby enables its spectroscopic survey on ultrafast timescales.

(b) System-Bath Hamiltonian

The full system-bath Hamiltonian consists of $\hat{H}_S(t)$ and $\hat{H}_B(t)$ governing the individual system and bath dynamics and an interaction term $\hat{V}_{SB}(t)$ coupling both together. The system usually consists of electronic states and the bath of vibrations. The size of the bath requires to focus attention on the dynamical behavior of the system in a reduced description of the density operator, abbreviated $\hat{\sigma}$.

$$\hat{H}_{SB}(t) = \hat{H}_S(t) + \hat{H}_B(t) + \hat{V}_{SB}(t) \xrightarrow{tr_B} \hat{H}_{SB}^{reduced} = \hat{H}_S(t) + \hat{V}_{SB}(t)$$

The exact dynamics of the bath are considered implicitly by tracing over the environmental degrees of freedom and projecting the component density matrix into the system subspace which is equivalent to drag the bath along as a perturbation to the relevant regards in the system. The influence of the bath in the reduced description enters through the system-bath interaction term that is treated classically as a random force [95, 96].

$$\hat{\sigma}_s = \hat{\rho}_{SB}^{reduced}(t) = \text{tr}_B(\hat{\rho}_{SB}(t)) = |\psi_s(t)\rangle \langle \psi_s(t)| \delta_{B,B'}$$

The time-evolution of the system-bath interaction can be displayed separately from the reduced system evolution in the interaction picture denoted by index I . Therein the total Hamiltonian is split into the time evolution of a stationary part corresponding to the unperturbed system and some additional small time-dependent deviation from the evolving unperturbed state caused by the system-bath interaction.

$$\frac{d\hat{\sigma}_I(t)}{dt} = -\frac{i}{\hbar} \text{tr}_B \left(e^{\frac{i}{\hbar}\hat{H}_0 t} [\hat{V}_{SB}(t), \hat{\rho}_{SB}(t)] e^{-\frac{i}{\hbar}\hat{H}_0 t} \right)$$

Tracing out the environment from the equation of motion is done by using projection operators in the weak coupling limit so that the resultant equation restricts the dynamics to the system subspace. The dissipative system dynamics induced by the system-bath interactions are then given in form of a quantum master equation

$$\frac{d\hat{\rho}(t)}{dt} = -\frac{i}{\hbar} \hat{L}(t)\hat{\rho}(t) - \frac{i}{\hbar} \hat{R}(t)\hat{\rho}(t)$$

where \hat{R} denotes a relaxation superoperator.

The environment appears via correlation functions of bath operators in the system-bath interaction term [95].

$$\frac{d\hat{\sigma}_I(t)}{dt} = -\frac{i}{\hbar} [\hat{V}_I, \hat{\sigma}_I] - \frac{1}{\hbar^2} \int_0^t (C_B(t-\tau) [\hat{V}_I^S(t), \hat{V}_I^S(\tau)\hat{\sigma}_I(\tau)] - C_B^*(t-\tau) [\hat{V}_I^S(t), \hat{\sigma}_I(\tau)\hat{V}_I^S(\tau)]) d\tau$$

Herein the time-evolution of the reduced system not only depends on the evolution of the sample subspace S but through its initial coupling to the bath also on the history of their interactions given by the correlation functions C_B .

The effect of a large, fluctuating surrounding on any excess energy stored within the systems electronic states (spectroscopically the photons angular momentum) is to perturb its evolution

and provide an irreversible exit channel. Such a reservoir initially leads to relaxation or redistribution of energy across the system and finally accepts and dissipates it.

The relaxation operator point of view is most conveniently outlined when expressing the reduced evolution in the energy level or site representation of the system in the Schrödinger picture (dynamics of $H_0 + V_{SB}$ are no longer separately treated) and introducing a coupling correlation function to other system states and certain bath degrees of freedom [95].

$$\frac{d\sigma_{ab}(t)}{dt} = -\frac{i}{\hbar} [\hat{H}_S, \hat{\sigma}]_{ab} - \frac{i}{\hbar} [\hat{V}, \sigma]_{ab} + \left(\frac{d\sigma_{ab}}{dt} \right)_B$$

The last term contains the thermal relaxation (energy dissipation to the bath) and is made up from integrals over memory kernels of the coupling correlation functions. This expression usually needs to be approximated to get manageable results.

One of the most common simplifications is the Redfield approximation where initial correlations are neglected, the time scales are separated so that relaxation in the bath is faster than in the system or invoking Markovian behavior and weak coupling between the considered states is assumed by calculating the relaxation superoperator $R_{ab,cd}$ to second order in the system-bath couplings. The approximations are consistent with the idea of a time evolving reservoir in the background whose slow equilibrium fluctuations facilitate relaxation and accept excess energy through weak coupling to the system [95].

The general Redfield equations provide equations of motions describing coupled dissipative dynamics of populations (diagonal tensor elements) and coherences (off-diagonal elements) [178, 179].

$$\frac{d\sigma_{ab}(t)}{dt} = -i\omega_{ab}\sigma_{ab} - \sum_{c,d} R_{ab,cd}\sigma_{cd}(t)$$

The first term describes the free exciton system while the relaxation superoperator allows to incorporate transport rates and dephasing times.

The assumptions involved in general Redfield theory do not guarantee physically acceptable density matrices, those with conserved populations and positive eigenvalues since they correspond to state probabilities in a diagonal matrix form, for all parameter regimes (especially for strong couplings between populations and coherences as observed in light harvesting systems and bacterial reaction centers).

There are two applicable possibilities to extend its limitations:

The first one utilizes a decoupling of population and coherence dynamics of the generalized Redfield equation by employing the secular approximation which only retains autocorrelations in the relaxation tensor ^[178, 179]. The resulting tensor describes population decay and transport by a classical Pauli master equation and coherence loss by dephasing rates.

$$R_{ab,cd}^{\text{secular}} = (\delta_{ab}\delta_{cd} + \delta_{ac}\delta_{bd}(1 - \delta_{ab}\delta_{cd}))R_{ab,cd}$$

This yields correct behavior (constant trace at all times and positive definiteness) but fails to explain some experimentally observable effects associated with their simultaneous evolution that are taken as evidence for quantum transport in these systems ^[178, 179].

An alternative approach that enjoys special popularity is given by the Lindblad equation which generalizes the Redfield relaxation tensor in the secular approximation and allows to recast the couplings between populations and coherences while still ensuring physically acceptable results ^[178, 179]. It does so by defining a subspace of acceptable relaxation tensors for the density matrix dynamics using dynamical semigroups. Its general form reads ^[178, 179]

$$\frac{d\rho_{ab}(t)}{dt} = -i\omega_{ab}\rho_{ab} + \sum_{\alpha} \sum_{c,d} \left(V_{ac}^{(\alpha)} \rho_{cd} (V_{bd}^{(\alpha)})^* - \frac{1}{2} \rho_{ac} (V_{dc}^{(\alpha)})^* V_{db}^{(\alpha)} - \frac{1}{2} (V_{ca}^{(\alpha)})^* V_{cd}^{(\alpha)} \rho_{db} \right)$$

where $V^{(\alpha)}$ denotes operators in the system subspace that couple it to the bath. A general problem consists in determining these operators since no procedure exists for their derivation and most implementations are therefore phenomenological.

The fluctuating random force exerted on the system in condensed phases manifests itself through broadening of spectral lines. The lineshape function $g(t)$ allows to deal with environmental fluctuations on different time scales as compared to the considered system processes ^[91-93]. The system time scale is usually described relative to the surrounding bath fluctuations by the correlation time τ_c . Defining this system-bath time relation is necessary to account for the classification of broadening mechanisms observed with a given experimental time resolution. Processes that are faster than the experimental time resolution cannot be resolved and are called homogenous or intrinsic while the resolvable slower ones seems to be extrinsic and are thus termed inhomogeneous.

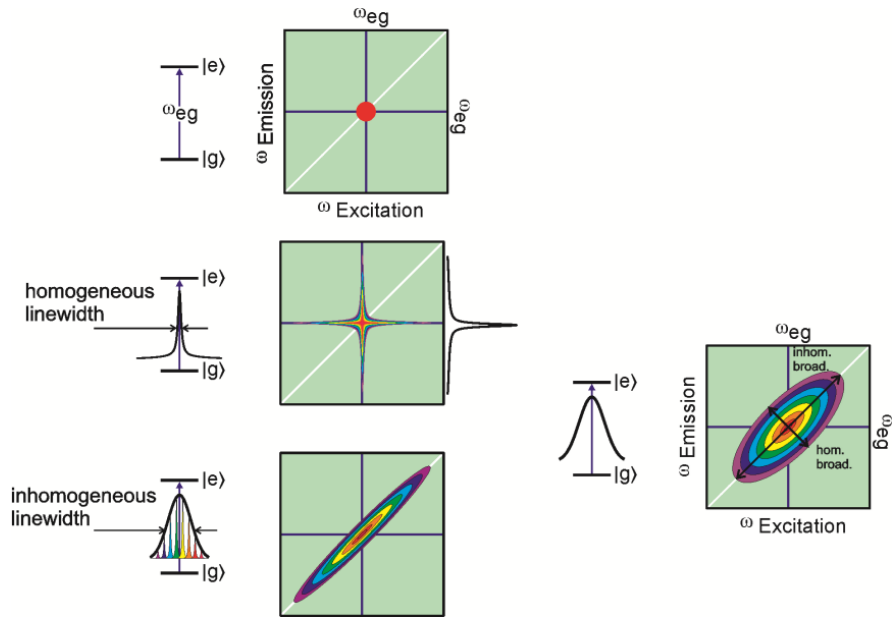


Figure 30: Recorded 2D-ES spectra correlate excitation and emission transition energies in a frequency-frequency plot. The linewidths directly display prevalent molecular dynamics and system-bath interactions in the frequency domain. Line broadenings are classified as homogeneous and inhomogeneous depending on their timescale relative to the experimental time resolution.

Relaxation effects contribute to line broadening because a loss of energy in time domain (a damped oscillation) is linked to a distribution of frequencies in the spectral representation. Population or amplitude relaxation and dephasing or loss of common phase relations are dynamic effects classified as homogeneous broadenings [97].

A static mechanism of linebroadening originates from a distribution of oscillators that are energetically different due to the instantaneous environment and is termed inhomogeneous broadening [97].

Dephasing and inhomogeneous broadening are also rated as ensemble effects while population relaxation is an intrinsic molecular property [97].

The lineshape function $g(t)$ is usually modeled on different levels of sophistication using either Kubo's stochastic theory [180] or a Brownian oscillator model [181].

Kubo's stochastic theory [180] describes the fluctuations of the energy gap on different correlation time-scales τ_c thereby enabling one to distinguish between homogeneous and inhomogeneous broadenings. The perturbations of the transition dipole due to stochastic forces of the environment are described by the transition-frequency autocorrelation function $C(t) = \Delta^2 e^{-t/\tau_c}$ where the coupling strength of modes to the electronic dipole is given by Δ .

$$g(t) = \Delta^2 \tau_c^2 (e^{-t/\tau_c} + t/\tau_c - 1)$$

The Brownian oscillator model [181] additionally depicts dissipation (reorganizations λ_k) by including the system's internal degrees of freedom (as underdamped vibrations) besides the environmental modes (overdamped oscillations). The lineshape function is given as a sum of individual Brownian oscillators that are labeled by the index k . Its real part characterizes spectral broadening of absorption lines through the transition-frequency autocorrelation function $C(\tau)$ and governs the coupling strength Δ between system modes on different potential curves. Its imaginary part is related to the Stokes shift via the reorganization energy λ_k and the displacement of the potential curves ΔQ via .

$$g(t) = \sum_k g_i(t) = \sum_k \left(\int_0^t \int_0^{\tau_1} \Delta_k^2 C_k(\tau_2) d\tau_1 d\tau_2 + i\lambda_k \int_0^t C_k(\tau) d\tau \right)$$

This time domain description of system-bath interactions reflects the underlying molecular dynamics because transition dipole fluctuations are sensitive to molecular configuration.

The frequency-domain analogon (or cos-Fourier-transform) of the lineshape function is the temperature-independent spectral density $J(\omega)$ that describes the coupling strengths and spectrum of modes modulating the transition frequency [94]. The *coth*-term reflects the boson distribution of the phonon-bath at a certain temperature $\beta=1/k_B T$.

$$g(t) = \frac{1}{2\pi} \int_{-\infty}^{\infty} \frac{1 - \cos(\omega t)}{\omega^2} \coth\left(\frac{\beta\hbar\omega}{2}\right) J(\omega) d\omega + \frac{i}{2\pi} \int_{-\infty}^{\infty} \frac{\sin(\omega t) - \omega t}{\omega^2} J(\omega) d\omega$$

(c) System-radiation Hamiltonian

An expression for the systems response to the spectroscopic survey is found when concerning the light-matter interaction expression.

The interaction potential of the system-radiation contribution in the total Hamiltonian is given semiclassically as the product of the dipole operator constituting the system times the field. The system is figured as a quantum mechanical level scheme while the electromagnetic field $\vec{E}(\vec{r}, t)$ is treated classically as a plane wave [83].

$$\hat{V}_{SR}(t) = \hat{\mu} \cdot \vec{E}(\vec{r}, t) = (-e \cdot \hat{r}) \cdot \vec{E}(\vec{r}, t)$$

$$\bar{E}(\bar{r}, t) = \sum_n \bar{E}_n(\bar{r}, t) = \sum_n A_n^0(t_n) \cdot e^{-i\omega_n t_n + i\bar{k}_n \bar{r}} + A_n^{0*}(t_n) \cdot e^{i\omega_n t_n - i\bar{k}_n \bar{r}}$$

The systems deviation from its equilibrium state through sequential interactions with the light fields is represented by a perturbative expansion of the density operator in the orders of the field [94]:

$$\hat{\rho}(t) = \hat{\rho}^{(0)}(t) + \hat{\rho}^{(1)}(t) + \hat{\rho}^{(2)}(t) + \hat{\rho}^{(3)}(t) + \dots + \hat{\rho}^{(n)}(t)$$

$$\hat{\rho}^{(n)}(t) = \left(\frac{i}{\hbar}\right)^n \int_0^\infty \dots \int_0^\infty \bar{E}(\bar{r}, \tau_n) \dots \bar{E}(\bar{r}, \tau_2) \bar{E}(\bar{r}, \tau_1) \cdot \hat{G}(\tau_n) \hat{\mu} \dots \hat{G}(\tau_2) \hat{\mu} \hat{G}(\tau_1) \hat{\mu} \hat{\rho}(-\infty) d\tau_n \dots d\tau_2 d\tau_1$$

The model assumptions in the interaction potential of the perturbations result in an overall transition dipole moment whose expectation value corresponds to the central variable of spectroscopy, the macroscopic polarization $\bar{P}(t)$ [94]:

$$\bar{P}^{(n)}(t) = \langle \langle \hat{\mu} | \hat{\rho}^{(n)}(t) \rangle \rangle = tr [\hat{\mu}, \hat{\rho}^{(n)}(t)] = tr \hat{\mu} \hat{\rho}^{(n)}(t)$$

According to the Maxwell's equations the observable quantity of the polarization is proportional to an electric field $\bar{E}_{signal}^{(n)}(\bar{r}, t)$ that is generated by the time dependent change of the induced charge density [89].

$$\bar{E}_{signal}^{(n)}(\bar{r}, t) \cong \frac{2\pi i d \omega}{n(\omega) c} \bar{P}^{(n)}(t)$$

The irradiated polarization is related to the non-linear response function of the system emerging from the consecutive perturbations by the fields via [94]:

$$\bar{P}^{(n)}(t) = \int_0^\infty \dots \int_0^\infty \bar{E}_n(\bar{r}, \tau_n) \dots \bar{E}_2(\bar{r}, \tau_2) \cdot \bar{E}_1(\bar{r}, \tau_1) \cdot R^{(n)}(\tau_1, \tau_2, \dots, \tau_n) d\tau_n \dots d\tau_2 d\tau_1$$

Here the response function $R^{(n)}(\tau_1, \tau_2, \dots, \tau_n)$ is given by [94]

$$R^{(n)}(\tau_1, \tau_2, \dots, \tau_n) = \left(\frac{i}{\hbar}\right)^n \langle \langle \hat{\mu} | \hat{G}(\tau_n) \hat{\mu} \dots \hat{G}(\tau_2) \hat{\mu} \hat{G}(\tau_1) \hat{\mu} | \hat{\rho}(-\infty) \rangle \rangle$$

It is seen that the response functions consist of a sequence of interactions indicated by the dipole superoperators $\hat{\mu}$ that are separated by periods of free evolution of the system described by the Greens function propagator $\hat{G}(\tau_n)$ which reads [94]

$$\hat{G}(\tau_n) = \theta(\tau_n) \cdot e^{\frac{i}{\hbar} \hat{L}_0 \tau_n}$$

where $\theta(\tau_n)$ denotes the Heaviside step function.

The following graph represents a diagrammatic approach to picture the molecular perturbations caused by the system-radiation interactions [97]:

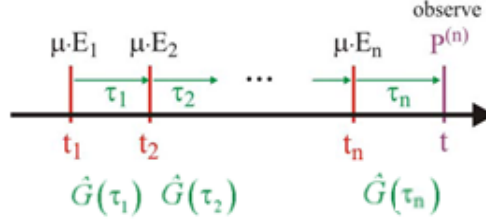


Figure 31: A diagrammatic picture of system-radiation interactions [97].

The timing of interactions can be given in terms of absolute values t_n defined with respect to the polarization or in time intervals τ_n [94].

$$\tau_j = \left(t - \sum_{\alpha=n}^1 t_\alpha \right) - \left(t - \sum_{\beta=n}^{\alpha-1} t_\beta \right)$$

The measured signal field resulting from the n th order polarization is raised by the molecular response function $\bar{E}_{signal}^{(n)}(\vec{r}, t) \approx P^{(n)}(t) \approx R^{(n)}(\tau_1, \tau_2, \dots, \tau_n)$ and is usually recorded by the spectrograph in the frequency domain. Therefore either the spectral representation of the response function or a Fourier transformation of the emerging signal field in the time domain will correspond to the collected spectrum $S^{(n)}(\omega_1, \omega_2, \dots, \omega_j)$ [94].

A Fourier-Laplace transform of the polarization with respect to the time intervals allows us to obtain an expression for the n th order nonlinear susceptibility $\chi^{(n)}(\omega_{signal}; \omega_1, \omega_2, \dots, \omega_n)$ that represents the frequency domain analogon of the non-linear response function [94]:

$$P^{(n)}(\omega_{signal}) = \chi^{(n)}(\omega_{signal}; \omega_1, \omega_2, \dots, \omega_n) \bar{E}_1(\vec{r}, t) \bar{E}_2(\vec{r}, t) \dots \bar{E}_n(\vec{r}, t)$$

$$\chi^{(n)}(\omega_{signal}; \omega_1, \omega_2, \dots, \omega_n) = \int_0^\infty \dots \int_0^\infty e^{i\Omega_n \tau_n} \dots e^{i\Omega_2 \tau_2} e^{i\Omega_1 \tau_1} \cdot R^{(n)}(\tau_1, \tau_2, \dots, \tau_n) d\tau_n \dots d\tau_2 d\tau_1$$

On the other hand Fourier-transformation of the emerging signal field with respect to the appropriate time-delays $d\tau_j$ will also resemble the spectrum.

$$S^{(n)}(\omega_1, \omega_2, \dots, \omega_j) = \int_0^\infty \dots \int_0^\infty e^{i\Omega_j \tau_j} \dots e^{i\Omega_2 \tau_2} e^{i\Omega_1 \tau_1} \bar{E}_{signal}^{(n)}(\vec{r}, \tau) d\tau_1 d\tau_2 \dots d\tau_j$$

Within the established formalism different kinds of non-linear spectroscopies differ in the time orderings (sequence), the spatial constellations (wavevector arrangements) and frequencies of the interrogating pulses. The number of field interactions with the system then results in the corresponding order of its response function that tracks the induced higher order correlations and connects them to the associated molecular polarization. Each non-linear response function comprises the sum over all possible Liouville pathways (perturbations originating for the used set of field parameters) contributing to a specific polarization [94].

An elegant graphical visualization of the spectroscopic dynamics is provided by double-sided Feynman diagrams [97].

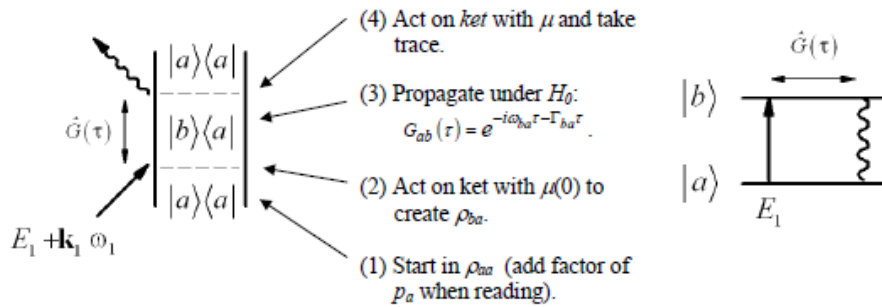


Figure 32: A graphical illustration of a system-radiation interaction given in by its double-sided Feynman diagram (left) or in terms of a wave mixing diagram (right) [97].

Herein time is running from the bottom to the top, interactions with the various states are indicated by the arrows (excitation is symbolized by arrowheads pointing toward the affected side whereas deexciting arrows points away from the affected side), free evolutions are indicated by periods between interactions and the overall response is depicted by the curly arrow leaving the system.

The same information can in principle be obtained from wave mixing diagrams where a dotted arrow indicates interaction on the bra and a full arrow interaction on the ket side. The time is evolving from left to right and the systems response is denoted by a curly arrow.

Conventions commonly used to construct both kinds of diagrams from the corresponding equations are summarized in table 12 [97].

Table 12: Rules for translating equations into respective Feynman and wave-mixing diagrams ^[97].

<i>Interaction</i>	<i>Diagrammatic Representation</i>	contrib. to $R^{(n)}$	contribution to \mathbf{k}_{sig} & ω_{sig}
<u>KET SIDE</u>			
Absorption $(\bar{\mu}_{ba} \cdot \bar{E}_n) \exp[i\bar{k}_n \cdot \bar{r} - i\omega_n t]$		$\bar{\mu}_{ba} \cdot \hat{\epsilon}_n$	$+\mathbf{k}_n \quad +\omega_n$
Stimulated Emission $(\bar{\mu}_{ba} \cdot \bar{E}_n^*) \exp[-i\bar{k}_n \cdot \bar{r} + i\omega_n t]$		$\bar{\mu}_{ba} \cdot \hat{\epsilon}_n$	$-\mathbf{k}_n \quad -\omega_n$
<u>BRA SIDE</u>			
Absorption $(\bar{\mu}_{ba}^* \cdot \bar{E}_n^*) \exp[-i\bar{k}_n \cdot \bar{r} + i\omega_n t]$		$\bar{\mu}_{ba}^* \cdot \hat{\epsilon}_n$	$-\mathbf{k}_n \quad -\omega_n$
Stimulated Emission $(\bar{\mu}_{ba}^* \cdot \bar{E}_n) \exp[i\bar{k}_n \cdot \bar{r} - i\omega_n t]$		$\bar{\mu}_{ba}^* \cdot \hat{\epsilon}_n$	$+\mathbf{k}_n \quad +\omega_n$
SIGNAL EMISSION: (Final trace, convention: ket side)		$\bar{\mu}_{ba} \cdot \hat{\epsilon}_m$	

(e) Third-order spectroscopies: Four-level system

Third order nonlinearities describe the majority of coherent multidimensional experiments in the optical regime performed nowadays including pump-probe (PP) -, transient grating (TG) -, photon echo (PE)- and degenerate four wave mixing (DFWM) experiments like two-dimensional electronic (2D-ES) and two-dimensional double quantum (2Q-2D) coherence spectroscopies ^[97].

Due to the underlying differences in the arrangement of interaction terms the diverse third order spectroscopies initiate different responses by launching distinct pathways and thereby probe assorted parts of the dynamics in the sample.

Hence an enumeration of all possible Liouville pathways (combinations of sequential bra and ket interactions) contributing to the third order response function is vital to the further discussion of the collected data ^[90].

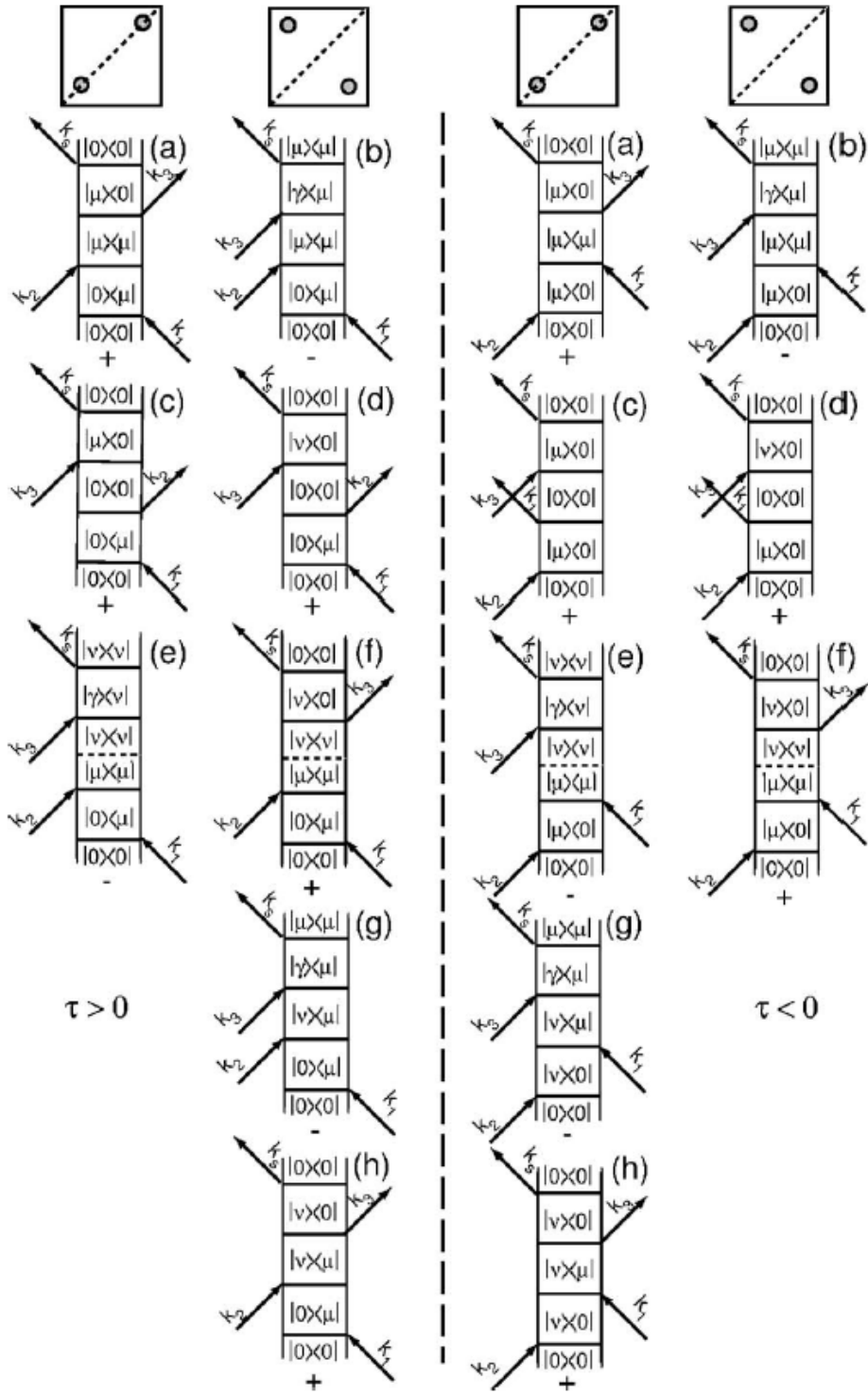


Figure 33: Feynman diagrams illustrating the constituting pathways of a four level system. Their locations in the resulting 2D spectrum are indicated by the row header, respective signs are given by + or – underneath the individual responses and separation into rephasing (left, $\tau > 0$) and non-rephasing (right, $\tau < 0$) diagrams is indicated by the central dashed line. The state labels denote 0 as the ground state, μ as an one-exciton state, v as a distinct one-exciton state and γ as a two-exciton state. Relaxation is depicted by a dashed horizontal line in the diagram^[90].

Pathways (a) and (f) correspond to simulated emission (SE). The irradiated polarization k_s stems from a coherence between the ground and a one-exciton (or singly excited) state which is created by the third interaction following a t_2 -evolution in the excited state. Pathways (b) and (e) are excited state absorption (ESA) signals. The excited state population is driven down during t_3 in a polarization that matches the difference frequency of a singly and doubly excited (two-exciton) state. Pathways (c) and (d) display ground state bleaches (GSB) characterized by evolution in the ground state during t_2 and a ground-one exciton state coherence radiating the signal during t_3 . Besides this signal contributions there are also pathways evolving in a coherence or a superposition of states during t_2 . Graphs (g) and (h) exemplify such oscillating signal paths where (g) correspond to ESA coherence and (h) to SE coherence pathways [190].

The sign of each individual signal contribution is determined by the prefactor $(-1)^n$ where n corresponds to the number of interactions on the bra side. The minus is associated with the bra side since it carries the minus sign in the commutator. The respective sequences of interactions impose a positive sign on GSB and SE contributions while ESA signals are negative [182].

These pathways apply to 2D-ES, PP and TG as all of the techniques make use of the same interactions but with different time orderings. Free choice of all interactions in 2D-ES singles out its unique position among third-order spectroscopies. A separation of the first two interactions enables 2D-ES to map out and correlate two evolution periods separated by intervening population times residing in different accessible states. The correlation of transition frequencies during the first and third time interval determines the position of occurrence of a peak in the 2D plot. Evolutions involving the same constellation of superposed states end up on the diagonal at $\omega_1 = \omega_3$ whereas differing excitation and emission energies ($\omega_1 \neq \omega_3$) give rise to off-diagonal elements that indicate connections of the involved states [85].

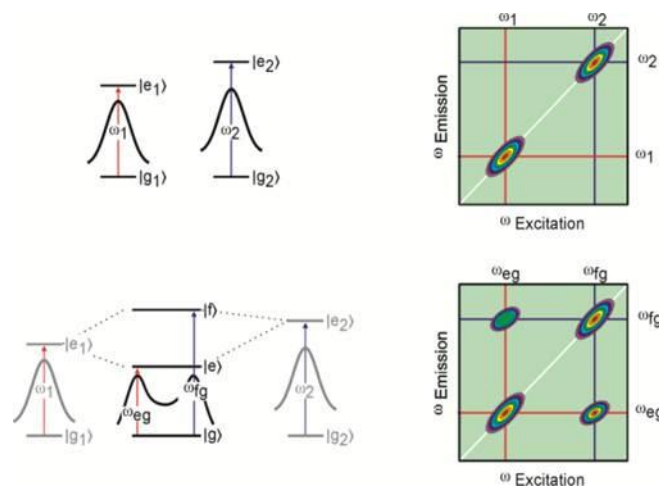


Figure 34: Depiction of the origin of cross-peaks in a coupled system. The top panel sketches two unrelated electronic oscillators that emit at their intrinsic frequencies. The lower panel represents a system coupled via a common ground state. Admixtures of monomeric transition frequencies in the underlying Liouville pathways give rise to cross-peaks.

Reversal of time ordering of the first two interactions allows for variation of the constituting pathway contributions of diagonal and off-diagonal peaks in rephasing and non-rephasing 2D signals. In contrast PP and TG lack this degree of freedom since the first time delay is zero and thus all pathways are present in the collected signals.

Its intermediate sojourn in a certain state during t_2 makes a pathway sensitive to the corresponding populated state, that is ESA and SE are perceptive to the excited and GSB to the ground state.

During pulse overlap additional pathways are contributing to the resulting polarization since the order of interactions is not fixed. Relevant diagrams originate from combinations of interchanged k_3 and k_1 interactions that involve two perturbations on the ket side thus creating a double-quantum coherence, a superposition of the ground and a two-exciton state ^[90]. An admixture of such pathways can arise additional features through their imbalanced partition to rephasing and non-rephasing signal contributions.

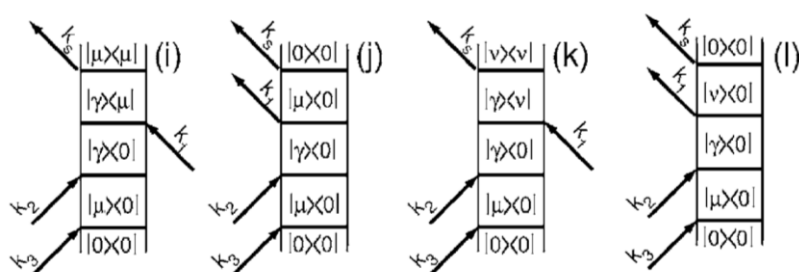


Figure 35: Feynman diagrams illustrating double-quantum coherence pathways during pulse overlap ^[90].

5. Experimental Ultrafast Spectroscopy

Ultrafast molecular dynamics are investigated by third-order spectroscopies. The lasersystem generating suitable pulses and the experimental set-up employed to handle multiple non-linear optical four-wave-mixing (FWM) techniques is described below.

(a) Lasersystem

The system used consists of an Coherent IR diode array seeding an intracavity frequency-doubled continuous wave solid-state Nd:YVO₄ laser (Coherent VERDI-V18) yielding 16 W output at 532 nm. 6 W of this output is used to pump a Coherent MIRA SEED oscillator in which initial pulses are obtained in a Ti:sapphire crystal by Kerr lens modelocking. Therein an intensity dependent refractive index passively sharpens the generated coherent white light continuum to pulses at prevalent field intensities. Performance of the oscillator is optimized for operation at 800 nm by appropriate alignment of the cavity and its compression unit. The resulting pulsed output is specified to give 420 mW at 76 MHz repetition rate corresponding to roughly 30 fs pulses or 5.5 nJ pulse energy. An intermediate Coherent stretcher-compressor integrity temporally elongates the oscillator discharge by spectrally dispersing it with a grating system to avoid damage of the amplifier. The Coherent REGA 9050 regenerative amplifier is excited by 10 W of Verdi emission and synchronized to the oscillator output by an acousto-optical modulator. The amplifier enhances each injected pulse to maximum intensity by Q-switching, that is repeatedly passing it through a gain medium and ejects the amplified beam with a cavity dumper to the compressor. The 800 nm output is then recompressed in the same stretcher-compressor unit as before setting-off 45 fs pulses of 25 nm width and 5 μ J power and 200 kHz repetition rate.

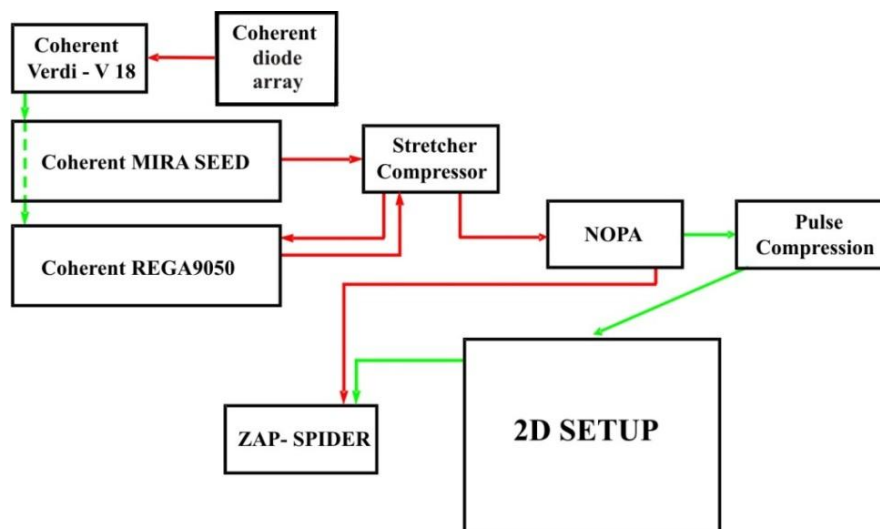


Figure 36: Scheme of the fs-lasersystem used to generate suitable pulses.

The central excitation wavelength can be tuned through-out the visible by frequency conversion in a homebuilt non-collinear optical parametric amplifier (NOPA) following pulse optimization by a combination of Brewster angle chirped mirrors and a fused silica prism compressor of variable length.

(b) Non-Collinear Optical Parametric Amplifier (NOPA)

Frequency conversion of the fundamental is achieved in a single stage process at non-collinear geometry to increase the tunability bandwidth by improving the group-velocity mismatch [183]. The compressor output is divided into a 10 % and a 90 % component at a 10/90 beamsplitter. The low energy beam is delayed with respect to the high energy one at a delay stage of μm accuracy and focused ($f=200\text{ mm}$) into a sapphire plate ($d=1\text{ mm}$) creating a white light continuum (WLC) from 400 – 800 nm [184]. A focussing lens ($f= 250\text{ mm}$) aims the WLC at a Barium- β -borate (BBO) crystal where it is mixed with the frequency doubled (400 nm) component. The latter was produced by second harmonic generation (SHG) in a BBO ($d= 300\ \mu\text{m}$) through focusing with a 200 mm lens, temporally stretching it in a fused silica block and directing it at an angle into the NOPA-BBO ($d=3\text{ mm}$) [185]. Introduction of a delay between the white light and the stretched SHG beam of the 90% component allows for specific retardation of frequency components (λ -delay) and correspondingly leads to variation in their temporal overlap at the NOPA-BBO. This modified coincidence in the crystal permits to generate suitable output frequencies by a parametric amplification process among 400 nm pump and 800 nm seed light. The wavelengths of the created idler photons depend on the chosen delay at constant phase matching angle [186]. The resulting NOPA emission centered at 650 nm typically comprises a FWHM of 45 nm with an energy of 180 nJ per pulse.

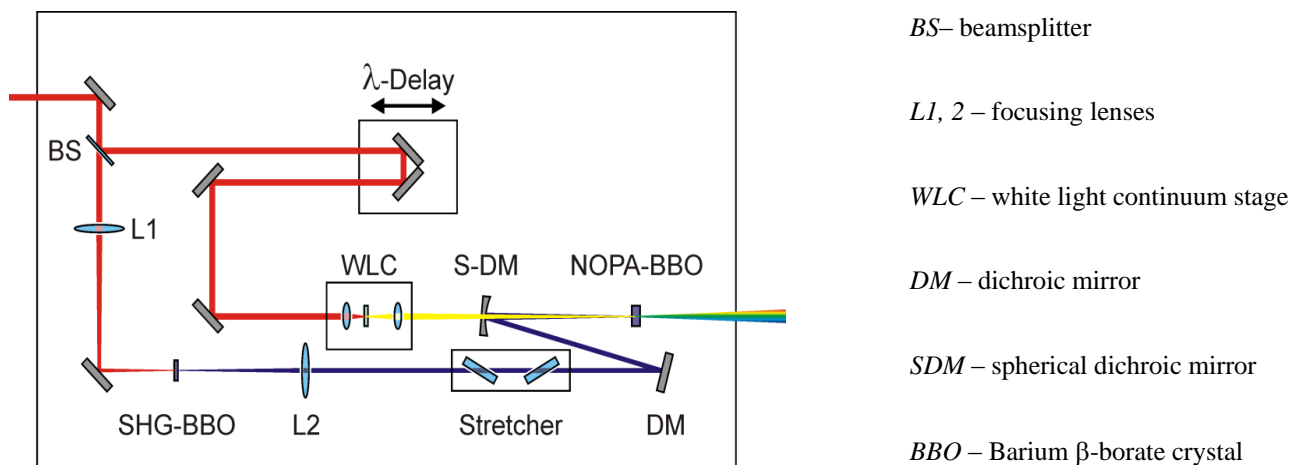


Figure 38: Compression of tuned NOPA pulses (green) with chirped mirrors and a prism compressor of variable length. The collimated beam passes through the chirped mirrors with its optimal number of reflections determined by the central wavelength and is then forward- and back-propagated through fused silica prisms ^[187].

(d) Pulse Characterization

Characterizing the compressed NOPA pulse is done by means of a simple frequency resolved autocorrelation in a SHG BBO crystal. The SHG spectrum resulting from a pair of temporally and spatially overlapping replica of the considered pulse are recorded spectrally resolved and the resulting FWHM is taken as a measure of the temporal length. The phase of the pulse can be retrieved using frequency resolved optical gating (FROG) ^[191, 192] or zero-additional phase spectral phase interferometry for direct electric field reconstruction (ZAP-SPIDER) ^[193, 194]. Since reconstructions of the phase from FROG traces are mathematically unambiguous ^[191] and ZAP-SPIDER measurements become noticeably more difficult with decreasing pulse duration a frequency resolved autocorrelation (AC) was taken as indication of the pulse quality. This approach was chosen because the collected SHG signals yielded characteristics of a properly compressed pulse verified by small and symmetric satellites (on the order of 3 %). Although wings in the AC do not yield information on their origin i.e. either uncompressed residuals or a non-Gaussian spectrum, their magnitude is indicative of a largely flat phase across the AC signal as the conversion of any Fourier-limited or Gaussian pulse from time- to frequency domain again results in a Gaussian without residuals. This Fourier transformation of the time-domain AC signal is implicitly performed by the detector through spectrally dispersed, time integrated data acquisition. Fourier limited pulses are required to ensure a homogenous excitation profile across the beam owing to their chirp free character and are denoted by a bandwidth product of 0.44 ^[195]. The achieved pulse duration of 9.2 fs at 650 nm yields a bandwidth product that indicates 5% chirp.

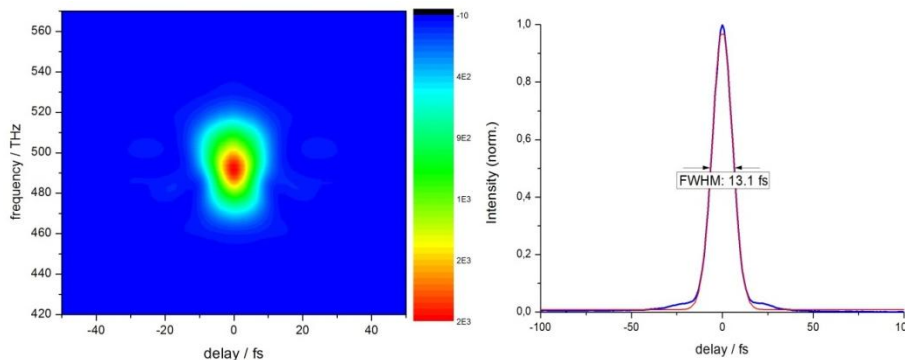


Figure 39: Frequency resolved optical gating (FROG) trace (left) and integrated autocorrelation (AC, right) of compressed NOPA pulses. The AC-FWHM of 13.1 fs corresponds to a pulse duration of 9.2 fs. Uncompressed residuals make up for 3% wings. The actual measured integrated autocorrelation is shown in blue and its Gauss fit in red.

(e) Calibration

Calibrating the frequency axis in 2D spectra is done in time domain by quantifying delays between the pulses in terms of the wedge stage position and defining a conversion coefficient between them [196]. The coefficient is converting the amount of glass introduced by the movement of individual stages into the actual time-delay between the pulses. To get rid of a misplacement of the peaks in the 2D spectrum and to obtain the required fs resolution of time steps the glass wedges are calibrated to an accuracy of 6 as. For this purpose a pinhole with an aperture ($d=10\mu\text{m}$) smaller than the beam diameters is placed between two pulses to create a collinear interference pattern. Fourier transforming a central frequency cut through the recorded oscillating interferogram and using the known oscillation period of the frequency gives the reciprocal number of stage steps needed to pass through one period of the recorded oscillation. This expression then translates wedge movement to actual pulse delay.

Proper time ordering of the pulses is calibrated by specifying points of zero delay in units of calibrated stage position between individual pulse pairs (k_1 and k_2 for t_1 ; k_2 and k_3 for t_2). It is determined by measuring their respective SHG signals in a BBO ($d= 10\mu\text{m}$) crystal and evaluating the fringe patterns as a function of delay by Fourier transforming into time-domain and extrapolating the resulting plot of delay versus stage position to zero. The stage position at zero delay is then set as time zero.

The k_3 -LO delay is determined in the same way as the time ordering but with pulses k_3 and LO. The measured value is recorded for phasing the ω_3 projected 2D spectrum to the corresponding pump probe.

The wavelength calibration of the spectrometer is set with an ORION mercury-argon stick lamp by assigning the Hg/Ar spectral lines to individual CCD pixels and interpolating them with a linear fit.

(f) Set-Up

Our multifunctional set-up is capable of acquiring two-dimensional electronic (2D-ES), pump-probe (PP) and transient grating (TG) data sets by picking appropriate wavevector geometries and accordingly modify the pulse orderings ^[197].

Excitation energies can be tuned with apertures located in front of the entrance to the set-up and are usually adjusted to give an energy of 10 nJ per pulse. The required k-vector architectures for the individual FWM experiments can be easily chosen by inserting beam blocks into the redundant paths.

The set-up consists of a 50/50 beamsplitter dividing a compressed NOPA pulse into two equal parts, one of them being delayed with respect to the other at a movable stage to control the t_2 -delay. The delayed replica are then focused into a diffractive optical element (DOE) by spherical mirror 1 (SM 1) ^[198]. The DOE is a 125 lines/mm fused silica transmission grating optimized for $\pm 1^{\text{st}}$ diffraction order. The delayed incoming beams are vertically split up by the grating and thereby give rise to two sets of phase-locked pulse pairs k_1/k_2 and k_3/LO . To maintain phase relations among the pulses they are further on all directed via the same optics. After the grating spherical mirror 2 (SM 2) collimates the beams and passes k_1 to k_3 through fused silica glass wedges ($d= 0.9$ mm, 2° angle) mounted on calibrated delay stages to introduce a t_1 and/or short t_2 time delay. Short t_2 intervals can be handled by mutually delaying k_2 and k_3 with the corresponding wedges while extended delays require prolonged retardation by the initial t_2 -delay stage. The local oscillator (LO) passes through a thin variable neutral density filter (NDF) which attenuates it to prevent impacts on the sample. The applied NDF consists of a x mm glass plate with a continuous dielectric surface layer. The LO precedes the pulse sequence by approximately 520 fs since it is traversing less material than the excitation beams. Although any material leads to introduction of chirp, distortions from optical elements affecting all pulses equally along the way to the sample position are precompensated in the compression. The different chirp of LO and excitation beams is kept minimal by using appropriate fused silica materials that introduce least chirp. The beams are then focused to a spot diameter of approximately 200 μm into the sample by SM 3. A homogenous excitation profile is achieved because the Rayleigh length is larger than the film thickness.

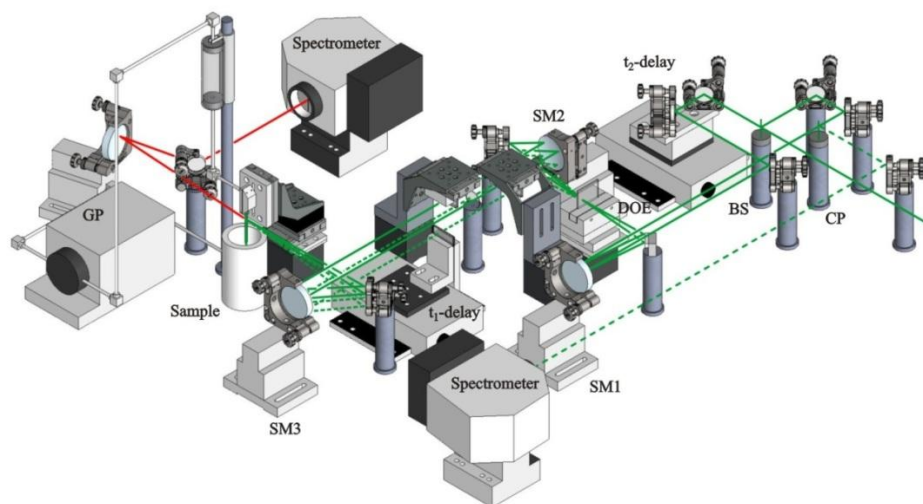


Figure 40: Multifunctional third order non-linear spectroscopy set-up in a folded boxcar geometry to trace ultrafast molecular dynamics. The design grants interferometric stability by generating phase locked pulse pairs in a diffractive transmission grating and guiding them along via the same optics. Individual delays in a pulse sequence are introduced by movable glass wedges and / or an additional up-stream t_2 delay stage while the k3-LO delay is set by a variable neutral density filter attenuating the LO ^[197].

The sample is circulated in a wire guided gravity driven flow jet ^[199] to avoid dispersions from cuvette windows and accumulation effects. A gear pump runs the sample in a cycle between an upper and a lower reservoir. By gravity the solution is flushed down a hooked 200 μm stainless steel wire that is clamped between two steel plates with an inlet pipe connected to the upper reservoir. The parabolic flow profile of the film allows for selection of the desired thickness by adjusting the jet position vertically in the beam focus. Collected sample in the lower reservoir is recycled by draining back into the circuit. An additional microflow pump can supply evaporated solvent at a desired rate on occasion. All connections are made from Teflon to resist organic solvents.

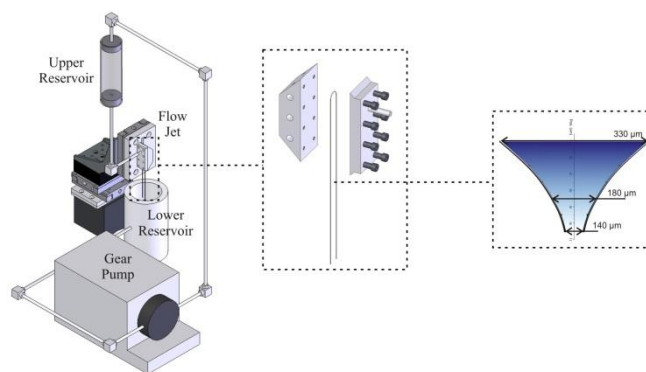


Figure 41: Schematic construction of the sample circulation with magnified wire guided flow jet and an inset showing the concentration gradient along the obtained biconcave flux profile.

The emitted non-linear polarization is spatially filtered by apertures to avoid stray light and depending on the applied four-wave mixing (FWM) technique either homodyne or heterodyne detected in its respective phase matching direction. Heterodyne detection refers to recording an interferogram of the signal with a known reference field (LO). The signal can be reconstructed from the interference pattern since the reference field and the delay between them is specified. Homodyne detection denotes recording the square of the irradiated signal field and accordingly loss of phase information.

An EHD camera with a sealed 2048 x 512 pixel CCD array in conjunction with a 1200 lines/mm grating of the spectrograph is employed to record signals in the frequency domain. Data acquisition is reduced by vertical binning of six pixels to a reading register to speed-up the camera's read-out time. Experimentally this is realized by smoothing potential wells of the defined amount of pixels and fencing them in larger one.

(g) Implementation of non-linear spectroscopies

2-Dimensional Electronic Spectroscopy (2D-ES)

2D-ES provides a versatile technique for studying coherences or couplings between individual molecular units as it allows to experimentally separate them from population contributions. Coupled systems manifest themselves by appearance of static and dynamic cross-peaks whose time evolution can elucidate the nature of the involved coherence (vibrational or electronic).

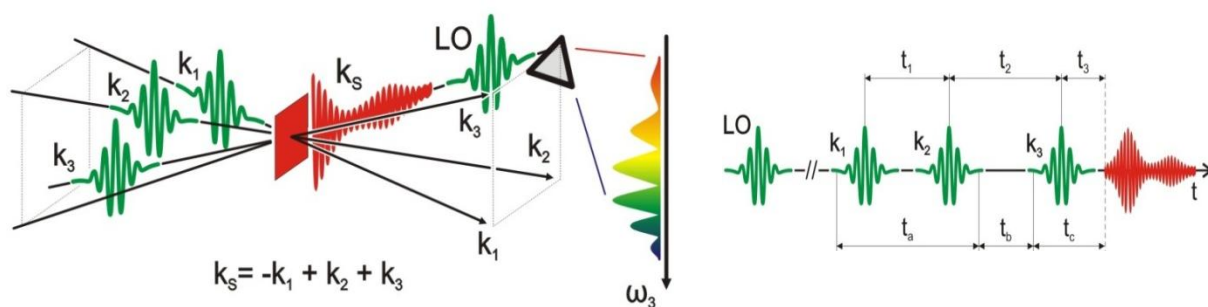


Figure 42: Schematic heterodyne detected two-dimensional electronic spectroscopy experiment (left) and time ordering of the pulses (right). 2D-ES correlates evolving coherences during time delays t_1 and t_3 for fixed population intervals. The LO preceding the induced polarization serves as a reference field to specify and reconstruct the signal's phase.

The experiment involves three equal pulses k_1 to k_3 arriving at the sample at different times [196, 200]. The t_1 delay between beams k_1 and k_2 is called coherence time because the system evolves in a coherent superposition of states generated by the first interaction from $-k_1$. The t_2 time delay is called waiting or population time. The latter expression is inspired by the fact that k_2 and

its induced dynamics are complex conjugate to $-k_1$ and thus leads to cancelation of phases in simple (two-level) systems thereby creating a stationary state or population. However in more complicated systems coherence and vibrational coherence pathways also contribute to the signal exceeding the simple picture. The third interaction from k_3 again restores a non-equilibrium state during t_3 that radiates the signal field. 2D spectra are obtained for fixed t_2 times by scanning the t_1 delay and heterodyne recording the corresponding t_3 emission by spectral interferometry [201, 202] with the local oscillator (LO).

In the above described set-up data are collected through reversing the time-ordering of the first two pulses giving rise to so-called rephasing and non-rephasing parts of the signal [89]. The interaction order $k_S = -k_1 + k_2 + k_3$ starting with a negative momentum kick from the initial pulse matches a rephasing signal for the molecular phase imprinted by $-k_1$ during the t_1 propagation period is reversed by $+k_3$ in the last (t_3) interval. The rephasing part is often called photon echo owing to the superradiant emission of merging phases of microscopic dipoles. The non-rephasing signal is obtained within the ordering $k_S = +k_1 - k_2 + k_3$ because the final phase is driven in the same direction as the first one indicating that microscopic dipoles are further spreading out. Both combinations are linearly-dependent and hence reversing the initial interaction order leads to emission of the counterpart in same phase matching direction. 2D-ES is a double FT spectroscopy correlating excitation (ω_1) and emission (ω_3) frequencies or rather time evolutions of coupled states during the intervals t_1 and t_3 in their spectral representation [83-85, 89]. To this end both delays t_1 and t_3 need to be scanned and transferred in the frequency domain. The polarization emitted during t_3 is implicitly recorded as ω_3 by time integrated spectrally resolved detection while t_1 needs to be explicitly FT with fine grid numerics. The coherence intervals to be related are separated by an intermediate waiting period (t_2) defining the temporal observation window. The constant t_3 -LO delay yields a modified heterodyned signal recorded as a function of ω_3 for every step of the t_1 scan. A 2D amplitude correlation chart is generated by numerical FT of individual t_1 delays to ω_1 slices and plotting them versus their respective ω_3 counterparts in a 2D array for a certain t_2 time. As the recorded interference pattern conserves phase information a retrieval algorithm is used afterwards to get rid of the reference field and reconstruct the phase of the 2D amplitude signal by projecting it onto the ω_3 axis and overlaying this map with the PP signal of the same t_2 .

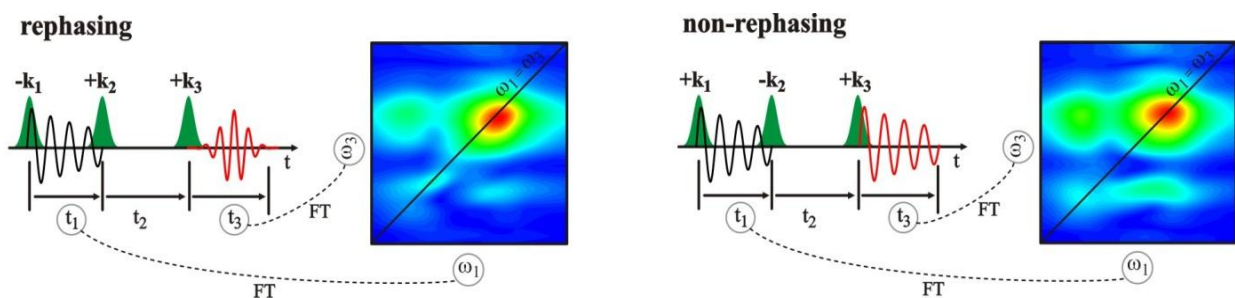


Figure 43: Illustration of rephasing (left) and non-rephasing (right) contributions of the non-linear polarization in 2D-ES. In the rephasing part the imprinted molecular phases during t_1 are reversed in t_3 while those of the non-rephasing part are further spread out.

Pump-Probe Spectroscopy (PP)

Pump-probe spectroscopy is a third-order technique although only two pulses are involved in creating the molecular polarization [97]. The pump beam being the first to interact with the sample causes two coherent perturbations while the second pulse probes the pump induced absorption changes. A spectral map of these population modifications over time yields a transient absorption spectrum reflecting the underlying molecular dynamics. The non-linear character of PP is highlighted in the phase matching condition of the emerging signal in figure x since two interactions from the pump and one from the probe are necessary to create a signal that is emitted in the same spatial direction as the probe. The produced polarization accounts for the observed probe alterations when summing up both fields. Because the probe beam acts like a reference field that is mixed with the signal at the detector PP is an inherently self-heterodyned technique and as such carries phase information.

Experimentally PP is implemented as an auxiliary measurement to retrieve the phase of the 2D spectrum by using k_1 as pump and k_2 as probe. The LO serves as a reference to normalize the probe beam for intensity fluctuations of the laser system and changes in the film properties. This arrangement is inspired by a likely trend of spatial chirp (originating from the DOE) along pulses k_1/k_3 and k_2/LO and accordingly a similar behavior of probe and reference with respect to experimental conditions. Scattering contributions are removed by dividing shuttered by bare probe spectra. A possible background is subtracted in advance of the measurement and fluorescence contributions can be removed by recording a spectrum at negative time delays. Contrary to good practice the probe beam cannot be attenuated before the sample spot due to the arrangement of the set-up. Since attenuation of the probe past the sample position leads to artifacts caused by different amounts of interspersed fluorescence in the two channels, the reference (or LO) intensity is equalized to the probe before the sample position by the NDF. The untreated probe is justified by an excitation probability of roughly 1 % of the molecules along the beam focus and a long recovering period in the circulating solution.

PP spectra at different population times are recorded at fixed t_2 delays by setting a certain threshold for the mean squared error between probe and reference and acquiring data until the changes in spectral signatures are on order of the noise level. A digitalized version of the spectrally resolved PP spectrum is stored for phasing.

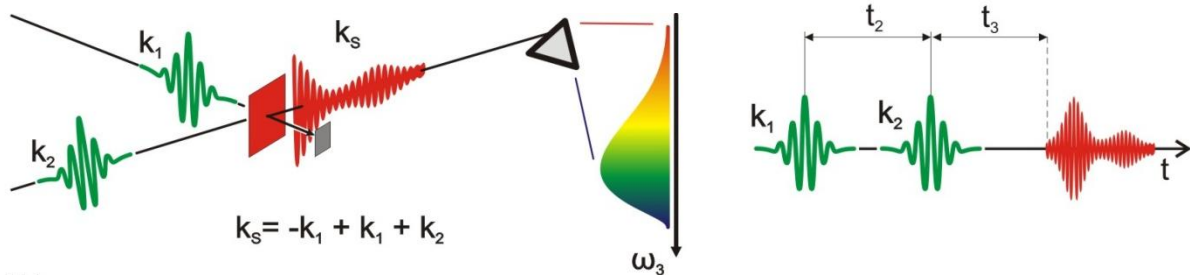


Figure 44: Scheme of auxiliary frequency resolved pump-probe experiment with its interaction sequence given by the phase matching condition for the emerging signal field (left side) and a time-ordering of the applied pulses (right). Spectra are recorded at fixed t_2 delays. The k_1 pump accounts for two interactions and the k_2 probe for one giving rise to a signal k_s in the probe direction that is self-heterodyned by the respective interference at the detector.

Dynamics over the full spectral range are investigated with a pump-supercontinuum probe technique by recording transient broadband spectra [203, 204].

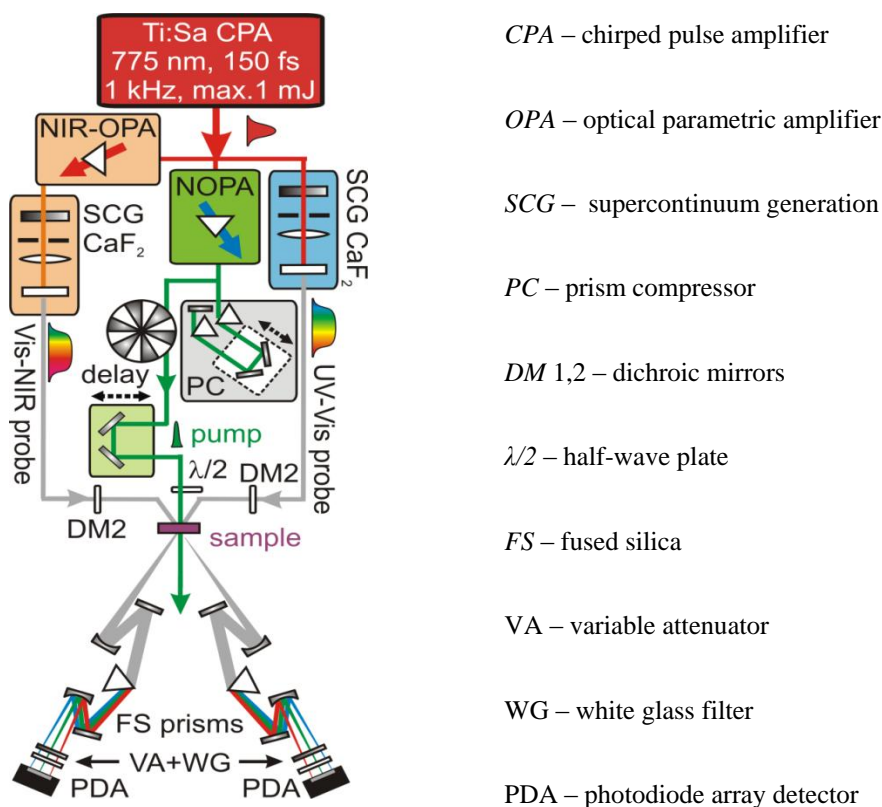


Figure 45: Broadband pump-probe set-up using a two-stage NOPA to generate VIS respectively UV pump, a NIR-OPA and two SCG stages one for UV/VIS and the second for generation of VIS/NIR probe pulses [204, 205]. A broadband prism polychromator together with a fast read-out multichannel PDA detection system allows to record absorption changes with mOD sensitivity on a sub-50 fs timescale.

A chirped pulse amplified titanium sapphire laser system (Ti:Sa CPA, Clark MXR) delivers 1 mJ pulses at 775 nm with 150 fs duration at 1 kHz [203]. A two-stage NOPA seeded with 200 mJ of Ti:Sa output provides pump tuning in the VIS or through subsequent frequency doubling in the UV. Below the μ J pump output is trimmed to sub-20 fs in an adjustable prism compressor (PC), chopped at 500 Hz and delayed with respect to the probe continuum. Preceding the sample position a combination of half-wave plate and wire grid polarizer is used to adjust the excitation energy and another $\lambda/2$ plate allows to set the polarization. Ultrabroad probe pulses are produced in supercontinua generation stages (SCG) comprising circularly translated CaF₂ crystals (d=5 mm) pumped by 1 μ J of Ti:Sa fundamental. Direct use of the CPA Ti:Sa leads to UV/VIS spanning emission (290-720 nm) while an input from a NIR-OPA gives a NIR/VIS detection window [204]. The resulting chirped white light supercontinua are not compressible to the Fourier limit due to their octave spanning bandwidth but can be used as obtained owing to their stable operation. A movable flow cell with 200 μ m cuvette windows and adjustable Teflon spacers is housing the sample. The cross-correlation measurement between pump-and probe in pure benzonitrile yielded a time resolution 50 fs. Temporal overlap between pump and probe is evaluated by correcting for the white light chirp since time zero is wavelength dependent in a temporally inhomogeneous pulse. The correction involves approximating the center of the coherent artifact in the solvent response with a polynomial fit and compensating for it. Detection of the broadband pulses takes place by dispersing them with a fused-silica prism polychromator, attenuating with ND and long-pass WG filter and detecting at 1 kHz read-out rate with a multichannel photo diode array (PDA) [203]. A prism polychromator as dispersing element is necessary to cover the whole exploited spectral range and to improve the UV energy resolution. A 512 pixel PDA sensor offers low electronic noise and good detection efficiency over a wide dynamic range. The detector is calibrated by assigning individual transmission patterns of a filter wheel equipped with known attenuation profiles in different spectral regions to the detector pixels.

Transient Grating Spectroscopy (TG)

Transient grating spectroscopy is a useful technique to quickly screen for oscillations with high sensitivity since it is a background free and homodyne detected technique.

Experimentally the initial two pulses (k_1 and k_2) hit the sample at the same time ($t_1=0$) at an angle θ and their interference creates a periodically modulated intensity pattern with a period given by the wavelength and incident angle of the beams. The resulting field gradient between extrema of the intensity grating forces polarizable molecules to align and gives rise to a periodically modulated density distribution [206]. Areas of high density exhibit a high refractive

index while those of low density influence the beam propagation less clearly. This induced material grating then scatters-off part of the last light pulse (k_3) at the Bragg angle which is equivalent to the polarization generated in its phase matching direction [207]. The order of interactions indicates that population and wavepacket dynamics in the ground and excited state are contributing to the detected signal. The diffracted probe pulse or rather irradiated polarization is then homodyne detected for different t_2 -times. This involves collecting the directional and therefore background free signal squared by excluding interference effects with a reference field. Its homodyne detection not only accounts for increased sensitivity but also for loss of phase information and a narrower spectral range. The absolute value of the recorded TG signal implies a real (absorptive) and an imaginary (dispersive) part. A plot of the polarization as a function of t_2 time can then be used to select suitable time-points for 2D measurements.

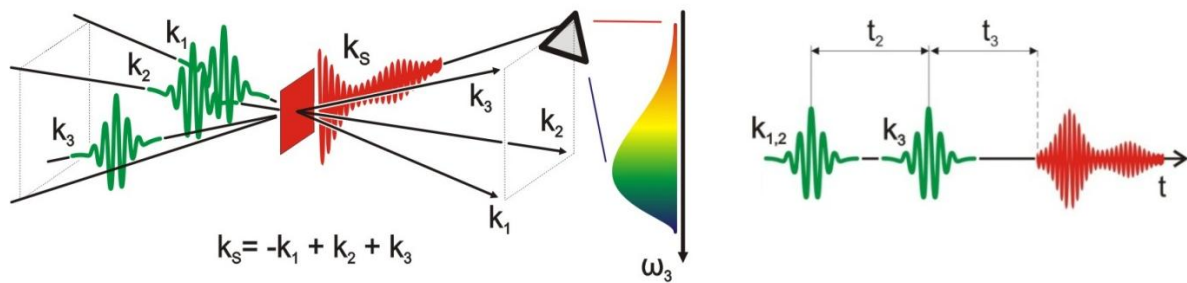


Figure 46: Scheme of implemented frequency resolved transient grating experiment (left) and time ordering of the pulses (right). Beams k_1 and k_2 arrive at the same time ($t_1=0$) at an angle inducing a material grating in the sample that is probed by k_3 for various t_2 times. The non-linear polarization k_s (or alternatively a scattered k_3 component) emerging after the last interaction is irradiated in a different direction than the k_3 probe beam and homodyne detected.

(h) Data processing

The collected signals are processed in two steps [197]. The first involves reconstruction of the recorded signal field while the second is used to retrieve the phase of the 2D plot.

Extraction of the polarization from the interferogram and specification of its phase and delay is achieved by taking apart the heterodyned signal and counting out the reference contributions [197]. Inverse Fourier transforming the heterodyned signal with respect to ω_3 yields three peaks (complex quantities) in terms of the detection time centered at zero and \pm the delay between signal and LO ($t_{\text{sig-LO}}$). The zero delay component corresponds to the envelope (amplitude) of the interferogram, while the shifted peaks arise from carrier frequency oscillations (\cos) and can be used to evaluate the signal-LO delay. The positively delayed temporal sideband is selected with a filter window and treated onwards since the experimental delay is positive whereas the unmeaningful negative (or complex conjugate) component arising from time-reversal symmetry of Fourier transformation (FT) is neglected. Back FT the positive sideband with respect to t_3 and dividing out the LO amplitude results in a complex number of the polarization represented as spectral amplitude times a phase factor. The signal phase as a function of ω_3 is wrapped up and approximated by the t_3 -LO delay. Subtraction of the t_3 -LO delay and combining the spectral phase with its amplitude gives the reconstructed frequency domain signal field plus a phase contribution from the LO that is divided out later on in the phasing procedure to PP. Neglecting the frequency dependence of the refractive index and reordering constants gives a field that is proportional to the molecular polarization. The 2D amplitude correlation chart is generated by numerically FT individual t_1 delays to ω_1 slices and plotting them versus their respective ω_3 counterparts in a 2D array.

Determination of the absolute phase of the 2D amplitude spectrum is done by relating the real part projection of the 2D amplitude spectrum onto ω_3 to its respective PP signal measured at the same t_2 time as justified by the projection slice theorem [89]. The real part is used since it comprises absorptive signal contributions only just as the changes recorded in PP. Projecting the real part onto the ω_3 (emission) axis is equal to sum up all ω_1 amplitudes and thereby setting the t_1 delay to zero in its spectral representation. Since PP the t_1 and k_3 -LO delays in PP are per definition zero and ω_3 in the 2D spectrum corresponds to the emission axis this projection resembles the PP signal at the same t_2 time. An optimal overlap of the ω_3 real part 2D projection with the respective pump probe spectrum is granted by varying an overall constant phase adjustment term and a timing correction factor [197].

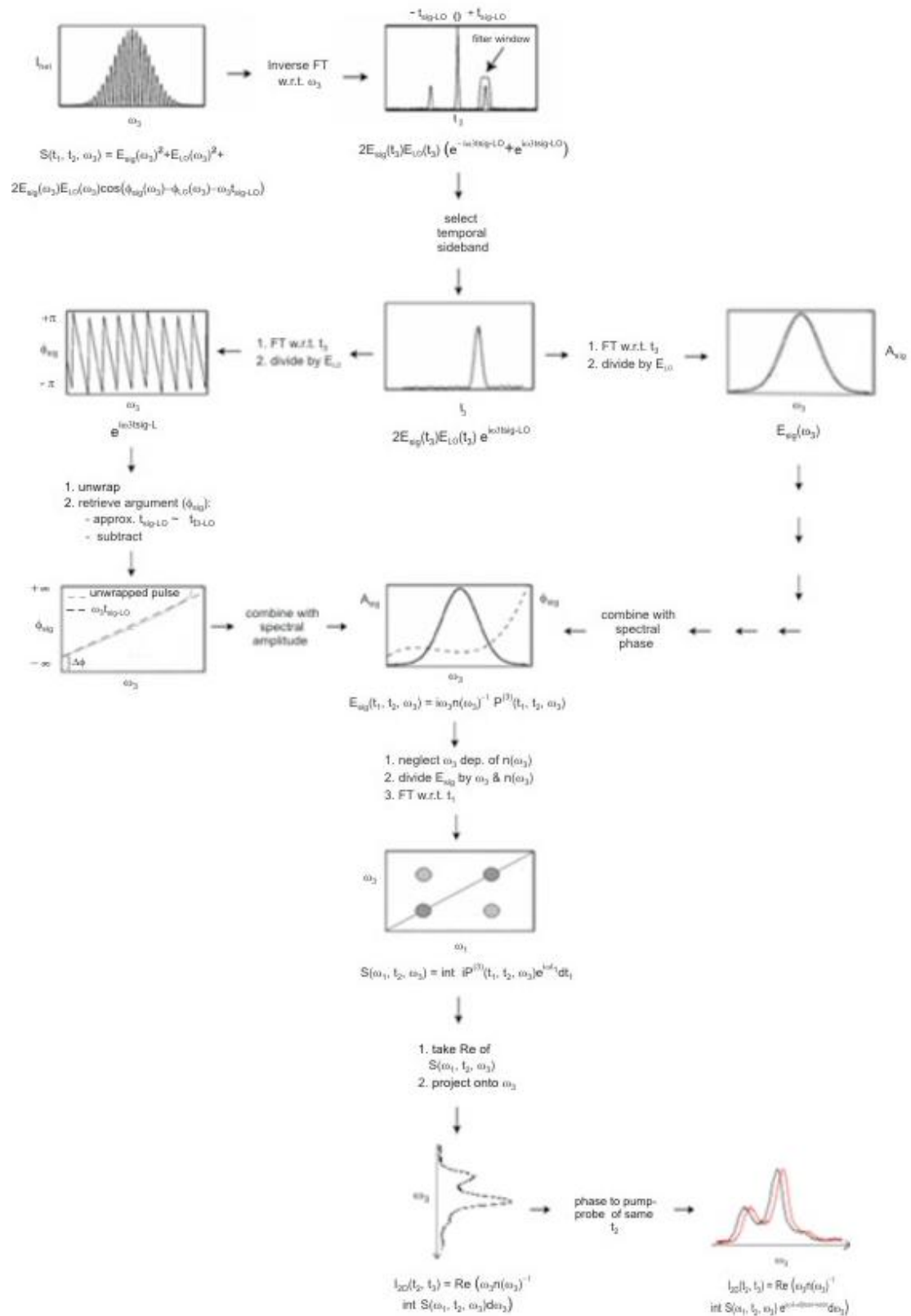


Figure 47: Inversion routine for obtaining the recorded signal field, restoring the corresponding 2D spectrum and phasing its absorptive part by projecting it onto the ω_3 axis and overlaying the plot with the respective pump-probe data.

6. Results Ultrafast Spectroscopy

(a) Pump-Probe spectroscopy

Pump-broadband Probe

The central PP trace resembles a plot of wavelength on the horizontal (or x-) versus population time on the vertical (y-) axis. The recorded intensities are given in terms of signal changes by the color scheme on the z-axis where blue areas indicate negative absorptive signal contributions (GSB and SE) and red ones correspond to positive portions (ESA). The upper chart shows transient absorption spectra along horizontal slices of the PP trace for population times selectable by the dashed cursor. Its magnitude at that time is given by the absorption change in 10^{-3} units (ΔmOD). The plot on the right shows time evolutions of single wavelength components based on their absorption changes selected by the vertical, dotted cursor.

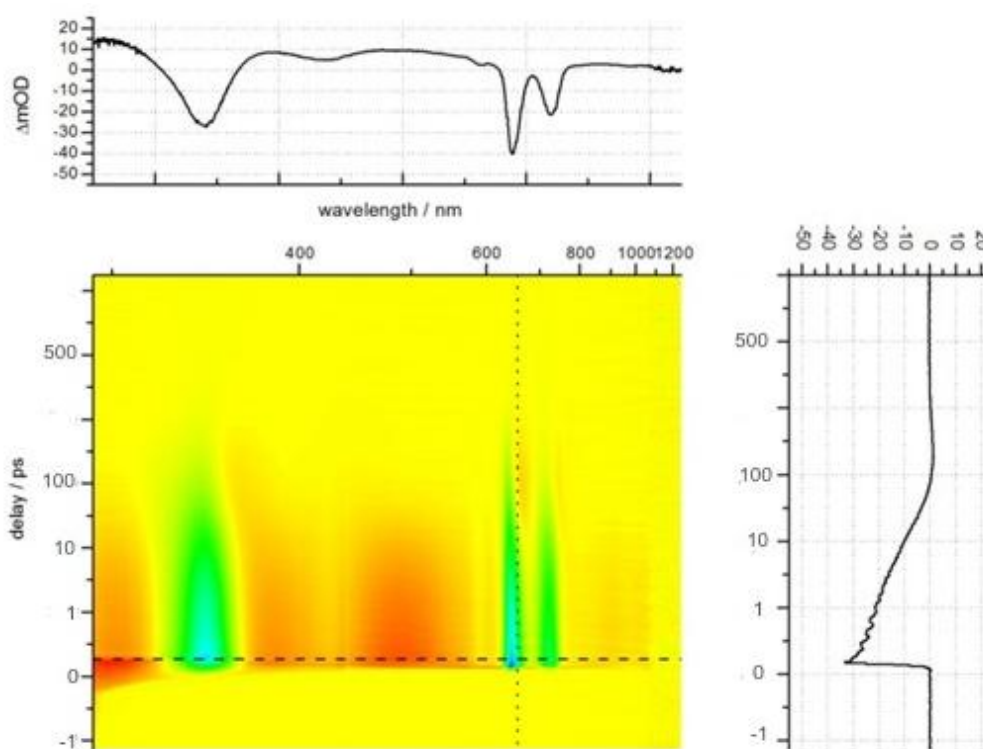


Figure 48: Magic angle polarization PP trace of lutetium bisphthalocyanine excited at 620 nm for population times up to 700 ps. Supercontinuum white light probing enables to detect spectral changes from the UV to the NIR. The color scaling indicates negative GSB and SE contributions in blue and positive ESA in red. Plots on top and to the right of the trace represent time and wavelength component slices at the current horizontal and vertical cursor positions respectively.

Probing from 300 nm (33333 cm^{-1}) to 1250 nm (8000 cm^{-1}) reveals all three main bands seen in the linear absorption spectrum as well as ESA in the UV, VIS and NIR regions. The main peaks B^{EX} , Q^{EX} and Q^{CT} appear as dominant GSB at 333 nm (30030 cm^{-1}), 618 nm (16180 cm^{-1}) and 702 nm (14245 cm^{-1}). Weaker bands like B^{CT} and Q^{vib} are mostly overlaid by ESA, but can be identified as less positive stripes in the time trace centered at 413 nm (24215 cm^{-1}) and 564 nm (17730 cm^{-1}). Very weak spectral features like the linear absorption peak at 498 nm (20080 cm^{-1}) and NIR bands at 785 nm (12738 cm^{-1}) and 950 nm (10526 cm^{-1}) are only seen in the corresponding decay profiles.

First sight conspicuities in diverse spectral regions of the time trace are oscillations with a vibrational period of 210 fs. A more detailed analysis of the oscillation periods show that all of them are corresponding to a 160 cm^{-1} mode which is attributed to a ground-state Lu- N_{iso} vibration. These vibrations are found at different intensities in ESA regions with underlying GSB contributions at 440 to 470 nm (24215 to 21275 cm^{-1}) (red edge of B^{CT} / strong) and at 560 to 570 nm (17857 to 17543 cm^{-1}) (Q^{vib} / weak) as well as in pure GSB areas from 595 to 735 nm (16805 to 13605 cm^{-1}) (Q^{EX} to Q^{CT} -bands / strong).

Table 12: Bands observed in the broadband spectrum and regions with 160 cm^{-1} oscillations.

<i>bands</i>	λ / nm	ν / cm^{-1}	<i>regions / nm with 160 cm⁻¹ osc.</i>
NIR 1	950	10526	595 – 735 (strong)
NIR 2	785	12738	
Q^{CT}	702	14245	
Q^{EX}	618	16180	560 – 570 (weak)
Q^{vib}	564	17730	
	498	20080	440 – 470 (strong)
B^{CT}	413	24215	
B^{EX}	333	30030	

Since frequencies and phases of the observed oscillations are virtually all the same they are attributed to a single wavepacket. Identical dephasing times are also pointing to the same surface as origin. Differences in vibrational amplitudes might emanate from different amounts of ESA in the various spectral regions or are due to unequal Huang-Rhys factors of the states.

PP in the Q-region exhibits characteristic modulations of the Q^{EX} and Q^{CT} bands with time. The pattern comprise an anti-correlated (or out-of phase) spectral motion between the red (blue) edge of the high (low) energy band and the red (blue) side of the low (high) energy band [82]. A correlated (or in-phase) modulation is seen between the red edge of the high energy peak and the blue edge of the low energy band. Strongest oscillations are seen in the region between the Q-bands from 630-690 nm.

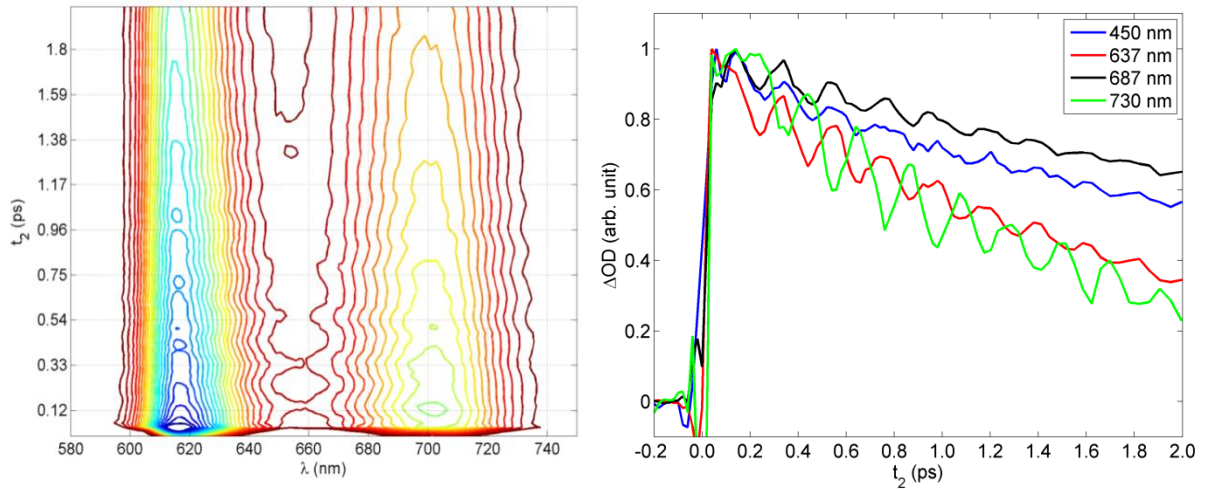


Figure 49: PP in the Q-band region showing the modulation patterns among the edges of EX and CT bands (left side). The selected time profiles (right side) are highlighting the in-phase (red, black) and out-of phase (black, green) spectral motions. The same mode is present near the B^{CT} transition at 450 nm (blue) and overlaid to establish their common origin.

The anti-correlated spectral movement was taken as an indication of a change in the mixing of CT and EX bands [208] mediated by a low frequency vibrational mode that modulates the interring distance. Such a modification will reciprocally alter the relative state admixtures by increasing the excitonic energy as the rings move together owing to enhanced exciton coupling and simultaneously decreasing the charge-transfer energy due to the smaller charge separation. In this way the transient absorption signal acquires a nuclear coordinate dependence, or in other words, arouses a non-Condon effect [82].

Varying the excitation in the Q-region yielded essentially identical dynamics and transient spectra without clear-cut dissimilarities for both pump wavelengths in magic angle (m-) polarization. The observed signals showed parallel decay profiles outside pulse overlap besides unequal signal strengths caused by differing pump energies. In each case the relative Q-band ratios were constant. The pump wavelength independency indicates either a ground- state wavepacket or coherence maintenance during electronic relaxation between the excited states [82]. Such a phase pattern indifferent of the excitation testifies equal Q-band affection that could be caused by the former two mechanisms.

The extension of the probing bandwidth does not allow to definitely assign the wavepacket to the ground or the dark excited state since both of them can account for the oscillations seen in GSB and ESA. The exact positions of ESA signals needed to clarify the situation are unfortunately unknown due to the lack of reliable quantum chemical calculations. Furthermore neither the observed pump wavelength independency of the Q-bands nor the fact that GSB oscillations are way stronger than those in ESA favor a certain state as the origin of the wavepacket. The first observation is caused by a fast relaxation between the states revealed by 2D-ES while different Huang-Rhys factors for ground and excited state transitions might explain the unequal amplitudes.

Albeit an excited state wavepacket cannot be excluded the more likely scenario is a common change in ground state density. It is reasoned by the requirements that a wavepacket in the excited state invokes to maintain coherence during two relaxation [82] steps from the exciton to the dark Q-state and moreover requires to exhibit appropriate characteristics of the doubly-excited manifold. A third option depicting the wavepacket in the CT state can be excluded by virtue of the state's lifetime that was measured with 2D-ES. Such a wavepacket would relax to the dark state within one vibrational period and hence cannot give rise to the timeframe of observed oscillations.

Even though the oscillation could not be localized both possible cases restrict the excited state topology to oppositely displaced potential curves along the vibrational coordinate [82] in the Franck-Condon region in order to be able to explain the observed correlations.

Another striking observation based on broadband probing concerns the time evolutions of B- and Q-bands that seem to be interrelated past 100 fs via similar bleaching patterns in both regions although only Q^{EX} was excited. Such correlated dynamics suggest a common source for Q and B transitions since joint loss of population seen by the probe can be accounted for by likewise depletion of a common ground state through Q^{EX} excitation.

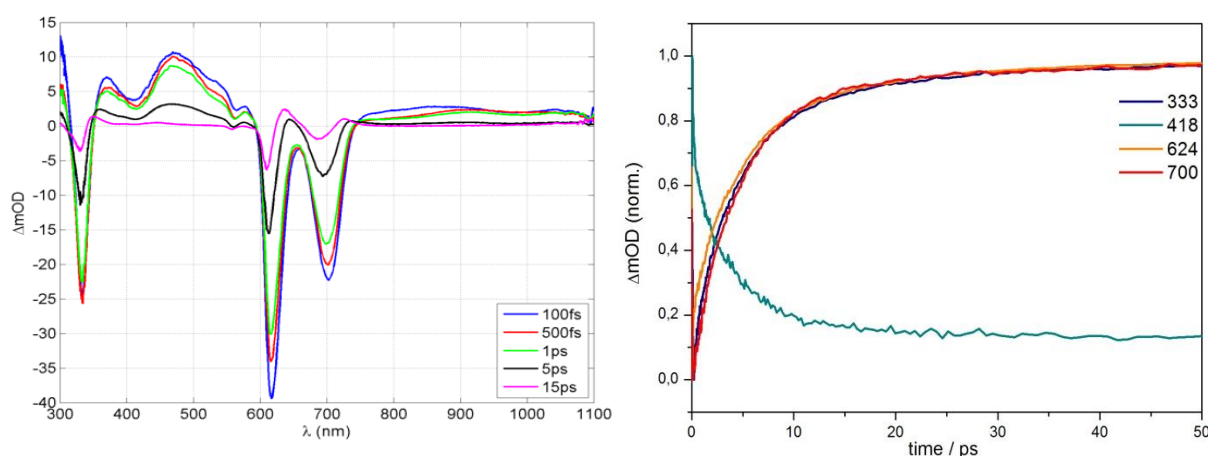


Figure 50: Transient absorption spectra after Q^{EX} excitation for selected population times and normalized bleaching pattern of single wavelength fits in the Q- and B-regions as a function of time (right).

This perception contrasts previously published calculations [78-80, 209, 210] in which transitions giving rise to Q- and B-bands are originating from different levels. Common oscillations observed in Q^{EX} , Q^{CT} and near the B^{CT} region further support the idea of transitions from a collective ground state. The lack of oscillation in the B^{EX} band can be explained by the Franck-Condon factors that only allow for a zero-phonon transition in this region.

Global fitting of the PP trace gave decay associated spectra (DADS) [211] originating from three exponential components with respective lifetimes 3.8 ps, 15.8 ps and < 1 ns plus one 160 cm^{-1} oscillation. For each component correlated bandshift pattern are found in Q- and B-regions. The second (15.8 ps) and third (1 ns) components show dispersive spectra indicating interference of negative and a shifted positive contribution. Their band displacements are more pronounced and in opposite direction as compared with the 3.8 ps component. The increasing amounts of intermixed positive contributions are thought to arise from HGS-ESA growing in as the ground state population recovers.

ESA at 770-840 nm shows an additional fast component. The single wavelength fit at 800 nm with a 40 fs response function yields an 180 fs component that is assigned to the delayed rise of SE. The SE is strongly red shifted which is typical for CT states. We estimate the strength of this component to be 2 mOD, or 10% of the GSB signal.

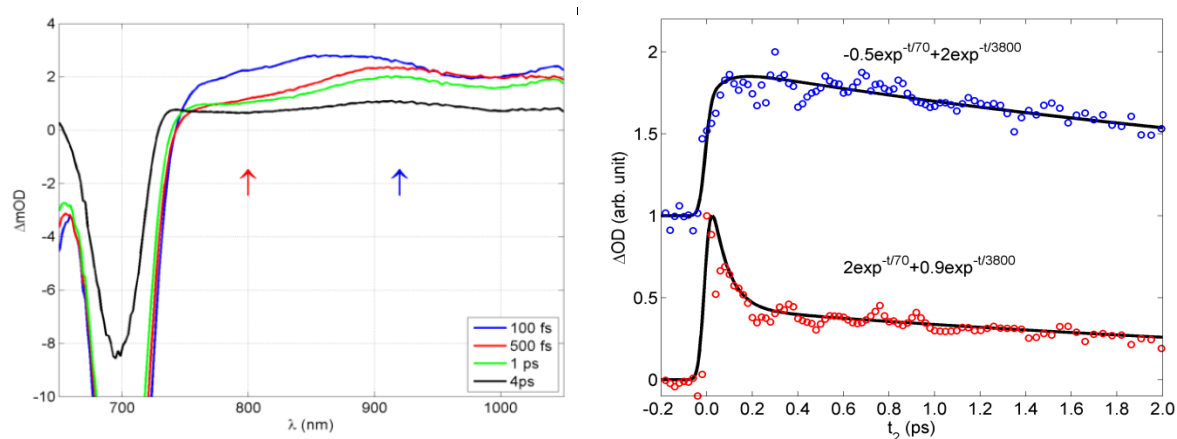


Figure 51: Time profile of the NIR region (left) with arrows indicating the positions of single wavelength fits (right) at 800 nm (red) and 920 nm (blue). Both exponentials display the observed oscillations in this region while only the 800 nm fit yields an additional fast decay component attributed to a delayed rise of SE.

The species associated spectra (SAS) [211], obtained assuming a sequential model without branching, yield components of the second and third state which are very similar to the ground

state absorption spectrum. Their resemblance in band shapes and slightly red shifted absorption suggest hot ground state (HGS) components as source of the 15.8 and inf species. The amplitude variations among their Q- and B-regions are probably an artifact related to merging the spectra and normalizing them to their respective Q-maxima. The 3.8 ps component spectrum exhibits an upside down absorption pattern to the other two species with maximal contributions in the B^{CT} and its adjacent ESA region around 480 nm as well as between the two Q-bands. The absorptive structure of the 3.8 ps SAS component cannot be associated with the (common) ground state. When concerning its absorptive structure in the NIR, its lifetime and the fact of missing fluorescence from Q^{CT}, the 3.8 ps species appears to be a dark state accepting the excited state population. This dark state then relaxes the excited state population within 3.8 ps to a hot ground state.

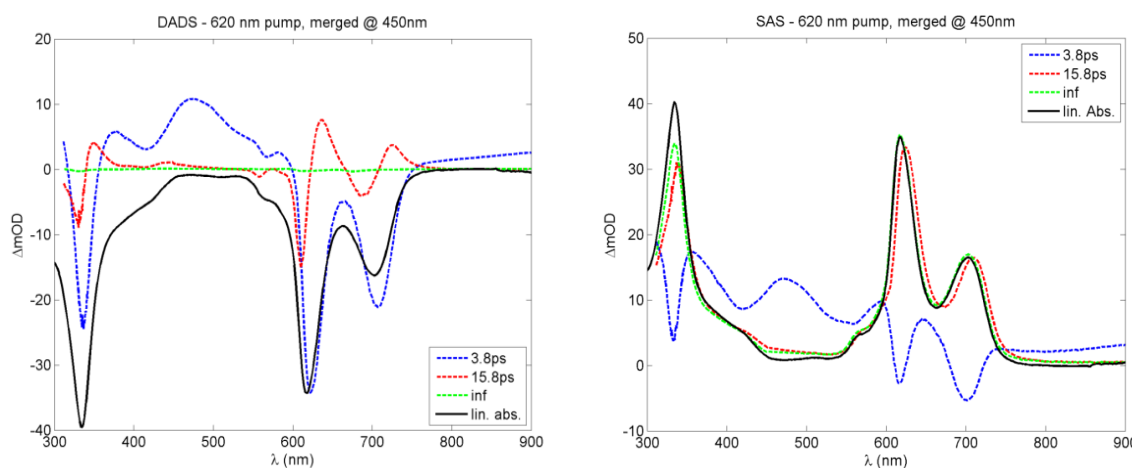


Figure 52: Global fit over the recorded spectral range yielding decay associated spectra (DADS) with three exponential components called by their respective lifetimes 3.8 ps, 15.8 ps and inf with a ns lifetime (left). The species associated spectra of the same components are shown on the right.

Frequency resolved transient grating (FRTG)

Two strong modes can be resolved in the FRTG in the region between the two Q-bands. The low frequency mode at 160 cm^{-1} was already known from pump-probe experiments. A second intense feature with a 700 cm^{-1} frequency shows up on the low energy side of the exciton band. The 700 cm^{-1} oscillation is only present in this spectral region as contrasted to the 160 cm^{-1} mode.

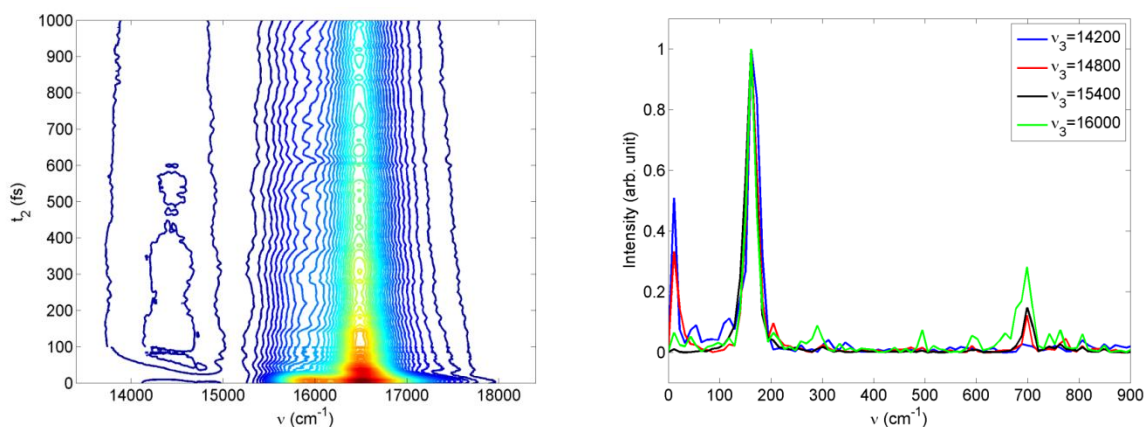


Figure 53: Frequency resolved transient grating trace of the Q-band region (left) and associated frequencies obtained by Fourier transforming the indicated time slices. The intensities have been normalized to the amplitude of the 160 cm^{-1} mode.

As higher energy excitation promotes the high frequency vibration, a possible implication in population transfer from the exciton to the charge transfer state arises naturally.

The oscillation periods, frequencies and phases extracted from FRTG match PP data well.

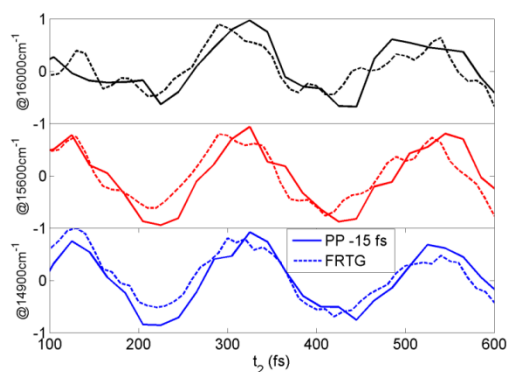


Figure 54: Oscillation characteristics of the modulation for three frequencies in the Q-band region as obtained from 10fs PP (straight line) and FRTG (dotted line).

(b) 2-D electronic spectroscopy

The presented 2D plots show phased amplitude spectra where positive contributions indicated in red give GSB and SE, while negative contributions in blue are related to ESA. The color scale is opposite to that in the broadband PP. The diagonal is reversed and highlighted as a blue line connecting the edges of the plot from the lower left to upper right. Contour lines reflect the intensity distribution of the peaks which have been normalized to their respective PP values and are plotted in 5 % steps. Peaks on the diagonal, located at $\omega_1 = \omega_3$, correspond to populations of the individual states, whereas off-diagonal elements at $\omega_1 \neq \omega_3$ are representing couplings between them. The upper diagonal peak at 16200 cm^{-1} corresponds to the exciton state and the lower diagonal peak at 14200 cm^{-1} to the charge-transfer state.

In the case of lutetium bisphthalocyanine the period exhibiting reversible dynamics prior to the onset of relaxation is so short that it is fully covered by pulse overlap. Pulse overlap refers to the initial time period up to 15 fs where additional pathways are contributing to the 2D signal. These pathways arise since each pulse in the sequence contributes with any possible linear combination, that is $\pm k_i$, in the concerned phase matching direction. Inconsistencies and uncommon features around time zero may originate from these additional signal contributions.

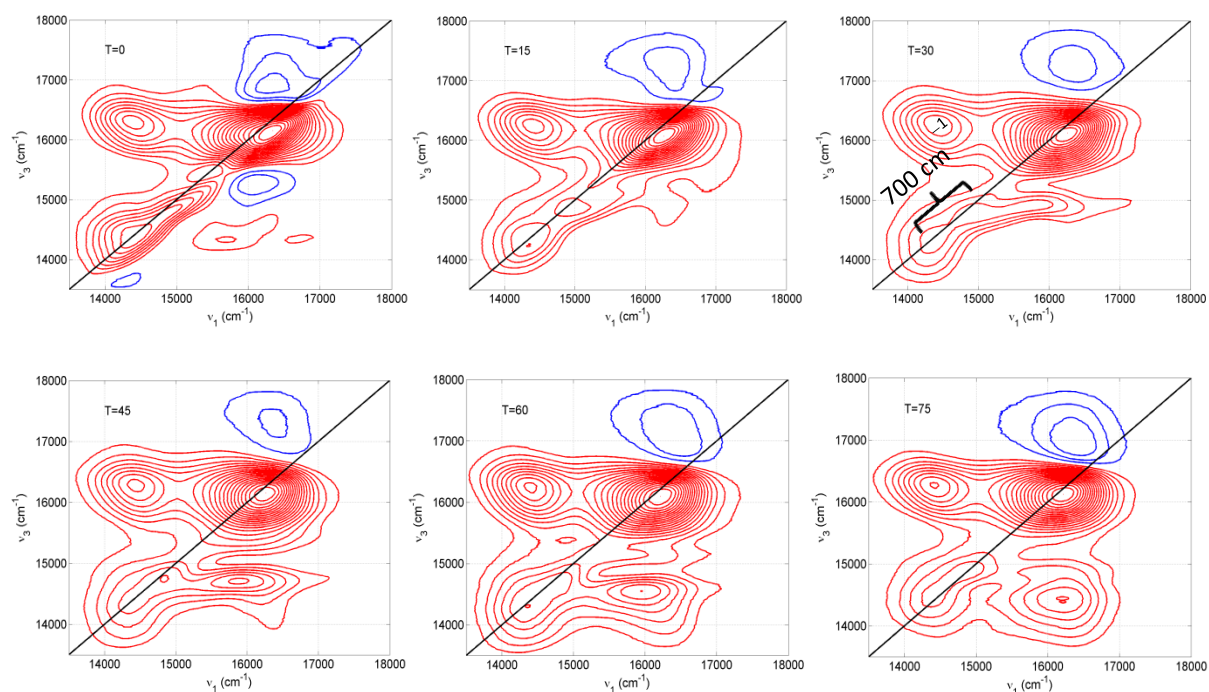


Figure 55: Phased 2D electronic spectra of lutetium bisphthalocyanine for early population times indicated by T in the upper left corner. Spectra are plotted with 2.5 % contour lines. Positive features are given in red and negative ones in blue.

The 2D correlation spectrum exhibits an unusual shape in both regimes lacking the characteristic square pattern of coupled transitions. Such a behavior is rather uncommon insofar as cross-peaks constitute mixtures of both diagonal peaks and should therefore appear with equal intensity and show similar dynamics.

The recovery of the absent lower cross-peak in the course of time is asymmetric with respect to the ω_3 -axis. In the initial pulse overlap region the outermost contour lines in the upper part of the ω_3 -axis are distorted differently but become stabilized in the following evolution. ESA on top of the upper diagonal peak seems to shift its center frequency down and cause an anti-diagonal elongation on early time-scales. The lower diagonal peak is elongated along the diagonal and clearly exhibits an inhomogeneous lineshape. The slant of the upper cross-peak is influenced by the ESA contribution in between the lower diagonal and upper cross peak. At $t_2=0$ fs there are additional ESA features among the upper diagonal peak and missing lower cross peak.

At $t_2=15$ fs the FWHM of the pulses are just separated and at $t_2=30$ fs only their wings coincide. During these periods of fading pulse overlap a feature separated by 700 cm^{-1} from the low energy diagonal peak emerges. At 15 fs its amplitude develops on the diagonal and at 30 fs the coupling to the upper diagonal peak builds up.

Outside pulse overlap (onwards 15 fs), the low energy cross-peak is still absent although there is considerable relaxation from the upper diagonal to the 700 cm^{-1} feature seen from the streaking along ω_3 . The shape of the upper diagonal peak gets much rounder at this stage of evolution which is attributed to relaxation and the ceasing influence of chirp brought along with subsiding pulse intersection. The same explanation holds for the onset of the well behaved ESA lineshapes on top of the upper diagonal peak. An imbalance of pathways as well as phase-twisted lineshapes for early times could lead to the observed pattern.

At 45 fs the upper diagonal peak broadens and a square shape builds up in the area of the upper diagonal to the 700 cm^{-1} feature. The downward motion of the upper peak and its vertical elongation are signatures of relaxation and the build-up of Stokes shift.

A clear low energy cross-peak between the 700 cm^{-1} feature and the upper diagonal peak is seen at 60 fs indicating ultrafast population relaxation from the upper diagonal (exciton) state to the 700 cm^{-1} feature contained within the lower diagonal peak (charge transfer state). Its observed oscillation period corresponds to 48 fs which is within the range of fast decay from the exciton state. The time-scale and efficiency of this process suggests the participation of a conical intersection near the Franck-Condon region. The term conical intersection describes a crossing of two potential energy surfaces in the form of a funnel that acts like a connection between them and serves to dissipate energy non-radiatively on a fs time-scale. The emerged feature on the

diagonal can either be related to a high-frequency vibration in the CT potential curve that accepts the excess energy or corresponds to an intermediately populated fragment of the split Q-bands that is derived from the interaction with the counterion.

In case the 700 cm^{-1} feature would be a nuclear mode, its impact on early dynamics is expected to be significant as the high energy implies strong influence on electronic degrees of freedom or vibronic coupling. Anyhow, the mode driving the population through an intersection is usually dark and accessed from the Franck-Condon region via a bright mode which makes it unlikely that the 700 cm^{-1} feature directly causes the relaxation.

In turn, if the state would correspond to an additional electronic level, its direct observation can be taken as experimental evidence of the counterion influence and concomitant alteration of the electronic structure.

An accurate declaration of its nature requires detailed simulation of the 2D spectra.

Following the relaxation step to this intermediate state, the population continues to flow down to the lower diagonal peak but never recovers the expected intensity of the upper cross peak as seen from 2D spectra recorded for longer waiting times.

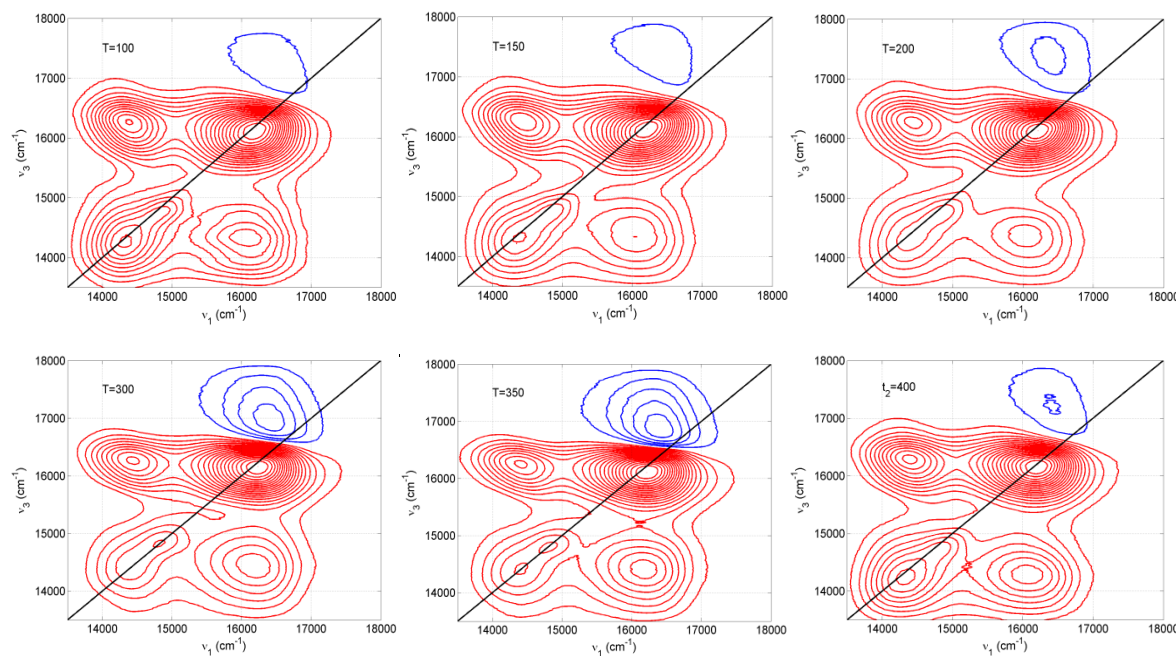


Figure 56: Phased 2D electronic spectra of lutetium bisphthalocyanine for longer population times.

The dynamics of the absent low energy cross-peak are explained by a time-dependent interplay of GSB, ESA and SE. The states are renamed in fig. x so that the ground state is named g , excited singlet states are denoted by e and doubly-excited singlet states are called f . Correspondingly EX

is now e_{EX} and CT is e_{CT} . The employed scenario involves a higher excited two-exciton state f whose ESA perfectly cancels the GSB contribution of the lower cross peak. To meet this condition the $e_{CT} - f$ transition needs to have the same energy as the $g - e_{EX}$ transition. The pathway is then contributing as long as the excited state f exists and is therefore observed for 2D spectra recorded at population times shorter than f 's lifetime. Given that the e_{EX} state decays within 30 fs this contribution will be dominant in the very beginning and only take part in the later evolution. As the initially counteracting ESA declines to state e_{CT} a correlated rise of positive SE to the ground state enhances the lower cross-peak during the lifetime of state e_{CT} . The SE pathway only partially restores the cross-peak signal by compensating for some of the remaining ESA. When state e_{CT} loses population to the dark NIR state underneath the positive SE disappears and no more rise in the lower cross-peak intensity is observed. Consequently its steady state amplitude then remains rather unchanged.

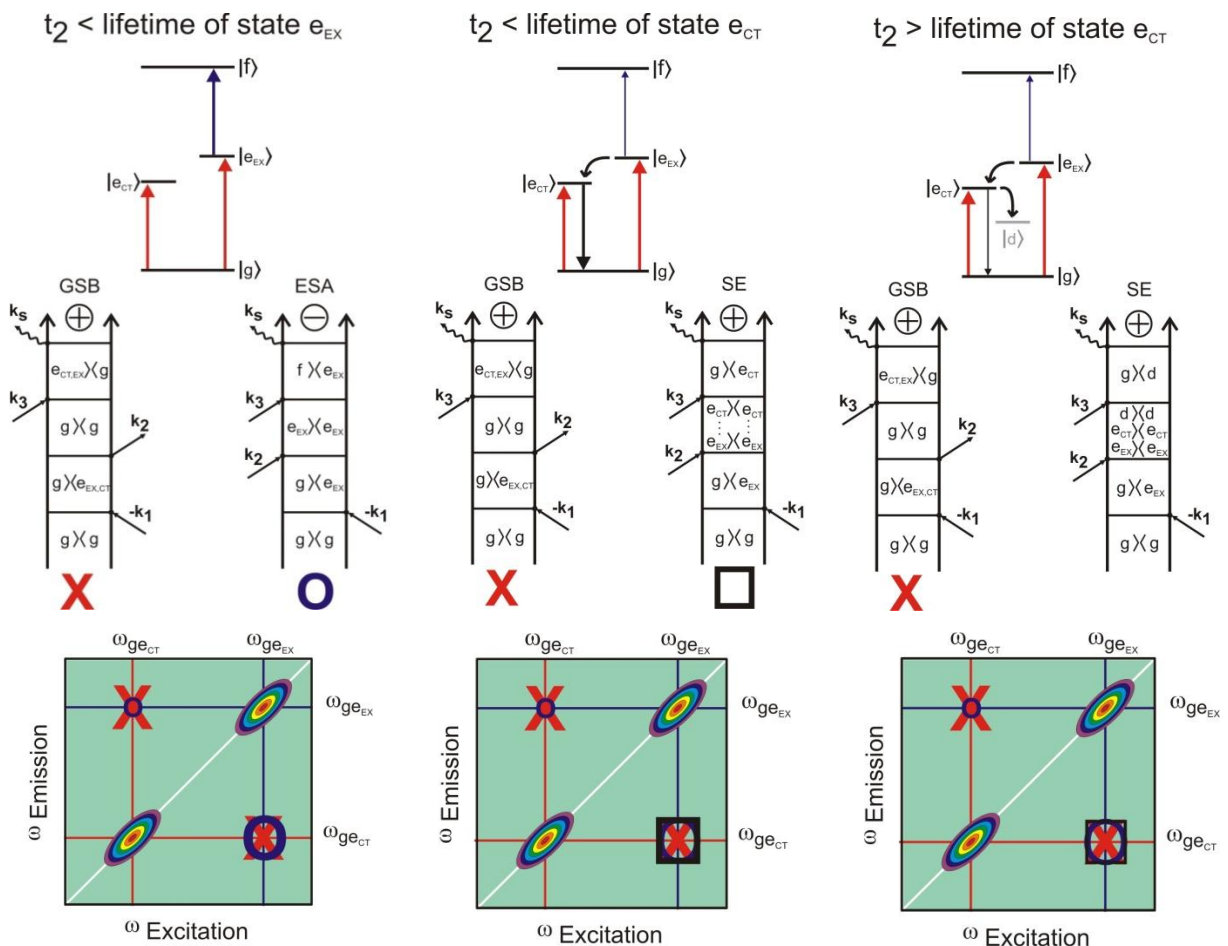


Figure 57: A sketch illustrating the interplay of several pathways which account for the absence of the lower cross peak. At short times an ESA pathway to a two-exciton state f is cancelling the lower cross peak, at intermediate times the SE contribution partially cancels ESA and restores some intensity that then remains rather constant due to relaxation of states 1 and 2.

The asymmetry of the recovery with respect to ω_3 can be either due to an energetically non-uniform decay of the ESA, that is relaxation from the Franck-Condon region causes a shift in transition energy or to discontinuous up-come from SE. Elucidating its exact nature will also require further simulation.

Kinetics are obtained from 2D spectra via renormalization of the data to PP. In this process the integral of the 2D projection is adjusted to the absolute value of the recorded PP spectrum.

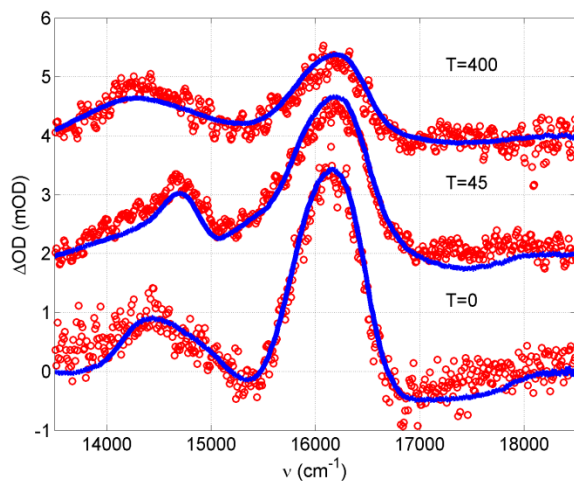
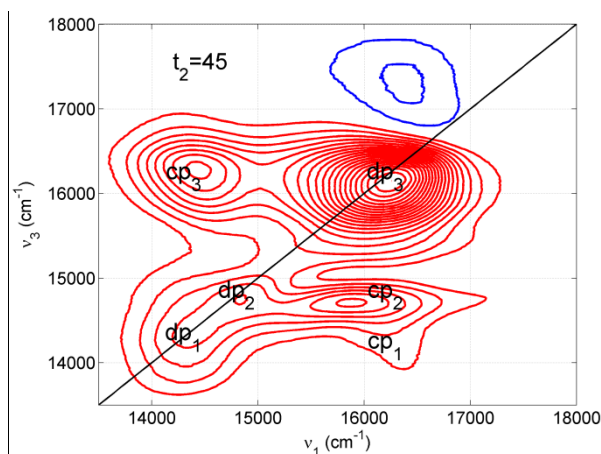


Figure 58: Phasing of the projected real part 2D spectrum (blue) to the recorded PP (red) in the investigated 5000 cm^{-1} area of the Q-band region. Kinetics from 2D spectra are obtained by adjusting the integral of the projection to the absolute value of the PP signal for each t_2 -time.

An enumeration of the 2D peaks and their corresponding kinetics are shown in the next graph.



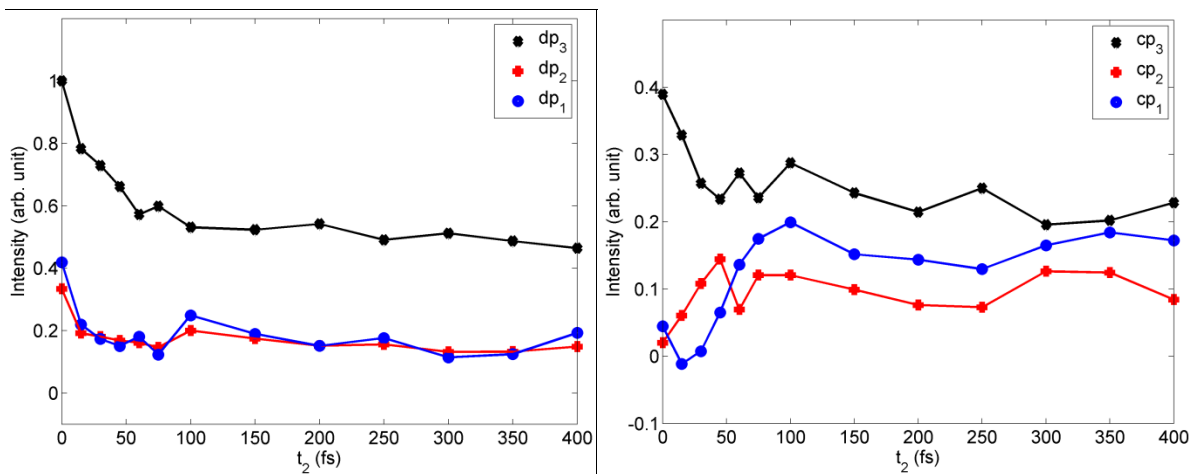


Figure 59: Enumeration of the various peaks (top panel) and their corresponding kinetics (lower panel) after normalization to their respective PP spectra. DP 1, 2, 3 kinetics are given on the left in blue, red and black respectively. CP kinetics are indicated by the same colour coding on the right.

DP3 exhibits a fast initial decay component and essentially shows GSB contributions afterwards. The data show a 42 % decay within 20 fs for Q^{EX}. This corresponds to the population decay to the dark state which then ends up in a hot ground state. The lack of observed oscillations from the 160 cm⁻¹ wavepacket after the fast decline in the GSB is probably related to the weak amplitude of the oscillation and fluctuations of the NOPA spectrum. DP2 and DP1 display less steep relaxation. Indications of the 160 cm⁻¹ oscillation are so weak as compared to those in the CPs that they might easily originate from changes in the NOPA spectra.

The CP dynamics are difficult to interpret since a couple of different pathways contribute to the signal (see theory part for a listing). The upper CP contains pulse overlap and coherence pathways in the beginning besides long lasting GSB. In the lower CP there are additional ESA and SE contributions involved. The coherent pathways are vanishing within approximately 5 fs as their lifetime makes up $\frac{1}{2}$ of the population relaxation time. Pulse overlap adds to the first 30 fs. Chirp effects cannot be further reduced since all of the applied bandwidth is needed and the pulses are compressed as good as possible. Interpretation of ESA / SE / GSB interplay with respect to the possibilities of non-uniform ESA decay and upcoming SE in the lower cross-peak dynamics requires onward modeling by simulation. Oscillatory patterns in the CPs can easily be attributed to the 160 cm⁻¹ wavepacket based on the GSB pathway evolving in the ground state during t₂. The sharp kink like structure around 50 fs is unlikely to be caused by the 700 cm⁻¹ mode because no vibrational coherence pathways are populated.

Lineshapes are evaluated via two methods [91-93, 212]. Slope analysis relies on observing the changes of the slant along the diagonal peak width. The evolution of lineshapes then reflects the

imbalance of rephasing and non-rephasing contributions. The ellipticity is defined as $E = \frac{a^2 - b^2}{a^2 + b^2}$ where a and b are diagonal and antidiagonal linewidths corresponding to inhomogeneous and homogeneous broadenings. Both methods are supposed to yield similar results, that is, they report on the relaxation of the correlation function or fluctuations of the environment. However a comparison showed that their equality only holds for long population times causing that lineshape analysis is trustworthy in this region. Since the ellipticity is directly proportional to the correlation function it was taken as measure for the initial evolution. Deviations among the analysis methods in the beginning are probably mainly caused by chirp and to a less extent by pulse overlap effects.

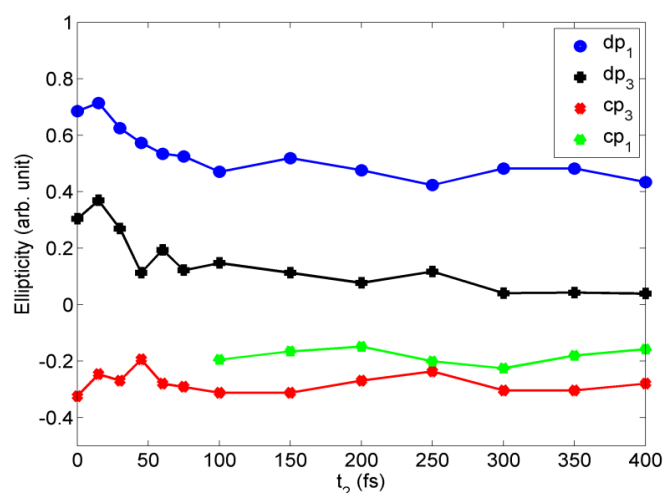


Figure 60: Ellipticity analysis results of the lineshapes. DP 1, 3 are shown in blue, black and CP 1, 3 in green, red.

DP1 and DP3 seem to oscillate out-of phase with a period that corresponds to the 160 cm^{-1} mode. This resembles the same anti-correlated oscillation pattern that was observed in PP. For DP3 the oscillation is weaker than for DP1, which is rationalized by admixing ESA contributions. CP1 and CP3 also exhibit similar oscillations, but CP1 is phase shifted. This shift might originate from chirp effects of the used pulses.

Summary

Ultrafast spectroscopy on lutetium bisphthalocyanine using 50 fs pump-broadband probe and subsequent analysis of transient spectra essentially reproduced the same Q-region dynamics as reported by Fleming. However the supercontinuum detection lead to the conclusions that a dark state in the NIR accepts population from the CT band within 200 fs and from there relaxes onward to the ground state. Furthermore the detection window allowed to resolve a coupling between the Q- and B-bands in the sense that both transitions originate from a common ground

state. This contrasts theory in which B- and Q-band transitions are derived from different levels. Oscillations corresponding to a 160 cm^{-1} mode are found in various spectral regions including GSB and ESA. The vibration could not be addressed to a particular state within 10 fs PP and 2D-ES experiments. Thereby the possible proposed models to explain the Q-band dynamics were settled to the one with oppositely displaced EX and CT potential curves.

Frequency resolved transient grating of the Q-region revealed the dominating 160 cm^{-1} mode and exposed an additional 700 cm^{-1} vibration on the low energy side of the exciton band.

10 fs PP and 2D-ES on the Q-region uncovered an ultrafast initial 42 % population decay from EX to the CT band. The 20 fs timescale and its efficiency point to the participation of a conical intersection near the Franck-Condon region. 2D-ES spectra initially exhibit an unusual shape lacking the low energy cross peak and likewise the characteristic square pattern of coupled transitions. The recovery of the absent lower cross-peak in the course of time is asymmetric with respect to the ω_3 -axis and reveals a feature 700 cm^{-1} above the CT band. It probably corresponds to a mode in the CT state accepting the excess energy of the EX band. The initial lack of the low energy cross peak is explained by an ESA transition to the two-exciton state that cancels the GSB in the beginning. An interplay of rises and decays of ESA, SE and GSB relaxation can account for the recovery dynamics. The asymmetric shape during the recovery along ω_3 requires further modeling to clarify its source.

The synergy of broadband pump-probe and 2D-ES data suggest the following excited state topology and level scheme with associated lifetimes.

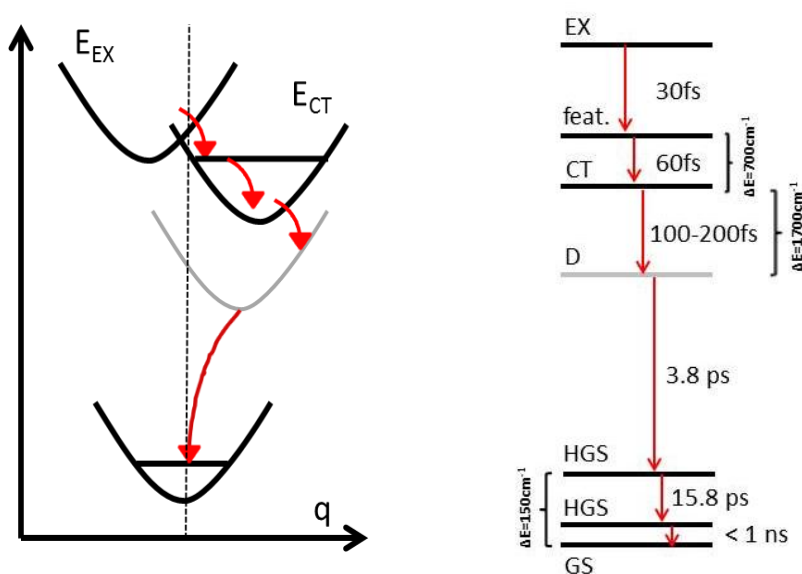


Figure 61: Proposed topology of the singly excited state manifold (right) and the corresponding level scheme with associated lifetimes (right) derived from the broadband pump-probe and 2D-ES experiments. EX denotes

the excited high energy singlet state that is mostly of exciton character, CT the lower energy singlet excited state of charge transfer character, D the dark state in the NIR and HGS a hot ground state (GS).

The influences of the vibrational modes on the dynamics of lutetium bisphthalocyanine are thought to be important during different times in the evolution. This argument is based on their distinct energetics. The 700 cm^{-1} mode is a high frequency vibration which is presumably dominant for the early dynamics from EX to CT while the low energy 160 cm^{-1} ground state vibration modulates the following vibronic coupling from CT to the dark state. In analogy to reaction centers these vibrations can be regarded as intramolecular high-frequency vibrations modulating the intrinsic monomer dynamics and intermolecular low-energy modes from the protein backbone altering the chromophores electronic properties.

Outlook

The hypothesis of a conical intersection in the Franck-Condon region is going to be further investigated in an upcoming experiment by variation of the solvent. A change in the solvent polarity most significantly affects the energetic position of the CT potential curve due to its larger dipole moment and is supposed to displace the conical intersection. This positional shift of the CI can then be used to explore the influence of the phase of the excitation on the funneling process, its efficiency and timescale.

2D-ES experiments with different polarizations can yield valuable additional information via enhancement of cross-peaks relative to diagonal ones or display excited state coherences only. In case the counterion lifts the degeneracy of the Q-bands, the resulting transitions should be polarized perpendicular to each other. These polarization measurements offer the possibility to assign the observed feature during relaxation and might expose additional features of the potential energy landscape.

Literature

- [1] Z. Ali-Adib, G.J. Clarkson, N.B. McKeown, et al., *J. Mater. Chem.*, 8 (1998) 2371-2378.
- [2] R. Bonnett, *Chem. Soc. Rev.*, 24 (1995) 19-33.
- [3] S.A. Borisenkova, *Pet. Chem.*, 31 (1991) 379-398.
- [4] C.G. Claessens, U. Hahn, T. Torres, *Chem. Rec.*, 8 (2008) 75-97.
- [5] M.J. Cook, M.F. Daniel, K.J. Harrison, et al., *J. Chem. Soc. Chem. Commun.*, (1987) 1148-1150.
- [6] G. de la Torre, C.G. Claessens, T. Torres, *Eur. J.Org. Chem.*, (2000) 2821-2830.
- [7] G. de la Torre, C.G. Claessens, T. Torres, *Chem. Commun.*, (2007) 2000-2015.
- [8] G. de la Torre, P. Vazquez, F. Agullo-Lopez, et al., *J. Mater. Chem.*, 8 (1998) 1671-1683.
- [9] M.R. Detty, S.L. Gibson, S.J. Wagner, *J. Med. Chem.*, 47 (2004) 3897-3915.
- [10] F. D'Souza, O. Ito, *Chem. Commun.*, (2009) 4913-4928.
- [11] M. Emmelius, G. Pawlowski, H.W. Vollmann, *Angew. Chem. Int. Ed. Engl.*, 28 (1989) 1445-1471.
- [12] D. Hohnholz, S. Steinbrecher, M. Hanack, *J. Mol. Struct.*, 521 (2000) 231-237.
- [13] S. Laschat, A. Baro, N. Steinke, et al., *Angew. Chem. Int. Ed.*, 46 (2007) 4832-4887.
- [14] K.Y. Law, *Chem. Rev.*, 93 (1993) 449-486.
- [15] A.B.P. Lever, M.R. Hempstead, C.C. Leznoff, et al., *Pure Appl. Chem.*, 58 (1986) 1467-1476.
- [16] J.Z. Li, D. Gryko, R.B. Dabke, et al., *J. Org. Chem.*, 65 (2000) 7379-7390.
- [17] M.A. Loi, P. Denk, H. Hoppe, et al., *J. Mater. Chem.*, 13 (2003) 700-704.
- [18] T.J. Marks, *Angew. Chem. Int. Ed. Engl.*, 29 (1990) 857-879.
- [19] McKeown N, *Phthalocyanine Materials: Synthesis, Structure and Function*, Cambridge University Press, 1998.
- [20] N.B. McKeown, *J. Mater. Chem.*, 10 (2000) 1979-1995.
- [21] R.J. Mortimer, *Chem. Soc. Rev.*, 26 (1997) 147-156.
- [22] R.J. Mortimer, *Electrochim. Acta*, 44 (1999) 2971-2981.
- [23] M.K. Nazeeruddin, R. Humphry-Baker, M. Gratzel, et al., *Chem. Commun.*, (1998) 719-720.
- [24] D. Phillips, *Prog. React. Kinet.*, 22 (1997) 175-300.
- [25] C. Piechocki, J. Simon, A. Skoulios, et al., *J. Am. Chem. Soc.*, 104 (1982) 5245-5247.
- [26] I. Rosenthal, *Photochem. Photobiol.*, 53 (1991) 859.
- [27] C.W. Tang, *Appl. Phys. Lett.*, 48 (1986) 183-185.
- [28] G. Witte, C. Woll, *J. Mater. Res.*, 19 (2004) 1889-1916.
- [29] J.D. Wright, *Prog. Surf. Sci.*, 31 (1989) 1-60.
- [30] C.J. Brabec, C. Winder, N.S. Sariciftci, et al., *Adv Funct Mater*, 12 (2002) 709-712.
- [31] C. Burda, X.B. Chen, R. Narayanan, et al., *Chem. Rev.*, 105 (2005) 1025-1102.
- [32] A.N. Cammidge, G. Berber, I. Chambrier, et al., *Tetrahedron*, 61 (2005) 4067-4074.
- [33] A. de la Escosura, M.V. Martinez-Diaz, P. Thordarson, et al., *J. Am. Chem. Soc.*, 125 (2003) 12300-12308.
- [34] G. de la Torre, P. Vaquez, F. Agullo-Lopez, et al., *Chem. Rev.*, 104 (2004) 3723-3750.
- [35] J.A. de Saja, M.L. Rodriguez-Mendez, *Adv Colloid Interfac*, 116 (2005) 1-11.
- [36] A.B. Djuricic, W.Y. Tong, M.H. Xie, et al., *J. Phys. Chem. B*, 110 (2006) 17406-17413.
- [37] J.A.A.W. Elemans, A.E. Rowan, R.J.M. Nolte, *J. Mater. Chem.*, 13 (2003) 2661-2670.
- [38] Y. Guan, S.H. Yu, M. Antonietti, et al., *Chem. Eur. J.*, 11 (2005) 1305-1311.
- [39] G. Guillaud, J. Simon, J.P. Germain, *Coord. Chem. Rev.*, 178 (1998) 1433-1484.
- [40] N. Ishikawa, *Struct Bond*, 135 (2010) 211-228.
- [41] N. Ishikawa, M. Sugita, T. Ishikawa, et al., *J. Am. Chem. Soc.*, 125 (2003) 8694-8695.
- [42] M. Johannsen, K.A. Jorgensen, *J. Org. Chem.*, 60 (1995) 5979-5982.
- [43] N. Kobayashi, W.A. Nevin, *Appl Organomet Chem*, 10 (1996) 579-590.
- [44] J. Leclaire, R. Dagiral, S. Fery-Forgues, et al., *J. Am. Chem. Soc.*, 127 (2005) 15762-15770.
- [45] X.Y. Li, L.E. Sinks, B. Rybtchinski, et al., *J. Am. Chem. Soc.*, 126 (2004) 10810-10811.
- [46] M. Maitrot, G. Guillaud, B. Boudjema, et al., *Chem. Phys. Lett.*, 133 (1987) 59-62.
- [47] X. Michalet, F.F. Pinaud, L.A. Bentolila, et al., *Science*, 307 (2005) 538-544.
- [48] B. Sain, S.L. Jain, V.B. Sharma, *Tetrahedron*, 62 (2006) 6841-6847.
- [49] N. Sehlotho, T. Nyokong, *J Mol Catal A*, 219 (2004) 201-207.
- [50] A.B. Sorokin, S. Mangematin, C. Pergrale, *J Mol Catal A*, 182 (2002) 267-281.
- [51] P.D. Tougaw, C.S. Lent, *J. Appl. Phys.*, 80 (1996) 4722-4736.
- [52] T. Uchiyama, K. Ishii, T. Nonomura, et al., *Chem. Eur. J.*, 9 (2003) 5757-5761.
- [53] D. Wohrle, *Macromol Rapid Comm*, 22 (2001) 68-97.
- [54] N.B. McKeown, *Phthalocyanines and Related Compounds*, 2003.
- [55] N. Kobayashi, J. Mack, *Chem. Rev.*, 111 (2011) 281-321.

- [56] A.B.P. Lever, *Adv. Inorg. Chem. Radiochem*, 7 ed. ed., Acad. Press, New York, 1965.
- [57] F.Z. Henari, *J Opt A*, 3 (2001) 188-190.
- [58] S.V. Rao, *Nonlinear Optics and Applications IV*, 2010.
- [59] J. Clark, G. Lanzani, *Nat Photonics*, 4 (2010) 438-446.
- [60] L. Bogani, W. Wernsdorfer, *Nat Mater*, 7 (2008) 179-186.
- [61] C. Wang, S.B. Lei, K. Deng, et al., *Nano Lett*, 8 (2008) 1836-1843.
- [62] S. Yoshimoto, T. Sawaguchi, W. Su, et al., *Angew.Chem. Int. Ed.*, 46 (2007) 1071-1074.
- [63] P. Bassoul, M. Bouvet, J. Simon, *Synth. Met.*, 61 (1993) 133-137.
- [64] M. Bouvet, J. Simon, *Chem.Phys. Lett.*, 172 (1990) 299-302.
- [65] K.M. Kadish, T. Nakanishi, A. Gurek, et al., *J. Phys. Chem. B*, 105 (2001) 9817-9821.
- [66] M. Lher, Y. Cozien, J. Courtotcoupez, *C. R. Acad. Sci. Ser. II*, 302 (1986) 9-14.
- [67] T.V. Magdesieva, I.V. Zhukov, L.G. Tomilova, et al., *Russ. Chem. Bull.*, 50 (2001) 396-403.
- [68] M.M. Nicholson, *Ind. Eng. Chem. Prod. Res. Dev.*, 21 (1982) 261-266.
- [69] L.G. Tomilova, E.V. Chernykh, V.I. Gavrillov, et al., *Zhurnal Obshchei Khimii*, 52 (1982) 2606-2611.
- [70] I. Yilmaz, T. Nakanishi, A. Gurek, et al., *J. Porph. Phthalocyan.*, 7 (2003) 227-238.
- [71] N. Ishikawa, Y. Kaizu, *Coord.Chem. Rev.*, 226 (2002) 93-101.
- [72] J.Z. Jiang, R.C.W. Liu, T.C.W. Mak, et al., *Polyhedron*, 16 (1997) 515-520.
- [73] N. Kobayashi, *Coord.Chem. Rev.*, 227 (2002) 129-152.
- [74] G. Ostendorp, H. Homborg, *Z. Anorg. Allg. Chem.*, 622 (1996) 1222-1230.
- [75] M. Hirasawa, Y. Sakazaki, H. Hane, et al., *Chem.Phys. Lett.*, 392 (2004) 390-395.
- [76] T. Kobayashi, M. Hirasawa, *J. Phys. Chem. B*, 109 (2005) 74-79.
- [77] Z. Gasyana, P.N. Schatz, *J. Phys. Chem.*, 100 (1996) 1445-1448.
- [78] N. Ishikawa, *J. Porph. Phthalocyan.*, 5 (2001) 87-101.
- [79] N. Ishikawa, Y. Kaizu, *Chem.Phys. Lett.*, 228 (1994) 625-632.
- [80] N. Ishikawa, O. Ohno, Y. Kaizu, et al., *J. Phys. Chem.*, 96 (1992) 8832-8839.
- [81] Z. Gasyana, P.N. Schatz, M.E. Boyle, *J. Phys. Chem.*, 99 (1995) 10159-10165.
- [82] B.S. Prall, D.Y. Parkinson, N. Ishikawa, et al., *J. Phys. Chem. A*, 109 (2005) 10870-10879.
- [83] M.H. Cho, *Chem. Rev.*, 108 (2008) 1331-1418.
- [84] M.H. Cho, *Two-Dimensional Optical Spectroscopy*, CRC Press, 2009.
- [85] M.H. Cho, T. Brixner, I. Stiopkin, et al., *J. Chin. Chem. Soc.*, 53 (2006) 15-24.
- [86] S.H. Shim, M.T. Zanni, *Phys. Chem. Chem. Phys.*, 11 (2009) 748-761.
- [87] J.D. Hybl, A.W. Albrecht, S.M.G. Faeder, et al., *Chem.Phys. Lett.*, 297 (1998) 307-313.
- [88] J.D. Hybl, A.A. Ferro, D.M. Jonas, *J. Chem.Phys.*, 115 (2001) 6606-6622.
- [89] D.M. Jonas, *Ann. Rev. Phys. Chem.*, 54 (2003) 425-463.
- [90] P. Kjellberg, B. Bruggemann, T. Pullerits, *Phys. Rev. B*, 74 (2006) 024303.
- [91] K. Lazonder, M.S. Pshenichnikov, D.A. Wiersma, *Opt.Lett.*, 31 (2006) 3354-3356.
- [92] S.T. Roberts, J.J. Loparo, A. Tokmakoff, *J. Chem.Phys.*, 125 (2006) 084502
- [93] A. Tokmakoff, *J. Phys. Chem. A*, 104 (2000) 4247-4255.
- [94] S. Mukamel, *Principles of nonlinear optical spectroscopy*, Oxford University Press, 1995.
- [95] A. Nitzan, *Chemical dynamics in condensed phases: relaxation, transfer and reactions in condensed molecular systems*, Oxford University Press, 2006.
- [96] M. Volkhard, O. Kühn, *Charge and energy transfer dynamics in molecular systems*, Wiley-VCH, 2004.
- [97] A. Tokmakoff, *Time-Dependent Quantum Mechanics and Spectroscopy in*, MIT Open Course Page, 2010.
- [98] G.R. Fleming, G.S. Engel, T.R. Calhoun, et al., *Nature*, 446 (2007) 782-786.
- [99] G.R. Fleming, A. Ishizaki, T.R. Calhoun, et al., *Phys. Chem. Chem. Phys.*, 12 (2010) 7319-7337.
- [100] F. Milota, J. Sperling, A. Nemeth, et al., *J. Chem.Phys.*, 131 (2009).
- [101] A.M. Moran, J.M. Womick, *J. Phys. Chem. B*, 113 (2009) 15747-15759.
- [102] A.M. Moran, J.M. Womick, S.A. Miller, *J. Phys. Chem. B*, 113 (2009) 6630-6639.
- [103] G.D. Scholes, E. Collini, *Science*, 323 (2009) 369-373.
- [104] G.D. Scholes, E. Collini, C.Y. Wong, et al., *Nature*, 463 (2010) 644-U669.
- [105] C. Elschenbroich, *Organometallchemie*, Teubner B.G., 2005.
- [106] N. Koike, H. Uekusa, Y. Ohashi, et al., *Inorg.Chem.*, 35 (1996) 5798-5804.
- [107] H. Konami, M. Hatano, A. Tajiri, *Chem.Phys. Lett.*, 160 (1989) 163-167.
- [108] I.S. Kirin, P.N. Moskalev, J.A. Makashev, *Zh. Neorg. Khim.*, 10 (1965) 1951-1953.
- [109] K.K. Tateishi, JP), M.K. Taniguchi, JP), H.K. Hanawa, JP), et al., *Method of producing a metal phthalocyanine compound, and method of producing a metal phthalocyanine compound and an analogue thereof*, in: F. Corporation (Ed.) free patents online, 2009.
- [110] S. Bräse, J. Bülle, H. A., *Organische und bioorganische Chemie*, 1st ed. ed., Wiley-VCH 2008.
- [111] A. Aravindakshan, *Copper Phthalocyanines in*, 2005.

- [112] K.C. Patil, Chandras.Gv, M.V. George, et al., *Can J Chemistry*, 46 (1968) 257.
- [113] X. Graehlert, *Synthese, spektroskopische Charakterisierung und Untersuchung des elektrochromen Verhaltens der Diphthalocyanine des Dysprosiums, Holmiums, Erbiums, Thuliums und Ytterbiums*, in, Technical University of Chemnitz, 1998.
- [114] R. Graeve, G.H. Wahl Jr., *J. Chem. Educ.*, 41 (1964) 279.
- [115] J. Janczak, R. Kubiak, *Acta Crystallogr. C*, 51 (1995) 2039-2042.
- [116] D. Qi, L. Zhang, L. Wan, et al., *Phys. Chem. Chem. Phys.*, 13 (2011) 13277-13286.
- [117] N. Sehlotho, *Phthalocyanines: Photochemical, electrochemical and biomimetic catalytic function*, in, Rhodes Univ., 2007.
- [118] M. Lher, Y. Cozien, J. Courtotcoupez, *C. R. Acad. Sci. Ser. II*, 300 (1985) 487.
- [119] T. Toupance, V. Plichon, J. Simon, *New J. Chem.*, 23 (1999) 1001-1006.
- [120] G. Ostendorp, H. Homborg, *Z. Anorg. Allg. Chem.*, 622 (1996) 1415-1418.
- [121] Wiberg E., A.F. Holleman, N. Wiberg, *Lehrbuch der anorganischen Chemie*, Walter de Gruyter, 2007.
- [122] J.E. Huheey, E.A. Keiter, R.I. Keiter, *Inorganic Chemistry: Principles of Structure and Reactivity 4ed.*, Harper Collins, 1993.
- [123] M. Hesse, H. Meier, B. Zeeh, *Spektroskopische Methoden in der organischen Chemie*, 7. ed., Thieme, 2005.
- [124] T. Koyama, T. Suzuki, K. Hanabusa, et al., *Inorg Chim Acta*, 218 (1994) 41-45.
- [125] M.S. Haghghi, G. Peters, H. Homborg, *Z. Anorg. Allg. Chem.*, 620 (1994) 1285-1294.
- [126] N. Ishikawa, Y. Kaizu, *J. Phys. Chem.*, 100 (1996) 8722-8730.
- [127] M. Kasha, *Rad. Res.*, 20 (1963) 55.
- [128] M. Kasha, H.R. Rawls, M.A. El-Bayoumi, *The exciton model in molecular spectroscopy*, in: VIIIth European Congress on Molecular Spectroscopy, Pure Appl. Chem., Copenhagen, Denmark, 1965.
- [129] M. Moussavi, A. Decian, J. Fischer, et al., *Inorg.Chem.*, 27 (1988) 1287-1291.
- [130] H. Konami, M. Hatano, A. Tajiri, *Chem.Phys. Lett.*, 166 (1990) 605-608.
- [131] K. Toyota, J. Hasegawa, H. Nakatsuji, *J. Phys. Chem. A*, 101 (1997) 446-451.
- [132] M.S. Haghghi, H. Homborg, *Z. Anorg. Allg. Chem.*, 620 (1994) 1278-1284.
- [133] J.B. Birks, *J. Res. Nat. Bur. Stnds. A*, 80 (1976) 389.
- [134] J.R. Lakowicz, *Principles of fluorescence spectroscopy*, Springer, 2006.
- [135] S. Yamauchi, H. Konami, K. Akiyama, et al., *Mol Phys*, 83 (1994) 335-344.
- [136] F.L. Lu, M. Bao, C.Q. Ma, et al., *Spectrochim. Acta A*, 59 (2003) 3273-3286.
- [137] J.Z. Jiang, L. Rintoul, D.P. Arnold, *Polyhedron*, 19 (2000) 1381-1394.
- [138] J.Z. Jiang, D.P. Arnold, H. Yu, *Polyhedron*, 18 (1999) 2129-2139.
- [139] J.Z. Jiang, U. Cornelissen, D.P. Arnold, et al., *Polyhedron*, 20 (2001) 557-569.
- [140] *Product Information and Analysis*, in, Sigma Aldrich.
- [141] P.W. Atkins, R.S. Friedman, *Molecular Quantum Mechanics*, 4th ed. ed., Oxford Press, 2005.
- [142] C. Eckart, *Phys Rev*, 47 (1935) 552-558.
- [143] W. Koch, M.C. Holthausen, *A Chemist's Guide to Density Functional Theory*, 3 ed., Wiley-VCH, 2008.
- [144] N.M. Harrison, *An Introduction to Density Functional Theory*, in: C.a. Kotomin (Ed.) *Computational Materials Science*, IOS Press, 2003.
- [145] P. Hohenberg, W. Kohn, *Phys. Rev. B*, 136 (1964) B864.
- [146] W. Kohn, L.J. Sham, *Phys Rev*, 140 (1965) 1133.
- [147] M. Olivucci, *Computational Photochemistry Elsevier*, 2005.
- [148] R.O. Freire, N.B. da Costa, G.B. Rocha, et al., *J. Phys. Chem. A*, 110 (2006) 5897-5900.
- [149] J. Wilson, E. B. , J.C. Decius, P.C. Cross, *Molecular vibrations; the theory of infrared and Raman vibrational spectra*, McGraw-Hill, , 1955.
- [150] M.A.L. Marques, E.K.U. Gross, *Ann. Rev. Phys. Chem.*, 55 (2004) 427-455.
- [151] M.A.L. Marques, C.A. Ullrich, F. Nogueira, et al., *Time-Dependent Density Functional Theory*, in: *Lecture notes in physics*, Springer, 2006.
- [152] J.L. Bredas, D. Beljonne, V. Coropceanu, et al., *Chem. Rev.*, 104 (2004) 4971-5003.
- [153] M. Malagoli, V. Coropceanu, D.A. da Silva, et al., *J. Chem.Phys.*, 120 (2004) 7490-7496.
- [154] J. Burkhardt, *Vibronic coupling in large chromophores*, in: *Dep.Chem.Phys.*, Univ. of Lund, 2008.
- [155] R.S. Sanchez-Carrera, M.C.R. Delgado, C.C. Ferron, et al., *Org. Electron.*, 11 (2010) 1701-1712.
- [156] *TURBOMOLE V6.3 2011*, Forschungszentrum Karlsruhe GmbH, 1989-2007, in.
- [157] *MOPAC 7*, J. J. P. Stewart, Fujitsu Limited, Tokyo, Japan, in.
- [158] J.P. Perdew, K. Burke, M. Ernzerhof, *Phys. Rev. Lett.*, 77 (1996) 3865-3868.
- [159] C. Adamo, V. Barone, *J. Chem.Phys.*, 110 (1999) 6158-6170.
- [160] A.D. Becke, *J. Chem.Phys.*, 98 (1993) 5648-5652.
- [161] A.D. Becke, *J. Chem.Phys.*, 98 (1993) 1372-1377.
- [162] K. Eichkorn, F. Weigend, O. Treutler, et al., *Theor Chem Acc*, 97 (1997) 119-124.

- [163] J.F. Jensen, Introduction to Computational Chemistry, 2nd ed. ed., Wiley VCH, 2006.
- [164] C.J. Cramer, Essentials of computational chemistry: theories and models, 2 ed., John Wiley 2004.
- [165] A. Dreuw, M. Head-Gordon, J. Am. Chem. Soc., 126 (2004) 4007-4016.
- [166] A. Dreuw, J.L. Weisman, M. Head-Gordon, J. Chem.Phys., 119 (2003) 2943-2946.
- [167] D. Rocca, Time-Dependent Density Functional Perturbation Theory - New algorithms with applications to molecular spectra, in: Scuola Internazionale Superiore di Studi Avanzati, 2007.
- [168] Y. Zhao, D.G. Truhlar, J. Phys. Chem. A, 110 (2006) 13126-13130.
- [169] D.J. Tozer, N.C. Handy, J. Chem.Phys., 109 (1998) 10180-10189.
- [170] D.J. Tozer, J. Chem.Phys., 119 (2003) 12697-12699.
- [171] I. Tavernelli, TDDFT as a tool in chemistry, in: Time dependent Density-Functional Theory: Prospects and Applications, École polytechnique fédérale de Lausanne, Benasque, Spain, 2008.
- [172] R. Baer, D. Neuhauser, Phys. Rev. Lett., 94 (2005) 043002.
- [173] Y. Tawada, T. Tsuneda, S. Yanagisawa, et al., J. Chem.Phys., 120 (2004) 8425-8433.
- [174] O. Gritsenko, E.J. Baerends, J. Chem.Phys., 121 (2004) 655-660.
- [175] N.T. Maitra, J. Chem.Phys., 122 (2005) 234104.
- [176] H.P. Breuer, F. Petruccione, The Theory of Open Quantum Systems Oxford University Press, 2007.
- [177] K. Blum, Density Matrix Theory and Applications 3ed., Springer-Verlag 2011.
- [178] D. Abramavicius, S. Mukamel, J. Chem.Phys., 133 (2010) 064510.
- [179] B. Palmieri, D. Abramavicius, S. Mukamel, J. Chem.Phys., 130 (2009) -.
- [180] J.L. Skinner, J.R. Schmidt, N. Sundlass, Chem.Phys. Lett., 378 (2003) 559-566.
- [181] W.P. deBoeij, M.S. Pshenichnikov, D.A. Wiersma, Chem.Phys. Lett., 253 (1996) 53-60.
- [182] P. Hamm, Principles of Nonlinear Optical Spectroscopy: A Practical Approach, in, Univ. of Zurich, 2005.
- [183] E. Riedle, M. Beutter, S. Lochbrunner, et al., Appl. Phys. B, 71 (2000) 457-465.
- [184] J. Piel, E. Riedle, L. Gundlach, et al., Opt.Lett., 31 (2006) 1289-1291.
- [185] T. Wilhelm, J. Piel, E. Riedle, Opt.Lett., 22 (1997) 1494-1496.
- [186] E. Riedle, NOPA - Fundamentals and Instructions, in, LMU Munich, 2002.
- [187] J. Sperling, Two-Dimensional Optical Spectroscopy of Molecular Systems, in: Dep. Phys. Chem., Vienna, Vienna, 2010.
- [188] G. Steinmeyer, Opt. Express, 11 (2003) 2385-2396.
- [189] P. Baum, M. Breuer, E. Riedle, et al., Opt.Lett., 31 (2006) 2220-2222.
- [190] R.L. Fork, O.E. Martinez, J.P. Gordon, Opt.Lett., 9 (1984) 150-152.
- [191] R. Trebino, K.W. DeLong, D.N. Fittinghoff, et al., Rev. Sci. Instrum., 68 (1997) 3277-3295.
- [192] K.W. DeLong, R. Trebino, J. Hunter, et al., J. Opt. Soc. Am. B, 11 (1994) 2206-2215.
- [193] P. Baum, E. Riedle, J. Opt. Soc. Am. B, 22 (2005) 1875-1883.
- [194] C. Iaconis, I.A. Walmsley, IEEE J.Quant. Electron., 35 (1999) 501-509.
- [195] Diels J.C., W. Rudolph, Ultrashort laser pulse phenomena: fundamentals, techniques, and applications on a femtosecond time scale, 2nd ed. ed., Academic Press, 2006.
- [196] T. Brixner, T. Mancal, I.V. Stiopkin, et al., J. Chem.Phys., 121 (2004) 4221-4236.
- [197] A. Nemeth, Exploring the potentials of two-dimensional electronic spectroscopy, in: Dep. Phys. Chem., Vienna, Vienna, 2010.
- [198] M.L. Cowan, J.P. Ogilvie, R.J.D. Miller, Chem.Phys. Lett., 386 (2004) 184-189.
- [199] M.J. Tauber, R.A. Mathies, X.Y. Chen, et al., Rev. Sci. Instrum., 74 (2003) 4958-4960.
- [200] A. Nemeth, J. Sperling, J. Hauer, et al., Opt.Lett., 34 (2009) 3301-3303.
- [201] L. Lepetit, G. Cheriaux, M. Joffre, J. Opt. Soc. Am. B, 12 (1995) 2467-2474.
- [202] C. Dorrer, N. Belabas, J.P. Likforman, et al., J. Opt. Soc. Am. B, 17 (2000) 1795-1802.
- [203] U. Megerle, I. Pugliesi, C. Schrieffer, et al., Appl. Phys. B, 96 (2009) 215-231.
- [204] D. Herrmann, S. Niesar, C. Scharsich, et al., J. Am. Chem. Soc., submitted (2011).
- [205] M. Bradler, private communication, in.
- [206] E.J. Brown, Q.G. Zhang, M. Dantus, J. Chem.Phys., 110 (1999) 5772-5788.
- [207] E. Vauthey, Introduction to nonlinear optical spectroscopic techniques for investigating ultrafast processes, in, Univ. of Geneva, 2006.
- [208] B.S. Prall, D.Y. Parkinson, G.R. Fleming, et al., J. Chem.Phys., 120 (2004) 2537-2540.
- [209] E. Orti, J.L. Bredas, C. Clarisse, J. Chem.Phys., 92 (1990) 1228-1235.
- [210] R. Rousseau, R. Aroca, M.L. Rodriguezmendez, J. Mol. Struct., 356 (1995) 49-62.
- [211] I.H.M. van Stokkum, D.S. Larsen, R. van Grondelle, Biochim. Biophys. Acta, 1657 (2004) 82-104.
- [212] M. Khalil, N. Demirdoven, A. Tokmakoff, Phys. Rev. Lett., 90 (2003) 047401

Appendix A: Device specifications

Elementary Analysis:

C, N, H – contents were measured via combustion analysis using a Perkin Elmer 2400 CHN Elemental Analyzer and a TCD detector. Oxygen was used as operating gas and helium as carrier.

NMR:

All NMR spectra were recorded with an AVIII 400 device from Bruker at room temperature using a BBFO sampling head. DMSO-d₆, (CD₃)₂SO, was employed as solvent and tetramethylsilane, (CH₃)₄Si, added as internal standard.

UV-VIS:

UV-VIS spectra in the range of 200 – 800 nm were recorded with a Perkin-Elmer Lambda 7 UV-VIS spectrometer and PD detector. The complex salt was dissolved in and referenced against spectrophotometric grade acetonitrile, CH₃CN. Three cycles were recorded at room temperature at a scan speed of 7.5 nm / min. and 2 nm resolution in a quartz cuvette.

Fluorescence:

Fluorescence spectra are obtained with a Fluorolog II, Spex 1681 spectrometer and a PMT detector. The complex salt was dissolved in spectrophotometric grade benzonitrile, C₆H₅CN and excited with a Xenon lamp at 333 nm, 620 nm and 705 nm. Spectra were recorded at 1 nm increments with an integration time of 1 sec and averaged over 3 cycles.

IR:

IR spectra are received with a Vertex 70 FT-IR spectrometer and MCT detector from Bruker at room temperature in benzonitrile. The data were recorded in a transmission cell with zinkselenide, ZnSe, windows from 1000 – 8000 cm⁻¹ with 4 cm⁻¹ resolution and medium scan speed.

Raman:

FT-Raman spectra were measured with the RAM II FT-Raman-module of Vertex 70 FT-IR spectrometer from Bruker. The sample, dissolved in benzonitrile, was excited with a Nd:YAG-laser at 1064 nm and 120 mW, A germanium detector was employed and cooled with liquid nitrogen to 77 K.

ESI-MS:

ESI spectra are obtained with a Finnigan mass spectrometer at 4 kV voltage in acetonitrile / methanol, CH₃CN / CH₃OH.

Curriculum

Oliver Bixner

Personal Data

Date of Birth: 02.02.1986
Place of Birth: Klosterneuburg, Austria
Nationality: Austrian

Education

1996 – 2004 Bundes- und Bundesrealgymnasium Klosterneuburg
De la Salle Schule Strebersdorf , Vienna
Gymnasium und wirtschaftskundliches Realgymnasium
Haizingergasse, Vienna

Since 2005 Study of Chemistry, University Vienna

Career History

02/2004 Participation at Rhetoric Seminars, Die Berater, Vienna

06/2008 Attending the summer school "Mixed Quantum-Classical Dynamics: Foundations and Application to Photo-Biological Questions", organized by Prof. H. Lischka, University of Vienna

08/2008 Internship at the Quantum Optics, Quantum Nanophysics, Quantum Information group around Prof. M. Arndt, University of Vienna

02/2010 Attending the workshop on Theoretical Chemistry "Dynamics in Excited States", organized by Dr. M. Barbatti, MPI Mühlheim

03-06/2010 Research stay at the Department of Bioorganic Chemistry with Prof. W. Schmidt, University of Vienna

10/2010-01/2011 Tutor at "Practical Chemistry Training for Biologists and Nutritionists", Institute of Organic Chemistry, University of Vienna

02/2011 Research sojourn at the Department of Biomolecular Optics with Prof. E. Riedle, Ludwig-Maximilians-Universität, Munich

Since 03/2010 Diploma Student at the Institute of Theoretical Chemistry, Quantum Chemistry and Chemical Dynamics group, Prof. Werner Jakubetz , University of Vienna

Since 06/2010 Member of Ultrafast Dynamics group with Prof. H.F. Kauffmann, Department Electronic Properties of Materials, Institute of Physics, University of Vienna

Publications

- High frequency vibrational modulations in two-dimensional electronic spectra and their resemblance to electronic coherence signatures, N. Christensson, F. Milota, J. Hauer, J. Sperling, O. Bixner, A.

Nemeth, and H. F. Kauffmann, *J. Phys. Chem. B* , 115, 18, 5383-5391 (2011)

- Dynamics of Quantum Wave Packets in Complex Molecules Traced by 2D Coherent Electronic Correlation Spectroscopy, T. Mančal, O. Bixner, N. Christensson, J. Hauer, F. Milota, A. Nemeth, J. Sperling, H.F. Kauffmann, Contribution to the 22nd Solvay Conference on “Quantum Effects in Chemistry and Biology” in *Procedia Chemistry* (2010)

Research Interests

- Synthesis and Nonlinear Spectroscopy of Organic and Biological Molecules
- Femto-Chemical Physics
- Quantum Chemical Modelling